

**STUDY OF STRUCTURAL, ELECTRICAL, OPTICAL AND
MAGNETIC PROPERTIES OF ZnO BASED FILMS
PRODUCED BY MAGNETRON SPUTTERING**

by

Luis Manuel Angelats Silva

A thesis submitted in the fulfillment of the requirements for the degree of

**MASTER OF SCIENCE
in
PHYSICS**

UNIVERSITY OF PUERTO RICO
MAYAGÜEZ CAMPUS
2006

Approved by:

Maharaj S. Tomar, PhD
Member, Graduate Committee

Date

Oscar Perales Pérez, PhD
Member, Graduate Committee

Date

Héctor Jiménez Gonzáles, PhD
President, Graduate Committee

Date

Oscar Marcelo Suarez, PhD
Representative of Graduate Studies

Date

Héctor Jiménez Gonzáles, PhD
Chairperson of the Department

Date

ABSTRACT

This work focused on the evaluating of the structure, optical, electrical and magnetic properties of and $Zn_{0.90}Co_{0.10}O$ and $Zn_{0.85}[Co_{0.50}Fe_{0.50}]_{0.15}O$ thin films synthesized from ceramic targets using the magnetron sputtering technique. Given the complexity of the deposition processes and in order to optimize the quality of the films in study, the first step this work consisted in carrying out a systematic study about the structural features and optical properties of ZnO films as function of substrate to target distance and rf power considering the magnetron sputtering system used in this work. This study revealed that the substrates must be located between -1 cm and + 6 cm on holder with a vertical substrate to target distance of 7.5 cm approximately. The sputtering conditions possible or range optimum for the deposition were: rf power between 80 and 125 W, argon working pressure between 8.0×10^{-3} and 9.0×10^{-3} Torr, substrate temperature between 200 and 300°C. The X-ray diffraction patterns of $Zn_{0.90}Co_{0.10}O$ and $Zn_{0.85}[Co_{0.50}Fe_{0.50}]_{0.15}O$ films showed only (002) peak indicating the strong preferred orientation along these planes. $Zn_{0.90}Co_{0.10}O$ film showed transmittance above 70% with three absorption peaks in 1.89, 2.03 and 2.18 eV attributed to d-d transitions of tetrahedrally coordinated Co^{2+} . Transmittance optic of $Zn_{0.85}[Co_{0.50}Fe_{0.50}]_{0.15}O$ film was less than $Zn_{0.90}Co_{0.10}O$ film between 400-700 nm. The band gap values for $Zn_{0.90}Co_{0.10}O$ and $Zn_{0.85}[Co_{0.50}Fe_{0.50}]_{0.15}O$ films were 2.95 and 2.70 eV respectively, which are slightly less than ZnO films found in this work. Although these films exhibited good crystallinity with a fraction of Zn atoms substituted by Co and Fe, from M-H measurements no indication of FM in both films was observed between -2000 and 2000 Oe at room temperature, indicating on the contrary, a possible character antiferromagnetic.

RESUMEN

Este trabajo se centró en evaluar la estructura y las propiedades ópticas de películas finas de $\text{Zn}_{0.90}\text{Co}_{0.10}\text{O}$ and $\text{Zn}_{0.85}[\text{Co}_{0.50}\text{Fe}_{0.50}]_{0.15}\text{O}$ sintetizada a partir de targets cerámicos usando la técnica de magnetron sputtering. Dado la complejidad del proceso de deposición y a fin de optimizar la calidad de las películas en estudio, la primera etapa de este trabajo consistió en realizar un estudio sistemático sobre las características estructurales y propiedades ópticas de las películas de ZnO en función de la distancia target-sustrato y de la potencia de radio frecuencia considerando el sistema de magnetron sputtering utilizado en este trabajo. Este estudio reveló que los sustratos deben situarse entre -1 cm y + 6 cm sobre el holder a una distancia vertical debajo del target de 7.5 cm aproximadamente. Las posibles condiciones u rangos óptimas encontrados para la síntesis fueron: Potencia rf, entre 80 y 125 W, presión de gas argón entre 8.0×10^{-3} y 9.0×10^{-3} torr, temperatura del sustrato entre 200 y 300°C. Los patrones de difracción de las películas de $\text{Zn}_{0.90}\text{Co}_{0.10}\text{O}$ y $\text{Zn}_{0.85}[\text{Co}_{0.50}\text{Fe}_{0.50}]_{0.15}\text{O}$ mostraron solo un pico de difracción (002) indicando una fuerte orientación preferencial a lo largo de estos planos. La película de $\text{Zn}_{0.90}\text{Co}_{0.10}\text{O}$ mostró transmisión por encima del 70% con tres picos de absorción en 1.89, 2.03 y 2.18 eV atribuido a las transiciones $d-d$ del CO^{2+} tetraédricamente coordinado. La transmisión óptica de la película de $\text{Zn}_{0.85}[\text{Co}_{0.50}\text{Fe}_{0.50}]_{0.15}\text{O}$ para la región entre 400-700 nm fue menor que la encontrada en la película de $\text{Zn}_{0.90}\text{Co}_{0.10}\text{O}$. Los valores de band gap para $\text{Zn}_{0.90}\text{Co}_{0.10}\text{O}$ y $\text{Zn}_{0.85}[\text{Co}_{0.50}\text{Fe}_{0.50}]_{0.15}\text{O}$ fueron 2.95 y 2.70 eV respectivamente, los cuales son ligeramente menores que las películas de ZnO encontradas en este trabajo. Aunque estas películas exhibieron buena cristalinidad con una fracción de los átomos del Zn substituidos por Co y Fe, a partir de las mediciones de $M-H$ no se observó ninguna indicación de FM en ambas películas entre O_e -2000 y 2000 a temperatura ambiente, indicando por el contrario, un posible carácter antiferromagnetic.

Copyright © 2006

By

Luis Manuel Angelats Silva

Dedicatory

To my loved wife Dalila and to my adored daughter Jazmín.

To my parents Luis and Bertha and to my brothers: Ana Bertha, Oscar Miguel,
Eva Elena and Carlos Fernando,

.....for their unconditional support, inspiration and love.

And..... to a “star” called Lucía who is in the sky and lives close to God
taking care to me.

ACKNOWLEDGEMENTS

During the development of my graduate studies in Department of Physics of the University of Puerto Rico-Mayaguez Campus several persons and institutions collaborated directly and indirectly with my research. Without their support it would be impossible for me to finish my work. That is why I wish to dedicate this section to recognize their support. I want to start expressing a sincere acknowledgement to:

Dr. Maharaj S. Tomar for introducing me to this subject and his invaluable guidance and because gave me the opportunity and confidence for research in his laboratory.

Dr. Héctor Jiménez by support I received from him as my advisor and by his valuable knowledge offered in the course of advanced physics of solid state, which was important for the discussion this work.

Dr. Oscar Perales Pérez by his patient labor as orientation professor and by his helpful discussions contributed for this researching.

My friend Ricardo Edilberto Manuel Melgarejo Salas by support I received about of the Raman spectra analysis carried out on my samples.

Dr. Wilfredo Otaño and Mr. José Gonzales, both of the Department Mathematic-Physics at the University of Puerto Rico – Cayey Campus by the valuable collaboration for chemical and surface analysis on my sample carried out on their laboratory.

NSF-PREM Grant No. 0351449 and NSF-EPS Grant No. 0223152 by the offered economic support during the development of this research.

At last, but the most important I would like to thank my friends of the graduated student's office F-439 of physics building.

TABLE OF CONTENTS

ABSTRACT	ii
RESUMEN	iii
DEDICATORY	v
ACKNOWLEDGEMENTS	vii
TABLE OF CONTENTS	vii
TABLE LIST	ix
FIGURE LIST	x
CHAPTER 1	1
1.1 Introduction.....	1
1.2 Aim of study.....	3
1.3 Summary of following chapters.....	3
CHAPTER 2 ZnO films	5
2.1 Introduction.....	5
2.2 Physical properties of zinc oxide.....	6
2.2.1 ZnO lattice.....	6
2.2.2 The band structure of ZnO.....	10
2.3 Synthesis of the ZnO thin films.....	14
2.3.1 Deposition techniques.....	14
2.3.2 Sputtering of ZnO.....	21
2.3.3 Influence of deposition parameters on ZnO thin film.....	23
CHAPTER 3 Magnetic properties of diluted magnetic semiconductors oxides	36
3.1 Introduction.....	36
3.2 Phenomenology.....	36
CHAPTER 4 Experimental procedure	46
4.1 Introduction.....	46
4.2 Preparation of the substrates.....	47
4.3 Description of magnetron sputtering system.....	47
4.4 The sputtering targets.....	50
4.5 Sputtering deposition procedure of ZnO films.....	50
4.5.1 Substrate to target distances.....	50
4.5.2 Radio frequency power (P_{rf}) sputtering deposition.....	52
4.5.3 Doping of ZnO film with Aluminum (Al) by co-sputtering deposition.....	52
4.6 Sputtering deposition procedure of Co-doped ZnO and Co,Fe-doped ZnO films.....	52
4.7 Characterization of the films.....	53

4.7.1	Introduction.....	53
4.7.2	Determination of film thickness.....	53
4.7.3	Structural characterization.....	54
4.7.3.1	X-ray diffraction.....	54
4.7.3.2	Atomic force microscopy (AFM).....	61
4.7.3.3	Scanning electron microscopy (SEM).....	63
4.7.3.4	Optical characterization of films.....	64
4.7.3.5	Magnetic properties of films.....	64
CHAPTER 5 Results and discussions.....		66
5.1	Introduction.....	66
5.2	Sputtering deposition of ZnO films.....	66
5.2.1	ZnO thickness and deposition rate.....	66
5.2.2	Structure of ZnO film.....	71
5.2.2.1	XRD patterns.....	71
5.2.3	Optical properties of ZnO films.....	77
5.3	Sputtering deposition of Al-doped ZnO film.....	82
5.4	Substrate effect on structure of ZnO film.....	86
5.5	Optimum deposition conditions of ZnO-based films.....	87
5.6	Sputtering deposition of Co-doped ZnO and Co,Fe-doped ZnO films.....	88
5.6.1	Structure.....	89
5.6.1.1	XRD patterns.....	89
5.6.1.2	Raman spectra of ZnO and Co,Fe-doped ZnO films.....	94
5.6.1.3	Surface morphology.....	96
5.6.2	Optical properties of Co,Fe-doped ZnO films.....	99
5.6.3	Resistivity vs temperature of Zn _{0.85} [Co _{0.50} Fe _{0.50}] _{0.15} O film.....	104
5.6.4	Magnetic properties of Co,Fe-doped ZnO films.....	106
CHAPTER 6 Conclusions and suggestions.....		114
References.....		117

TABLE LIST

Tables		Page
Table 2.1	Comparison of measured and calculated lattice parameters , c/a ratio and u parameter reported by several groups for ZnO crystallized in wurtzite.....	10
Table 4.1	Composition and purity of the sputtering targets used for films deposition.....	50
Table 5.1	Thicknesses mean of ZnO films for different substrate positions along holder-substrate diameter.....	68
Table 5.2	Thicknesses mean of ZnO films for rf power different.....	69
Table 5.3	Peak position and calculated lattice parameters at different substrate position on holder.....	75
Table 5.4	Peak position and calculated lattice parameters at different rf power.....	75
Table 5.5	Optimum sputtering conditions for the deposition of ZnO-based films, as determined experimentally in this study.....	88
Table 5.6	Calculated lattice parameters and stress for ZnO, Co-doped ZnO and Co,Fe-doped ZnO films.....	92
Table 5.7	Optical band gap (E_g) and localized states (E_e) measurements of ZnO and Co,Fe-doped ZnO films at room temperature.....	102

FIGURE LIST

Figure		Page
Figure 2.1	(a) Hexagonal wurtzite, note $ \mathbf{a} = \mathbf{b} $, (b) the wurtzite crystal lattice of single crystal ZnO.....	7
Figure 2.2	Schematic representation of a wurtzitic ZnO structure having u parameter expressed as the bond length or the nearest-neighbor distance b divided by c (0.375 in ideal crystal), and α and β (109.47° in ideal crystal) are the bond angles.....	9
Figure 2.3	Band structure for ZnO. The zero in the graphs is taken as the valence band upper edge.....	13
Figure 2.4	Plasma-Enhanced Metal-Organic Chemical Vapor Deposition system.....	14
Figure 2.5	Schematic of MBE system.....	15
Figure 2.6	Schematic of PLD system.....	16
Figure 2.7	Schematic representation of a spray pyrolysis deposition (SPD).....	17
Figure 2.8	The sputtering environment.....	19
Figure 2.9	(a) Schematic diagram of a magnetron sputtering configuration for simultaneous rf and dc excitation (b) electron confinement which causes a non-uniform erosion of the target.....	21
Figure 2.10	Potential distribution in a magnetron sputtering discharge excited by rf.....	22
Figure 2.11	(a) X-ray diffraction spectra of ZnO and Al-doped ZnO films onto glass substrate showing highly preferred (002) orientation (b) Effect of the substrate temperature on FWHM.....	24
Figure 2.12	Effect of the relative oxygen flow (numbers at the peaks) on position of (002) Peak of ZnO films sputtered br rf excitation.....	25

Figure 2.13	XRD spectra of rf sputtered ZnO (---) and ZnO:Al (—) films of different thickness. The vertical bars display the diffraction pattern of zincite powder.....	25
Figure 2.14	(a) Effect of rf power and (b) argon gas pressure on ZnO films.....	26
Figure 2.15	Dependence of the conductivity and mobility with substrate temperature (a) and substrate to target distance for ZnO:Al films (c). $\ln \rho$ vs temperature plot for ZnO and ZnO:Al films.....	28
Figure 2.16	Plot of the resistivity of the Al-doped films grown on different temperature as a function of Al(OH) ₃ content.....	29
Figure 2.17	Dependence of resistivity, carrier concentration and Hall mobility with sputtering pressure.....	30
Figure 2.18	(a) Optical transmittance spectra of ZnO films formed at different sputtering pressures (b) Increase the optical band gap of ZnO films by increase in sputtering pressure.....	32
Figure 2.19	Influence the thickness (a), substrate to target distance (b) and content Al(OH) ₃ -doped ZnO targets on transmittance of Al-doped ZnO films (c). (d) Blue shift the optical band gap by Al(OH) ₃ content in the ZnO target.....	34
Figure 2.20	Relation between α^2 vs $h\nu$ for Al-doped ZnO films prepared at different substrate temperatures.....	35
Figure 2.21	Transmittance and reflectance of (a) undoped ZnO and (b) Al-doped ZnO films.....	35
Figure 3.1	Magnetization curves for dia-, para- and antiferromagnets.....	39
Figure 3.2	Magnetization curves for ferri- and ferromagnets.....	39
Figure 3.3	Hysteresis loop for the magnetization of a magnetization of a magnetic Material.....	41
Figure 3.4	(a) Normal Zeeman effect for a transition between <i>s</i> and <i>p</i> orbitals (b) Transition in the anomalous Zeeman effect.....	43
Figure 4.1	(a) Photograph of the magnetron sputtering system used in this study (b) top plate of chamber showing the targets (c) the process chamber.....	48

Figure 4.2	Schematic representation of the sputtering environment.....	49
Figure 4.3	Schematic representation of the position of the glass microscope slide in relation to substrate to target distance.....	51
Figure 4.4	Profilometer used for measures the thicknesses of the films (NAMAS-Lab of the Mathematic Physic Department of UPR-Cayey).....	54
Figure 4.5	X-ray spectrum, with a bremsstrahlung background and electrons excitations..	56
Figure 4.6	Bragg's diffraction conditions.....	56
Figure 4.7	Effect of crystal size on diffraction.....	58
Figure 4.8	Effect of fine crystallite size on diffraction curves.....	59
Figure 4.9	Interatomic force vs. distance curve. (a) repulsive force (b) attractive force....	62
Figure 4.10	Superconducting quantum interference device (SQUID) as a simple magnetometer.....	65
Figure 5.1	Variation of deposition rate vs substrate position on holder-heater.....	68
Figure 5.2	Variation of deposition rate with rf power.....	70
Figure 5.3	Effects of substrate to target distance on the crystallinity of ZnO films synthesized on glass. (X = substrate position on holder).....	72
Figure 5.4	XRD patterns of the ZnO films at different rf power.....	73
Figure 5.5	Size grain and film stress for different (a) substrate position and (b) rf power..	76
Figure 5.6	Surface morphology of ZnO films on glass with at 150 W rf power.....	77
Figure 5.7	Optical transmissions of ZnO film synthesized onto glass with various (a) substrate position and (b) rf power.....	78
Figure 5.8	Optical band gap of ZnO film at different (a) substrate to target distance and (b) rf power.....	79
Figure 5.9	Optical band gap and film stress of ZnO film with different (a) substrate to target distance and (b) rf power.....	80

Figure 5.10	XRD pattern of ZnO and Al-doped ZnO films deposited onto glass substrate. The inset shows the shift of (002) diffraction peak.....	82
Figure 5.11	SEM surface micrograph of Al-doped ZnO film (Al 4.85%at.) synthesized onto glass at 100 W rf power, $P_w = 9.0 \times 10^{-3}$ Torr).....	83
Figure 5.12	Optical band gap of ZnO and Al-doped ZnO film calculated from plot α^2 vs. $h\nu$	84
Figure 5.13	Diagram model showing the band and density of states by impurity effect (semiconductor <i>n</i> -type).....	85
Figure 5.14	Plot resistivity vs temperature of ZnO and Al (4.85%at.)-doped ZnO films.....	86
Figure 5.15	XRD patterns of ZnO films grown onto quartz and glass substrate.....	87
Figure 5.16	X-ray diffraction pattern of (a) $Zn_{0.90}Co_{0.10}O$ and (b) $Zn_{0.85}[Co_{0.50}Fe_{0.50}]_{0.15}O$ films. Inset: X-ray diffraction of ZnO film.....	90
Figure 5.17	(002) peak of ZnO, $Zn_{0.90}Co_{0.10}O$ and $Zn_{0.85}[Co_{0.50}Fe_{0.50}]_{0.15}O$ films.....	91
Figure 5.18	Variation of $d(002)$ value with the dopant fraction in the films, 'x'.....	92
Figure 5.19	Average grain size and stress of the ZnO and Co,Fe-doped ZnO film.....	94
Figure 5.20	(a) Room temperature Raman spectra of ZnO, $Zn_{0.90}Co_{0.10}O$ and $Zn_{0.85}[Co_{0.50}Fe_{0.50}]_{0.15}O$ films (b) Variation of strongest E_2 mode frequency with Co and Fe content in ZnO film.....	96
Figure 5.21	Surface morphology of (a) ZnO, (b) $Zn_{0.90}Co_{0.10}O$ and (c) $Zn_{0.85}[Co_{0.50}Fe_{0.50}]_{0.15}O$ films. (1 μ m x 1 μ m).....	97
Figure 5.22	SEM image of the $Zn_{0.85}[Co_{0.50}Fe_{0.50}]_{0.15}O$ film deposited on quartz at 300°C at argon pressure 8.5×10^{-3} Torr and 125W rf power.....	98
Figure 5.23	Optical transmittance spectra for ZnO, $Zn_{0.90}Co_{0.10}O$ and $Zn_{0.85}[Co_{0.50}Fe_{0.50}]_{0.15}O$ films.....	100
Figure 5.24	Optical band gap of ZnO, $Zn_{0.90}Co_{0.10}O$ and $Zn_{0.85}[Co_{0.50}Fe_{0.50}]_{0.15}O$ films calculated from Plot α^2 vs. $h\nu$	100

Figure 5.25	Variation of optical band gap with the dopant fraction 'x' in ZnO structure and stress type	102
Figure 5.26	Verdet constant of ZnO, Zn _{0.90} Co _{0.10} O and Zn _{0.90} Co _{0.10} O:Al (6.68%at.) film..	103
Figure 5.27	Variation of resistivity with the temperature of Zn _{0.85} [Co _{0.50} Fe _{0.50}] _{0.15} O film.....	104
Figure 5.28	Variation of resistivity with the temperature (below room temperature) of Co-doped ZnO films.....	105
Figure 5.29	Magnetoresistance (MR) at various temperatures for Zn _{0.90} Co _{0.10} O:Al film. MR is defined as: $[\rho(H) - \rho(0)] / \rho(0)$	107
Figure 5.30	Magnetization as function of applied field at T = 300 K (a) Zn _{0.85} [Co _{0.50} Fe _{0.50}] _{0.15} O and (b) Zn _{0.90} Co _{0.10} O films. The inset in each figure shows the coercivity H_c of 40 and 30 Oe respectively.....	110

CHAPTER 1

1.1 Introduction

The development of functional ferromagnetic semiconductors is a key to the development of spintronics (or spin-based electronics) that will certainly be the devices utilized in the future. A variety of semiconductors materials, called diluted magnetic semiconductors (DMS), combine the two interesting properties: semiconducting and magnetic. Therefore, the spin of electrons that carries the information can be used as an added of freedom degree in novel electronics devices. Such a compound is an alloy between a non-magnetic semiconductor and magnetic element. For these reasons, interest in developing diluted magnetic semiconductors oxides there which exhibit ferromagnetism (FM) upon doping with a few per cent of transition metals. In these alloys, a stoichiometric fraction of the constituent atoms can be replaced by transition metal atoms. Several investigations in dilute magnetic semiconductors come focusing on II–VI semiconductors (CdTe, ZnO for example) in which a fraction of the group II sub-lattice is randomly replaced by Fe, Co or Mn atoms in order to obtain Curie temperature at room temperature. We know that from the practical point of view, it is indispensable to obtain magnetic semiconductors devices showing ferromagnetism at room temperature. Studies theoretical predict that the Curie temperature can be increased above room temperature in *p*-type semiconductor-based DMS. These studies also showed that ferromagnetism (FM) is stable in a DMS which based on a wide bandgap semiconductor. The ZnO is an II-VI compound semiconductor with an wide band gap energy, 3.3 eV and is interesting from the viewpoint of forming a transparent conductive oxide (TCO)

ferromagnetic. ZnO in its non-stoichiometric form, is an *n*-type semiconductor with wurtzite structure, and depending on the type and concentration of carriers as well as on the technique of growth it could be show resistivities as small as $\sim 10^{-5}$ Ω -m. Other importance of this semiconductor is that it can make possible the formation of highly conductive *p*-type by using a co-doping technique. However, the origin and clear establishment of ferromagnetism of DMS in ZnO-based has not been clearly elucidated.

Recently, near room temperature ferromagnetism has been demonstrated in semiconductors transition metal-doped ZnO-based films prepared using a variety of deposition techniques, such as metal Plasma-Enhanced Metal–Organic Chemical Vapor Deposition (PEMOCVD), Molecular Beam Epitaxy (MBE), Pulsed Laser Deposition (PLD), Spray Pyrolysis Deposition (SPD). One of the deposition techniques mostly used by versatility is Magnetron Sputtering (MS). The fundamental difference between magnetron sputtering as a plasma process and thermally excited thin-film preparation methods (evaporation, chemical deposition methods) is the much higher energy input into the growing film providing high deposition rates. Furthermore, compared to other deposition methods, magnetron sputtering is characterized by the following advantages: low substrate temperatures, good adhesion of films on substrates, very good thickness uniformity and high density of the films, alloys and compounds of materials with different vapours pressures can be sputtered easily, among others.

1.2 Aim of study

The most aim of this study was to investigate the structure, electrical, optical and magnetic properties of Co-doped and Co,Fe-doped ZnO films synthesized by the magnetron sputtering technique. In order to obtain a reasonable quality of the films grown by this technique, was considered first to optimize the substrate to target distance and radio frequency power across of influence of these parameters on structure and optical properties of ZnO films deposited onto glass. The influence of the Al content into ZnO film on optical and electrical properties and the influence of the glass and quartz substrate on the structure were also studied.

1.3 Summary of following chapters

One of the II-VI compound semiconductor ZnO has drawn much attention since ZnO-based DMS it is expected as possible candidate to realize a ferromagnetic semiconductor with both at Curie temperature near room temperature and a large magnetization. In Chapter 2, a brief review of the physical properties of ZnO is given here. Attention also will be given to growth techniques generally applied for depositing ZnO films and about influence of deposition parameters by magnetron sputtering on structural, electrical and optical properties. In Chapter 3 a brief review will be given about phenomenology of magnetism and magnetic properties of DMS. In chapter 4 the various processing steps as well as the specific experimental details followed during the deposition of the respective thin films, are described in detail. In this chapter we will describe also about methods and characterization techniques used. The most important characterization techniques, which were used in this study, are: (i) X-ray diffraction (XRD), (ii) Transmission and absorption measurements by UV-vis

reflection. From of the transmission data the optical band gap E_g , it could be calculated. (iii) superconducting quantum interference device magnetomer (SQUID) for measure magnetic properties. (iv) X-ray diffraction (XRD), Raman spectra, atomic force microscopy (AFM) and Scanning electron microscopy (SEM) for structural analyses was used. The experimental results that followed from this study are discussed in detail in Chapter 5. Finally, conclusions and suggestions are presented in Chapter 6.

CHAPTER 2

ZnO films

2.1 Introduction

Zinc oxide (ZnO) films have been investigated in recent years as transparent conducting oxide (TCO) because of their good electrical and optical properties in combination with large band gap, abundance in nature, and absence of toxicity [1]. This material is an II-VI compound semiconductor with a wide variety of applications as electrodes, window materials in display, solar cells, and various optoelectronic devices [2-5]. Besides, ZnO have attracted intense attention in the searching for high temperature de Curie (T_c) ferromagnetic diluted magnetic semiconductors (DMS) materials since Dietl *et al.* [6] predicted that ZnO-based DMSs could exhibit ferromagnetism above room temperature upon doping with transition elements. Further, it should be noted that this material offers a number of advantages. Among these we may mention that ZnO-based films [7]:

- (i) consist of cheap and abundant elements, which may be contrasted with the more expensive In-coating films;
- (ii) are nontoxic, whereas Cd-containing films have potential health hazards;
- (iii) are readily produced by sputtering technology, which is currently preferred for large-scale architectural coatings; and
- (iv) allow tailoring of the ultraviolet absorption, which is possible because the fundamental gap of ZnO lies just at the end of the luminous spectrum.

In this chapter, attention will be given to the structural, optical and electrical properties of this important semiconducting material. Attention also given to the growth techniques generally applied for depositing ZnO films.

2.2 Physical properties of zinc oxide

2.2.1 ZnO lattice

Most of the group II-VI binary compound semiconductors crystallize in either cubic zincblende or hexagonal wurtzite structure. (II-VI it means an element A from column II and one B from column VI in the periodic table, e.g., ZnO, ZnS, CdTe, HgTe, etc.). Figure 2.1a shows a clinographic projection of this hexagonal structure for AB where each anion (A) is surrounded by four cations (B) at the corners of a tetrahedron, and vice versa, as shown by the dotted lines in the figure. This tetrahedral coordination is typical of *sp* covalent bonding, but these materials also have a substantial ionic character [8]. The space group of the structure wurtzite is $C_{6v}^4(P6_3mc)$, A at $(0,0,0)$ and $(2/3, 1/3, 1/2)$ and B at $(0,0,u)$ and $(2/3, 1/3, 1/2 + u)$ with $u \approx 3/8 = 0.375$ (the u parameter is defined as the length of the bond parallel to the c axis [9]). The lattice parameters are the second nearest neighbor distance a , and c , in the ratio of $c/a = \sqrt{8/3} = 1.633$. ZnO crystallizes in two different crystal lattices. The first is the hexagonal wurtzite lattice, which is mainly used in the thin film industry as a transparent conducting oxide [10]. The second structure is cubic rocksalt (NaCl) that may be obtained at relatively high pressures [11]. This structure is more known to the geologist and is a spinel phase that is used in the understanding of the Earth's lower mantle [3]. At ambient conditions,

the thermodynamically stable phase is wurtzite. The wurtzite crystal lattice of single crystal ZnO is depicted in figure 2.1b. The unit cell contains two zinc (Zn) cations and two oxygen (O) anions. The two important characteristics of the wurtzite structure are the noncentral symmetry and polar surfaces. The structure of ZnO, for example, can be described as a number of alternating planes composed of tetrahedrally coordinated O^{2-} and Zn^{2+} ions, stacked alternately along the c -axis [4]. The oppositely charged ions produce positively charged (0001)-Zn and negatively charged (0001)-O polar surfaces, resulting in a normal dipole moment and spontaneous polarization along the c -axis, as well as a divergence in surface energy.

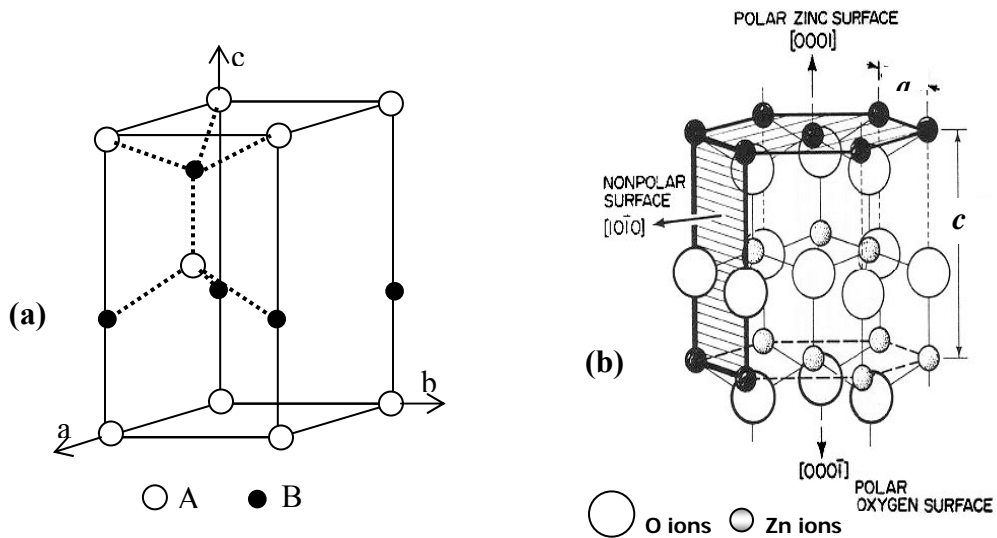


Figure 2.1 (a) Hexagonal wurtzite, note $|a| = |b|$, (b) wurtzite crystal lattice of single crystal ZnO.

Lattice parameters of ZnO

The lattice parameters of a semiconductor usually depend on the following factors: (i) free-electron concentration acting via deformation potential of a conduction-band minimum occupied by these electrons, (ii) concentration of foreign atoms and defects and their difference of ionic radii with respect to the substituted matrix ion, (iii) external strains (for example, those induced by substrate), and (iv) temperature[11,12]. On the other hand, the strict periodicity of lattice is disturbed by many imperfections or defects. These imperfections have a considerable and, some times, even the controlling influence on the mechanical, thermal, electrical and optical properties of semiconductors. They determine the plasticity, hardness, and thermal and electrical conductivities [12].

In a real ZnO crystal, the wurtzite structure deviates from the ideal arrangement, by changing the c/a ratio or the value u . The deviation from that of the ideal wurtzite crystal is probably due to lattice stability and ionicity [1,13]. The point defects such as zinc antisites, oxygen vacancies, and extended defects, such as threading dislocations, also increase the lattice constant in a ZnO crystal, albeit to a lesser extent in the heteroepitaxial layers.

Strong correlation exists between the c/a and the u parameter in that when c/a ratio decreases, the u parameter increases in such a way that those four tetrahedral distances remain nearly constant through a distortion of tetrahedral angles due to long-range polar interactions. These

two slightly different bond lengths will be equal if the following relation holds (see Fig. 2.2)[11]:

$$u = \left(\frac{1}{3}\right)\left(\frac{a^2}{c^2}\right) + \frac{1}{4} \quad 2.1$$

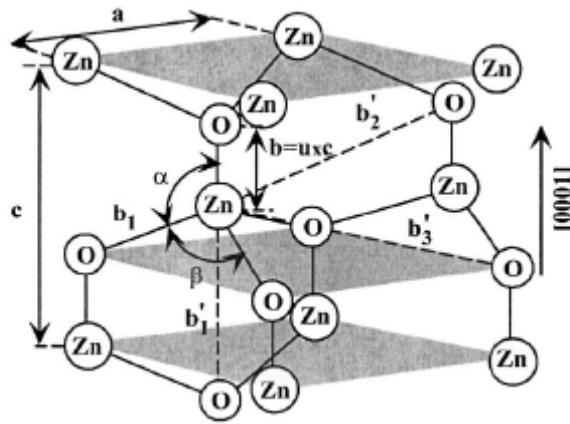


Figure 2.2 Schematic representation of a wurtzitic ZnO structure having u parameter expressed as the bond length or the nearest-neighbor distance b divided by c (0.375 in ideal crystal), and α and β (109.47° in ideal crystal) are the bond angles [11].

For the wurtzite ZnO, lattice constants at room temperature determined by various experimental measurements and theoretical calculations are in good agreement. The lattice constants mostly range from 3.2475 to 3.2860 Å for a parameter and from 5.241 to 5.2075 Å for the c parameter (see Table 2.1). In this table is observed that as c/a ratio decreases, the u parameter increases. The data produced in earlier investigations reviewed by R. Reeber [14]

are also consistent with the values given in Table I. The c/a ratio and u parameter vary in a slightly wider range, from 1.595 to 1.6035 and from 0.3796 to 0.3810, respectively.

Table 2.1 Comparison of measured and calculated lattice parameters, c/a ratio and u parameter reported by several groups for ZnO crystallized in wurtzite.

Wurtzite				
a (Å)	c (Å)	c/a	u	Ref.
3.2475	5.2075	1.6035	0.3796	[15] ^a
3.2495	5.2069	1.6024	0.3798	[16] ^b
3.2498	5.2066	1.6021	0.3799	[17] ^c
3.2497	5.206	1.6020	0.3799	[14] ^d
3.2496	5.2042	1.6015	0.3800	[18] ^e
3.286	5.241	1.595	0.3810	[19] ^f

^aCalculated by using *ab initio* periodic linear combination of atomic orbitals (LCAO) methods.

^bMeasured by using x-ray diffraction.

^cMeasured by using EDXD

^dMeasured by using x-ray powder diffraction.

^eMeasured by using x-ray diffraction.

^fCalculated by using *ab initio* periodic linear combination of atomic orbitals (LCAO) methods

2.2.2 The band structure of ZnO

Considering that the ZnO is a semiconductor to be incorporated in the family of materials for device applications, hence a clear understanding of the band structure is of critical importance to explain the electrical properties and many other phenomena because it determines the relationship between the energy and the momentum of the carrier. The task of determination the energy-momentum relationship for a three-dimensional lattice is of course difficult. It involves the determination of the solutions to Schrödinger equation using the crystal Hamiltonian [9, 20-24]. This crystal Hamiltonian contains energy from electrons in a

lattice structure of the nuclei. The solution can be accomplished in a number of ways using perturbation theory: using tight binding approximation, i.e., using functions that are linear combinations of either atomic or molecular orbitals [9,22]; using pseudopotentials [21,24]; and using various other approaches such as Green's functions techniques [25]. Perturbation theory allows the determination of final energy solution, by using the smaller Hamiltonian terms as perturbing functions. The basis states for using this perturbation are determined from the major term associated with Coulombic interactions with the nuclei. Since the basis functions, involving calculations based on using atomic orbitals near the cores, are $|s\rangle$ and $|p\rangle$ like, the resulting functions are combinations of these at various important points of the first Brillouin zone. The Wigner-Seitz unit cell in the reciprocal space is the first Brillouin zone.

A number of experimental data have been published also regarding the band structure of the electronic states of wurtzite ZnO. X-ray or UV reflection/absorption or emission techniques have conventionally been used to measure the electronic core levels in solids. These methods basically measure the energy difference by inducing transitions between electronic levels (for example, transitions from the upper valence-band states to the upper conduction-band states, and from the lower valence-band states) or by exciting collective modes (for example, the upper core states to the lower edge of the conduction band and to excitations of plasmons). Another important method for the investigation of the energy region is based on the photoelectric effect extended to the x-ray region, namely, photoelectron spectroscopy

(PES)[26]. The peaks in emission spectrum correspond to electron emission from a core level without inelastic scattering, which is usually accompanied by a far-less-intense tail region in the spectrum. More recently, angle-resolved violet photoelectron spectroscopy (ARUPS) technique has started to be used [27]. This technique together with synchrotron radiation excitation has been recognized as a powerful tool that enables experimental bulk and surface electronic band-structure determinations under the assumptions of k conservation and single nearly-free-electron-like final band.

A bulk band structure along the high symmetry lines in the hexagonal Brillouin zone is shown for ZnO in figure 2.3. The band structure was generated theoretically using an empirical tight-binding Hamiltonian [28,29]. The band structure $E(k)$ for ZnO is given along some symmetry lines in the Brillouin zone. The most important thing to notice is that between the occupied bands and the empty bands (specified between Γ_1 and $\Gamma_{1.5}$) there is a optical band gap, E_g , of approximately 3.3 eV. This is the energy difference between the full and empty electron states. These filled states are called the **valence band**, and the energy at the top of the valence band is conventionally the **zero of energy** and is called the **valence band edge**. The empty states above the gap are called the **conduction band**. The lowest point in the conduction band is called the **conduction band edge**. For ZnO the conduction band edge is at $k = 0$, the Γ point, which is also the k -value of the valence band edge. Since for ZnO the valence band and the conduction band edges occur at the same k -values, the material is called a **direct band gap** semiconductor.

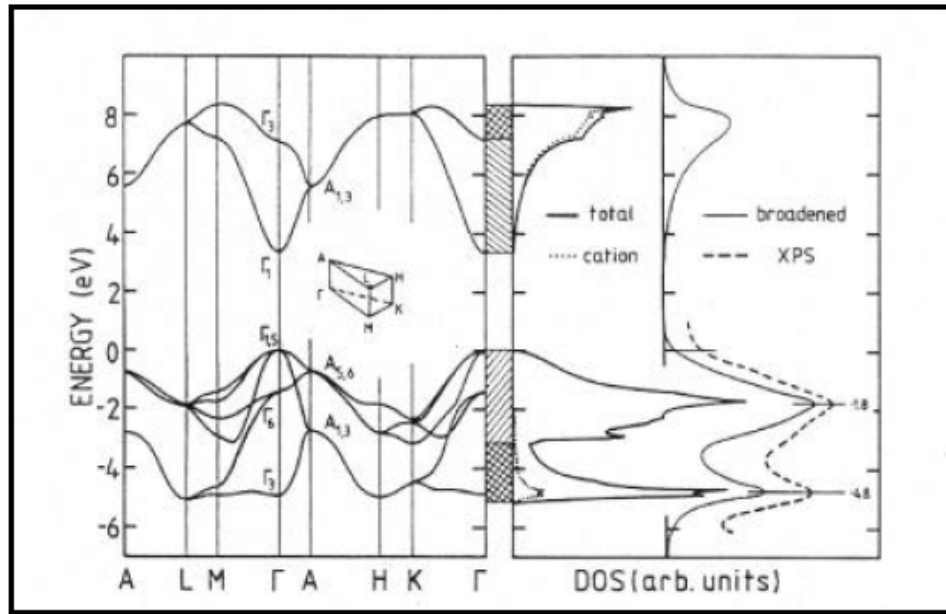


Figure 2.3 Band structure for ZnO. The zero in the graphs is taken as the valence band upper edge [3].

From the band structure (Fig. 2.3) six valence bands can be seen between -6 eV and 0 eV. These six valence bands correspond to the oxygen's $2p$ orbitals that contribute to the band structure. Below -6 eV at about -20 eV the valence band terminates with the oxygen's $2s$ core like state. This specific band (not shown in Figure 3.3) has no significant contribution to the density of states in the conduction band. For the conduction band there are two bands visible (above 3 eV). These bands are strongly localized on the Zn and correspond to the unoccupied Zn: $3s$ levels.

2.3 Synthesis of the ZnO thin films

2.3.1 Deposition techniques

ZnO films can be deposited by a variety of techniques such as:

(i) **Plasma-Enhanced Metal–Organic Chemical Vapor Deposition (PEMOCVD)** [30,31]:

Is one of the most attractive ones for synthesis of high perfection ZnO films at low and moderate temperatures. The deposition system, it consists of continuously pumped horizontal quartz tube placed between copper plates to which RF power (13.56 MHz) is put to excite plasma in the reaction chamber and to dissociate $\text{Zn}(\text{AA})_2$ (AA – acetylacetonate) vapor. The base unit can be equipped by a resistive-heated evaporator where $\text{Zn}(\text{AA})_2$ powder placed in quartz ampoule. Figure 2.4 shows a schematic of the plasma reactor for this technique [30]. Because diethylzinc (DEZ) and dimethylzinc (DMZ) are usually applied as precursors in CVD process, these precursors are less desirable due of its high toxicity. Crystalline sapphire (001), silicon (100) and SiO_2/Si substrates can be use for deposition of thin films.

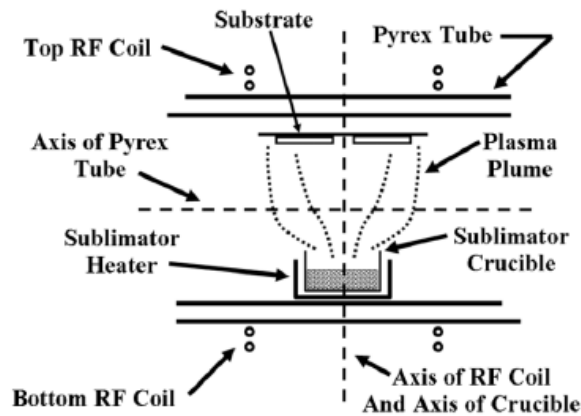


Figure 2.4 Plasma-Enhanced Metal–Organic Chemical Vapor Deposition system [30].

(ii) **Molecular Beam Epitaxy (MBE)** [4,32,33]: In this technique, the growth is performed under clean, low pressure conditions where the potential for contamination is minimized. The wafer on which growth occurs is held at an elevated temperature so that arriving Zn and O atoms have sufficient energy to move around on the surface of the wafer and find their correct bonding positions. If the temperature is too high, these atoms may be re-evaporated from the surface, while if the temperature is too low, the crystal quality of the ZnO layer being grown will be poor. The source materials for the growth are very pure Zn metal, which is evaporated from an oven toward the wafer, and atomic oxygen derived from plasma or ozone source. MBE is capable of layer-by-layer growth with excellent control of the purity and crystalline quality of the resulting film. Figure 2.5 shows a MBE system typical.

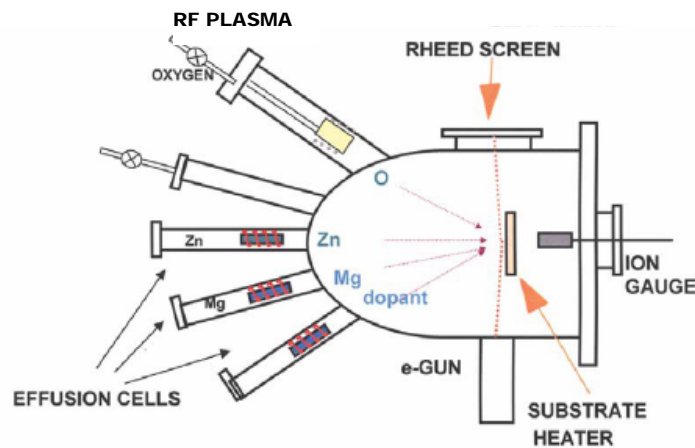


Figure 2.5 Schematic of MBE system [4].

(iii)**Pulsed Laser Deposition (PLD)** [4,31]: A focused laser pulse is directed onto target of material in a vacuum chamber (Figure. 2.6). The laser pulse locally heats and vaporizes the target surface, producing an ejected plasma or plume of atoms, ions, and molecules. The plume of material is deposited onto an adjacent substrate to produce a crystalline film. This technique possesses several favorable characteristics for growth of multicomponent materials, such as stoichiometric transfer of the target material to the substrate, compatibility with a background gas, and atomic level control of the deposition rate. In this method, oxidation of Zn primarily occurs in the ZnO ablation plasma plume, thus alleviating the difficulties encountered with MBE of ZnO, where oxidation proceeds via surface reactions.

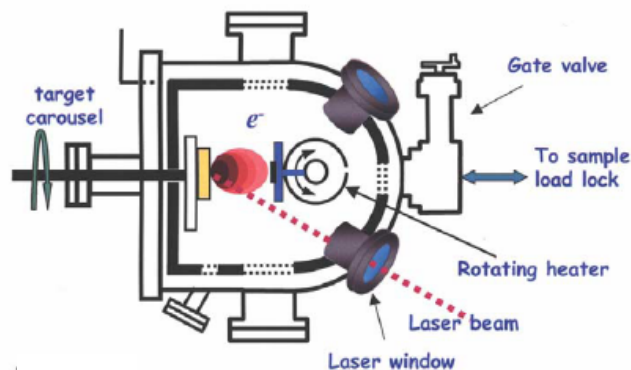


Figure 2.6 Schematic of PLD system [4].

(iv)**Spray Pyrolysis Deposition (SPD)** [34-36]: Because the film formation is carried out in air by a simple apparatus in SPD, the technique is one of the most attractive film preparation methods. SPD is essentially the same film processing technique as so-called pyrosol technique, in which a source solution is sprayed on the heated substrate to be

deposited as a film (see Figure 2.7). In other words, when a source solution is atomized, small droplets splash and vaporizes on the substrate and leaves a dry precipitate in which thermal decomposition occurs. Organometallic compounds and inorganic salts are used as source materials, which are dissolved in water, ethanol or other solvents to prepare source solutions. Because the source materials dissolve in a solvent as an ion, oligomer, or cluster depending on their chemical properties, the surface morphology of deposited films is easily controlled by choosing species of the source materials.

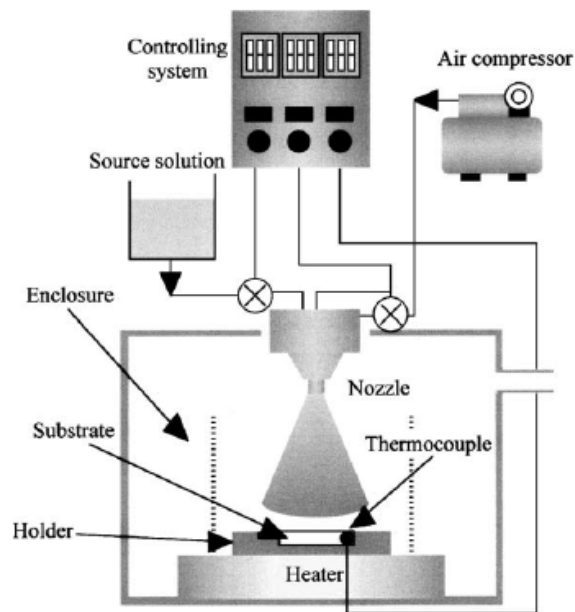


Figure 2.7 Schematic representation of a spray pyrolysis deposition (SPD) [34].

(v) **Magnetron Sputtering (MS)** [37-43]: The planar magnetron sputtering source was invented at the beginning of the seventies [41]. This technique is now one of the most versatile used for the deposition of transparent conducting oxides (TCO). The

fundamental difference between magnetron sputtering as a plasma process and thermally excited thin-film preparation methods (evaporation, chemical deposition methods) is the much higher energy input into the growing film that can be achieved by magnetron sputtering. This technique is characterized by the following advantages [41]:

- low substrate temperature
- good adhesion of films on substrates
- high deposition rates (up to $12 \mu\text{m min}^{-1}$)
- very good thickness uniformity and high density of the films
- good controllability and long-term stability of the process
- by reactive sputtering in rare/reactive gas mixtures many compounds can be deposited from elemental (metallic) targets
- relatively cheap deposition method

Because the growth of ZnO-based thin films in the present work this technique was used, a general discussion on the principles of magnetron sputtering will be presented:

The sputtering environment

Figure 2.8 is a diagram of a simple sputtering chamber. A power supply is connected so that a low pressure gas is ionized by the voltage supplied. The ions of gas produced are accelerated toward the target surface by the voltage where they collide with the atoms of the

target. The kinetic energy of the ions is transferred to these atoms, some of which are ejected and drift across the chamber where they are deposited as a thin film on the substrate material. Still other impacts on the target surface produce secondary electrons [44]. It is these electrons which maintain the electron supply and sustain the glow discharge. The sputtering is usually performed at pressures of 10^{-2} - 10^{-3} Torr. To increase the ionization rate by emitted secondary electrons even further, a magnet called planar magnetron is placed below target in order to maintain the electrons by magnetic field effect.

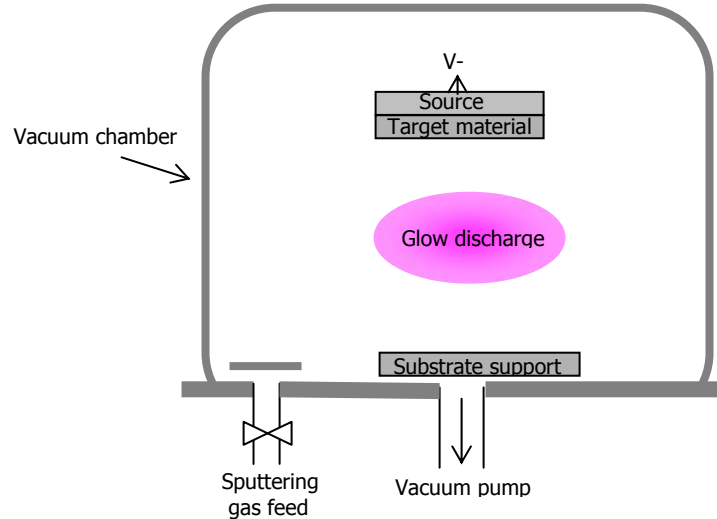


Figure 2.8 The sputtering environment.

Principles of magnetron sputtering

The basic feature of a magnetron discharge is the confinement of the plasma in front of the target (cathode). This is achieved by the combination of electric and magnetic fields [8]. The magnetic field strength is adjusted in such a way (about 50 to 200 mT) that the electrons are significantly influenced by the magnetic field while the ions are not. The electrons perform

cycloidal orbits in the crossed electric and magnetic fields, leading to very high ionization efficiency. Therefore, magnetron discharges can be sustained at much lower pressures ($<10^{-4}$ Torr) and/or higher current densities than the glow discharges without magnetic assistance.

In standard sputtering processes there are usually two modes of powering the magnetron sputtering system. These two modes are direct current (DC) magnetron sputtering or by radio frequency (RF) magnetron sputtering. In DC magnetron sputtering, a direct voltage is applied between the cathode and anode. This method works well with conductive targets (zinc, molybdenum, silver, aluminum, etc). The second method involves the use of a radio frequency source with atypical frequency of 13.56 MHz. This method is preferred for both conductive as well as non-conductive targets (ceramic targets). This mode was mainly employed in the present study. A schematic diagram of both magnetron sputtering discharge configurations is shown in the Figure 2.9a. The magnetic film confines the electrons in front of the target in a torus-like plasma region which causes a non-uniform erosion of the target (Figure 2.9b). The external discharge parameters such as working pressure, discharge power, design of the magnetic field (i.e. balanced or unbalanced magnetrons) and the excitation mode (dc or rf) influence the potential distribution and hence the particle energies.

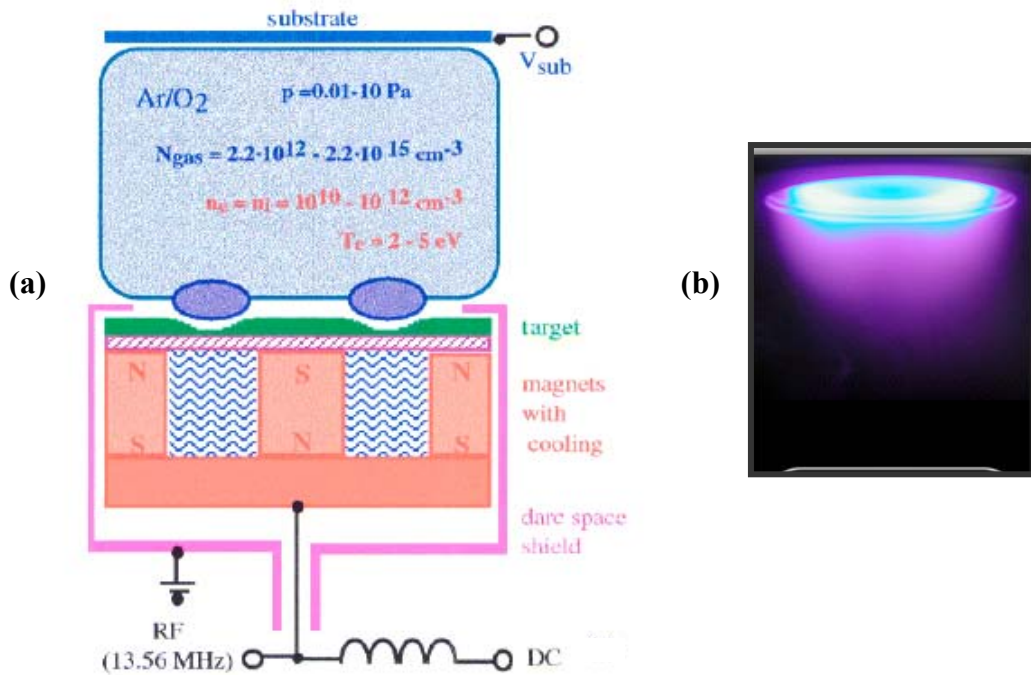


Figure 2.9 (a) Schematic diagram of a magnetron sputtering configuration for simultaneous rf and dc excitation [41] (b) electron confinement which causes a non-uniform erosion of the target.

2.3.2 Sputtering of ZnO

Magnetron sputtering (both RF and DC) can be used in reactive as well as non-reactive modes. There are, however, differences between reactive sputtering with an argon/oxygen mixture from a metallic Zn target, to sputtering ZnO with pure argon from a ceramic ZnO target. The control of film stoichiometry has been found to be much easier with oxide targets, which avoids the need for high temperature and post-deposition annealing. In DC magnetron sputtering of mixed oxide targets, the control of stoichiometry is virtually automatic but depends strongly on argon/oxygen ratio in the sputtering chamber [45], whereas preferential

sputtering of deposited film material in rf magnetron sputtering usually requires that the target composition be suitably adjusted to compensate for material lost at the substrate.

For rf excitation the potential distributions using a ceramic target of ZnO is shown schematically in figure 2.10. The rf plasma is mainly driven by ionization due to electrons which perform an oscillating motion in the plasma body. The electrons are able to follow the rf frequency (atypical) of 13.56 MHz, while the ions (Ar^+ , O^+ , Zn^+) are not, due to their inertia. These positive ions are accelerated in the cathode fall $V_p - V_{dc}$ towards the cathode, leading to the sputtering of the target. On the other hand, electrons and negative ions (O^-) move from the target to the substrate. Together with reflected neutral argon atoms energetic negative ions can reach the substrate and will influence the layer growth. The energy of the particles is a further important quantity to characterize the growth process.

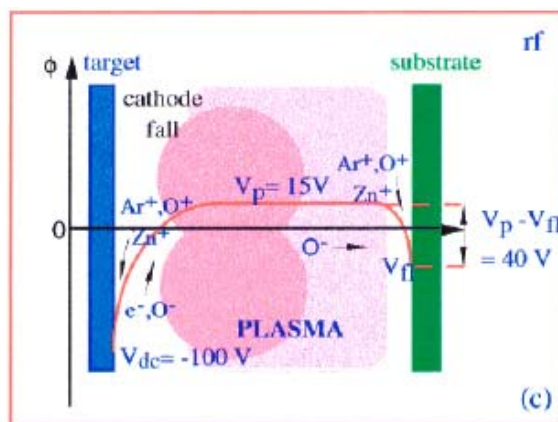


Figure 2.10 Potential distribution in a magnetron sputtering discharge excited by rf [41].

2.3.3 Influence of deposition parameters on ZnO thin film

The effect of sputtering variables (substrate temperature, target to substrate distance, rf power, gas pressure, and composition) on the ZnO film structure, electrical and optical properties have been one of the major research topics. We will make a brief summary about results found in diverse works referred to studio of the sputtering deposition parameters and their relation with some physical properties of the ZnO films.

On Structure

It is well known from several publishing that sputtered ZnO films as revealed by X-Ray Diffraction (XRD) are highly texturized with the *c*-axis perpendicular to the substrate surface [13,38-41,46]. Furthermore was observed that the structure of ZnO films depends strongly on the preparation conditions and by impurity presents. For example, the figure 2.11a shows the typical XRD pattern obtained from ~ 150 nm-thick ZnO and Al-doped ZnO (AZO) thin films on glass substrate prepared by different sputtering targets at rf power = 150W, substrate temperature = 150°C and working pressure = 2 mTorr) [39]. We observe a highly preferred (002) orientation with ZnO(002) peak located at $2\theta = 34.2^\circ$ for all samples indicating that ZnO and (AZO) films prepared by magnetron sputtering show a good *c*-axis orientation that is, the vertical growth to the substrate. In addition to the *c*-axis orientation a little shift of the peak position of the (002) plane is observed with variation of the content in the film due most Al atoms in the AZO are substituted in the Zn site which means that the lattice parameter of ZnO was decrease in the *c*-axis considering the differences between ionic radii (Zn^{2+} : 72 pm,

Al³⁺: 53 pm) [39]. Similar results were found by S.H. Jeong *et al* [13] (see Figure 2.11b). From the inset in figure 2.11b the full width half maximums (FWHMs) of the peak also changed from 0.329 to 0.306° with increasing substrate temperature caused by the crystallinity of the resulting films that have improved and formed a more stoichiometric oxide with increasing substrate temperature.

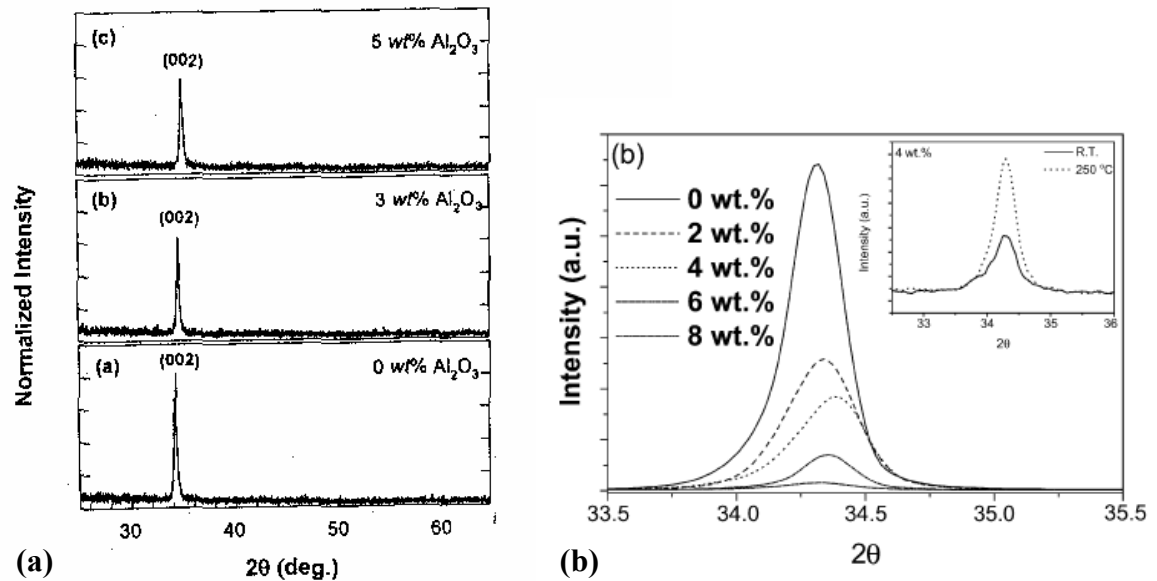


Figure 2.11 (a) X-ray diffraction spectra of ZnO and Al-doped ZnO films onto glass substrate showing highly preferred (002) orientation [39] (b) Effect of the substrate temperature on FWHM [13].

The extent of the texture, the grain size in the films depend significantly on the growth conditions, as shown for reactive magnetron sputtering in figure 2.12. This figure displays the (002) diffraction peak for different oxygen partial pressures during rf sputtering. With rising oxygen partial pressure the peak intensity decreases, the width of the peaks broadens and the peak location is shifted to smaller values compared to the reference peak of zincite powder due to different grain size and internal compressive strain (peak shift) [41].

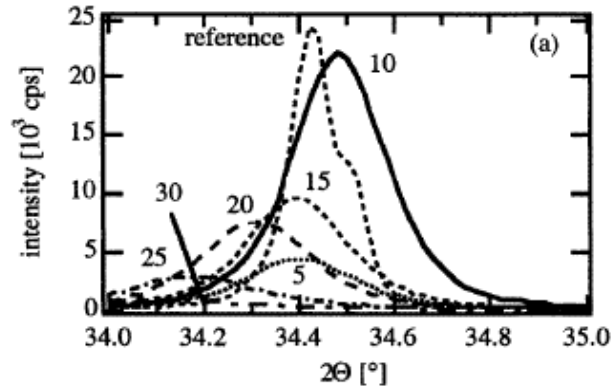


Figure 2.12 Effect of the relative oxygen flow (numbers at the peaks) on position of (002) peak of ZnO films sputtered by rf excitation [41].

The thickness also has influence on texture of ZnO films [40-41]. Figure 2.13 displays expanded XRD spectra of ZnO and ZnO:Al films of different thicknesses on a logarithmic scale [40]. At a larger thickness the zinc oxide films exhibit a (101) peak in addition to the dominating (002) peak. The aluminium-doped zinc oxide films do not show such a (101) peak, which is an indication of the better texture of the doped films.

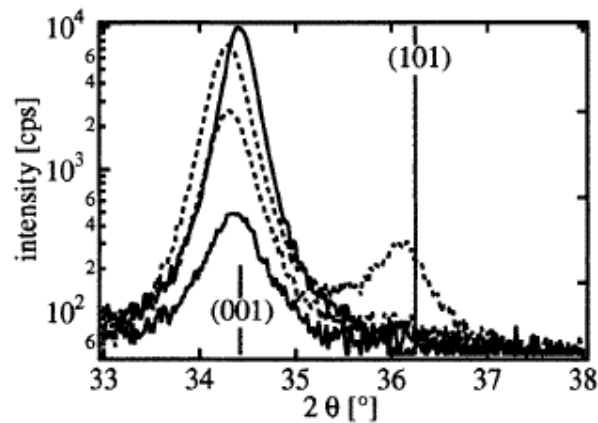


Figure 2.13 XRD spectra of rf sputtered ZnO (- - -) and ZnO:Al (—) films of different thicknesses. The vertical bars display the diffraction pattern of zincite powder [40].

The structural properties depend sensitively also on the power and pressure during deposition [38]. RF power-dependence (with argon gas pressure 10 mTorr and substrate temperature 350°C) of the x-ray diffraction patterns of the Al-doped ZnO films is shown in figure 2.14a. The peak observed at $2\theta = 32^\circ$ corresponds to the (100) peak of ZnO. The broad weak (100) peak emerges at power of 80 W and becomes sharper with increasing power indicating the preferred orientation of the hexagonal zinc oxide with the *c*-axis parallel to the substrate surface. The peak at $2\theta = 36^\circ$ observed in the film deposited at high power corresponds to the (101) peak of aluminium. The results of the x-ray diffraction analysis are shown in figure 2.14b. Relatively sharp (002) peaks of ZnO are observed at $2\theta = 34^\circ$ in the films deposited at a higher gas pressure, whereas no preferred orientation or a broad peak (100) is observed in the case of film prepared at a pressure below 20 mTorr.

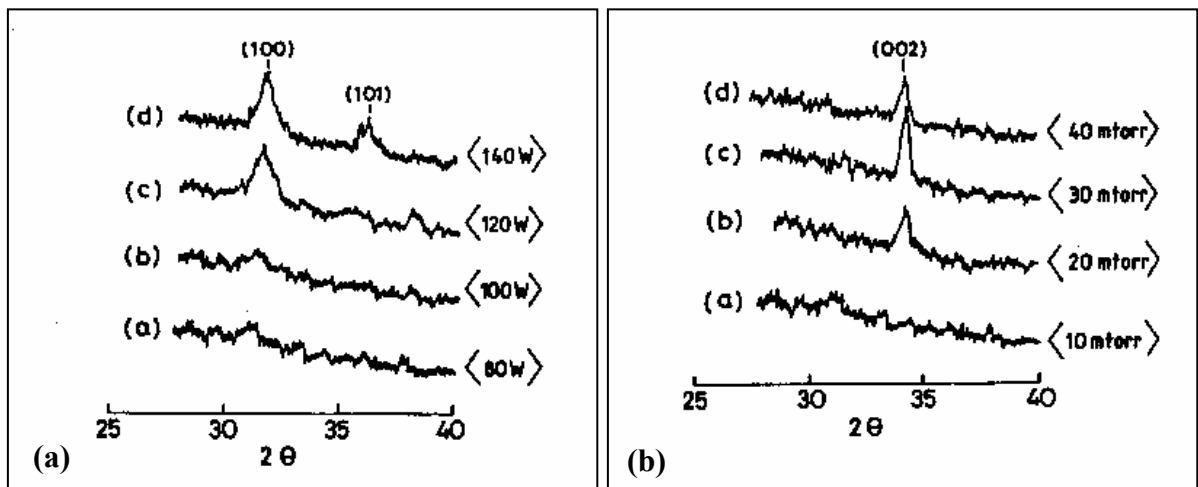


Figure 2.14 (a) Effect of rf power and (b) argon gas pressure on ZnO films [38].

In conclusion, the texture as quantified from the (002) peak depends on many deposition parameters such as oxygen partial pressure, substrate temperature, rf power, thickness of or from the dopant.

On electrical properties

We saw previously that heavily doped ZnO is a degenerate *n*-type semiconductor with an optical gap of about 3.3 eV at 300 K [11]. Depending on the stoichiometry and/or the presence of impurities (dopants), the resistivity can vary widely from 10^{17} - 10^{-4} Ω -cm [47]. Carrier concentration and mobility in the thin film can vary from 10^{18} - 10^{20} /cm³ and mobility from 10-100 cm²/V.s depending of the deposition parameters and doping. M.K. Jayaraj *et al* [49] found for undoped zinc oxide and aluminum doped zinc oxide films prepared by rf magnetron sputtering that the electrical resistivity of the film strongly depends on the substrate temperature (Figure 2.15a), substrate to target distance (Fig 2.15b) and very little dependence on temperature (Fig. 2.15c) where can be observed that the resistivity of undoped ZnO increases slightly with decreasing temperature. This dependence is too small in the case of ZnO: Al films. The nearly temperature independence of the resistivity confirms that the Al doped ZnO films are degenerate semiconductors. Furthermore, the increase in conductivity is due to the increase of carrier concentration and also due to the increased mobility of the carriers.

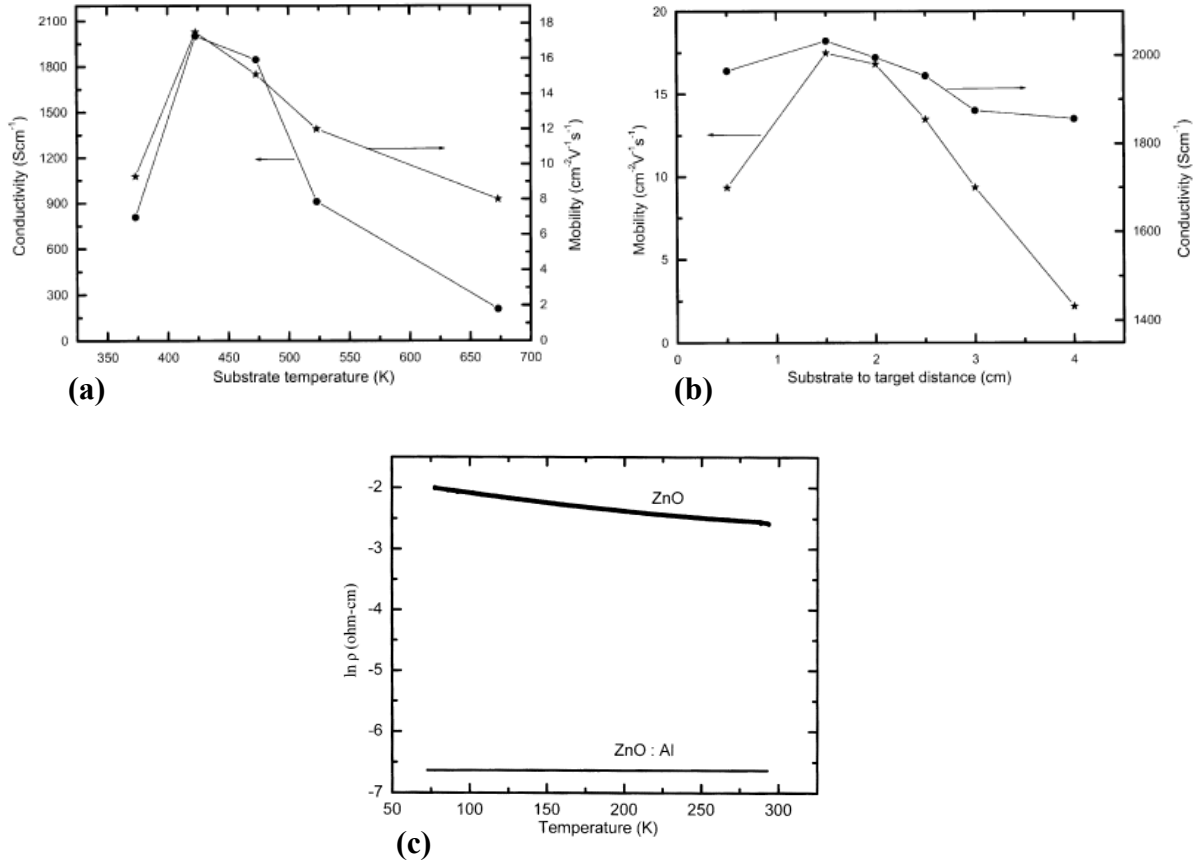


Figure 2.15 Dependence of the conductivity and mobility with substrate temperature and substrate to target distance for ZnO:Al films (a) y (b). $\ln \rho$ vs temperature plot for ZnO and ZnO:Al films (c) [49].

S.H. Jeong et al [13] found also that increasing Al content on ZnO films from high purity zinc oxide (99.99%) and aluminum hydroxide (Al(OH)₃) target, the resistivity was decreased from $5.0 \times 10^{-1} \Omega\text{-cm}$ to a minimum value of $9.8 \times 10^{-2} \Omega\text{-cm}$ (Figure 2.16). However, was observed that the resistivity of the AZO film prepared with >6 wt.% Al(OH)₃ doped ZnO target has been increased up to 12 $\Omega\text{-cm}$.

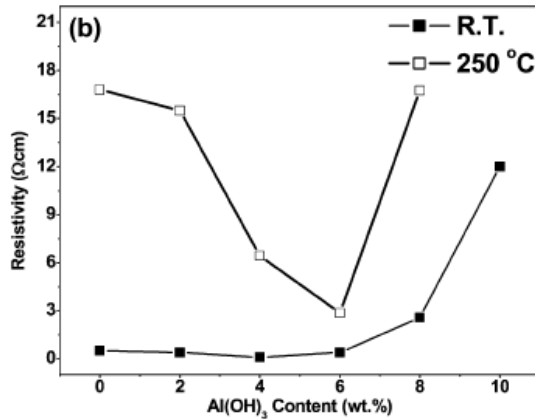


Figure 2.16 Plot of the resistivity of the Al-doped films grown at different temperatures as a function of Al(OH)₃ content [13].

Another important parameter that influences the electrical properties of ZnO is the sputtering pressure. T.K. Subramanyam *et al.* [48] found that the electrical resistivity of the ZnO films deposited on glass substrate by reactive sputtering from metallic target zinc (substrate to target distance: 65 mm, oxygen partial pressure (p_{O_2}): 1×10^{-3} mbar, substrate temperature: 663 K) decreased from 3.2×10^{-1} Ω -cm to 6.9×10^{-2} Ω -cm with increase in sputtering pressure from 3×10^{-2} mbar to 6×10^{-2} mbar there after increased to 1 Ω -cm at a sputtering pressure of 10×10^{-2} mbar. The variation of electrical resistivity (ρ), Hall mobility (μ) and carrier concentration (n) of the films on the sputtering pressure is shown in figure 2.17. The decrease of electrical resistivity in the sputtering pressure range 3×10^{-2} - 6×10^{-2} mbar was related to the increase of Hall mobility which is caused by the reduction in the electron scattering from the grain boundaries due to improvement in the crystallinity of the films. At high sputtering

pressures, the gas density is high and the sputtered zinc atoms can only reach the substrate with more collisions leading to produce nearly stoichiometric zinc oxide films resulting in the increase of electrical resistivity.

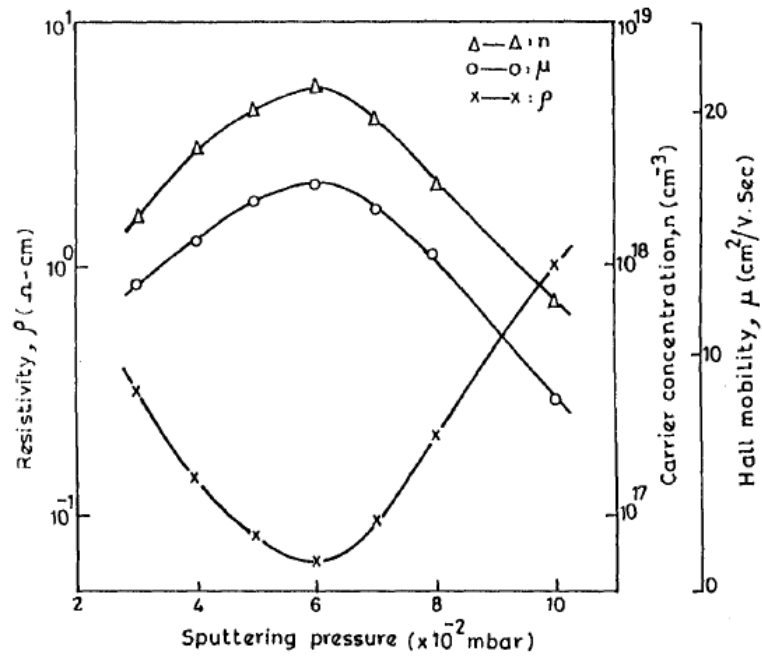


Figure 2.17 Dependence of resistivity, carrier concentration and Hall mobility with sputtering pressure [48].

On optical properties

From literature we know that the optical properties of a semiconductor are connected with both intrinsic and extrinsic effects [11,50]. Intrinsic optical transitions take place between the electrons in the conduction band and holes in the valence band, including excitonic effects due to the Coulomb interaction. The chief condition for exciton formation is that the group velocity of the electron and hole be equal [21]. Excitons are classified into free and bound

excitons. In high-quality samples with low impurity concentrations, the free exciton can also exhibit excited states, in addition to their ground-state transitions. Extrinsic properties are related to dopants or defects, which usually create discrete electronic states in the band gap, and therefore influence both optical-absorption and emission processes.

As we mentioned lines above from band structure that the ZnO is a direct band semiconductor and a transparent conductive. Reason by which, optical transitions in ZnO have been studied by a variety of experimental techniques such as optical absorption, transmission, reflection, photoreflexion, spectroscopic ellipsometry, photoluminescence, etc.

We will start with the revision about the influence of the parameters of sputtering deposition of ZnO films on optical transmittance by its importance in most optical applications in the visible range and to have direct relation with the used techniques of evaluation in this work.

Several works report results about transmittance of ZnO and Al-doped ZnO films for their comparison showing that all ZnO films are in general highly transparent (> 85%) between the wavelength range of 300 and 2500 nm [1,13,28,38,39,48,49]. For example, T.K. Subramanyam *et al.* [48] reported that the transmittance is high in the visible region and depends on the sputtering pressure (Figure 2.18a). The optical transmittance of the films (at $\lambda = 500$ nm) increased from 80% to 85% with the increase of sputtering pressure from 3×10^{-2} mbar to 6×10^{-2} mbar, then decreased to 73% as the sputtering pressure increased to 10×10^{-2} mbar. The optical band gap of the films increased from 3.24 eV to 3.32 eV with

increase in sputtering pressure from 3×10^{-2} mbar to 10×10^{-2} mbar (Figure 2.18b). The optical band gap is defined as the minimum energy needed to excite an electron from the valence band to the conduction band [9]. Widening of band gap with the increase of sputtering pressure might be due to the increase of the carrier density in addition to Moss-Burstein shift. The Burstein-Moss effect is present in direct (vertical) transitions type and was observed that the optical band gap increases in energy with increasing impurity concentrations [9]. Such a widening of the band gap was also noticed earlier in non-stoichiometric ZnO films [51].

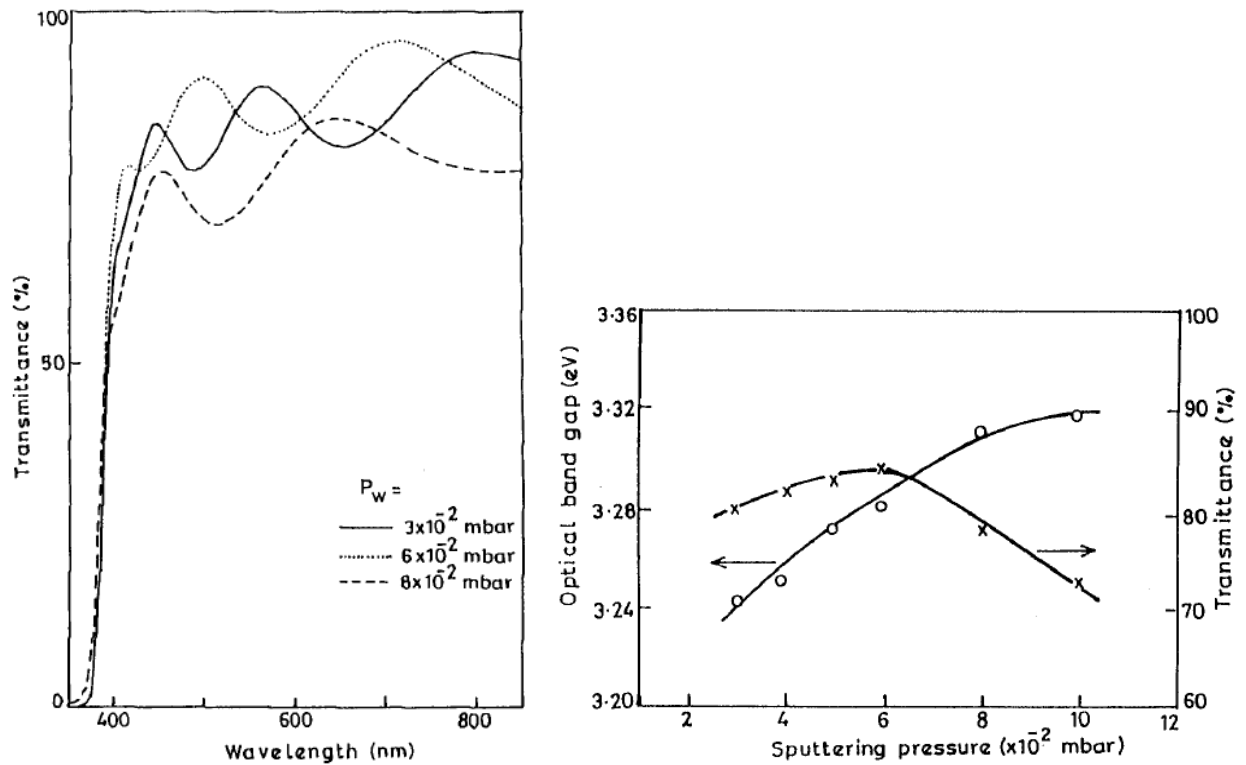


Figure 2.18 (a) Optical transmittance spectra of ZnO films formed at different sputtering pressures (b) Increase in the optical band gap of ZnO films with increasing sputtering pressure [48].

On the other hand, S. Bose et al. [38] observed however that the transmittance of the films did not change significantly with variation in substrate temperature and pressure, but observed that with the increase in power from 60 to 140 W the transmittance decreases from 95% to 85% which was associated with a decrease in carrier concentration due an increase in concentration of ionized impurities. The increase in impurity scattering will reduce the carrier relaxation time, which is inversely proportional to the carrier absorption [52].

J. H. Jeong et al [1] made a study systematic about the influence of deposition parameters by rf magnetron sputtering such as thickness (Figure 2.19a), target-substrate distance (Figure 2.19b) and Al content from Al(OH)₃-doped ZnO targets (Figures 2.19c and 2.19d) on transmittance. They found that the transmittance decreased when deposition time increased and target-substrate distance decreased due to the thickness effect, which leads to a decrease in light scattering losses. Also showed that as the Al(OH)₃ content increases in the target, the absorption edge shifted monotonically to shorter wavelength region widening (blue shift) the optical band gap due possibly at the Burstein effect [9] (Figure 2.19d).

Similar results was found by K. Ho Kim et al [39] for ZnO and Al-doped ZnO films prepared from targets having different Al₂O₃ at substrate temperature ($T_s = 150^\circ\text{C}$), work pressure ($P_w = 2 \text{ mTorr}$) and rf power ($P_{rf} = 150 \text{ W}$). Also was observed a change on optical band gap from α^2 vs $h\nu$ on films at different substrate temperatures ($P_w = 2 \text{ mTorr}$, $P_{rf} = 150 \text{ W}$ and 3 wt% Al₂O₃ content in target) (Figure 2.20).

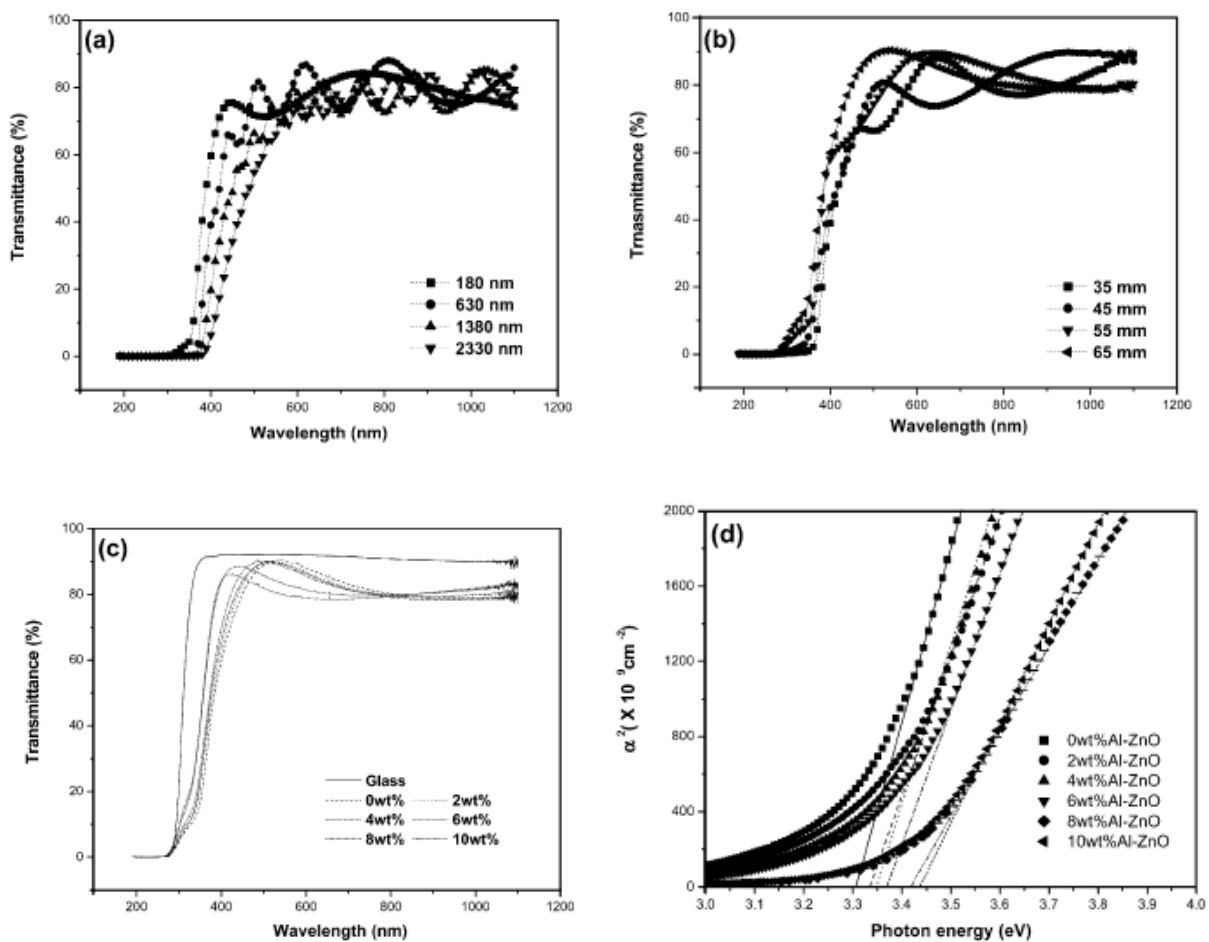


Figure 2.19 Influence the thickness (a), substrate to target distance (b) and content Al(OH)₃-doped ZnO targets on transmittance of Al-doped ZnO films (c). (d) Blue shift the optical band gap by Al(OH)₃ content in the ZnO target [1].

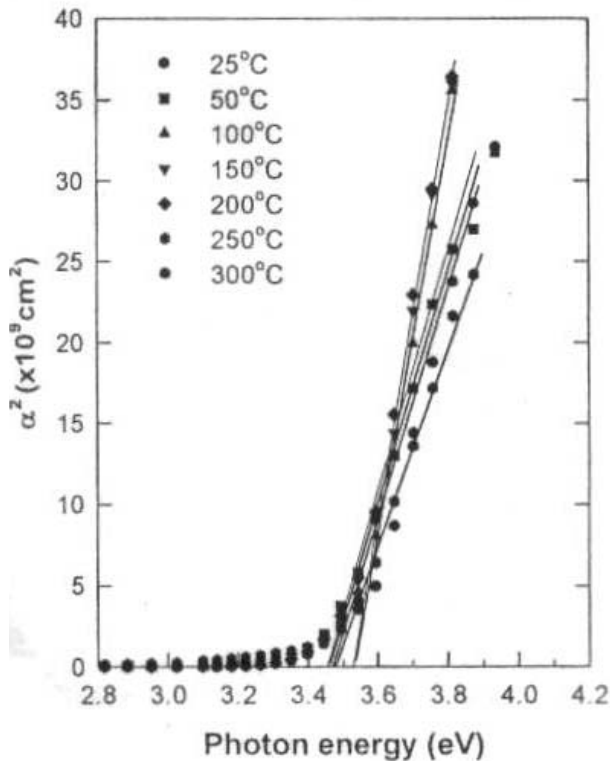


Figure 2.20 Relation between α^2 vs $h\nu$ for Al-doped ZnO films prepared at different substrate temperatures [39].

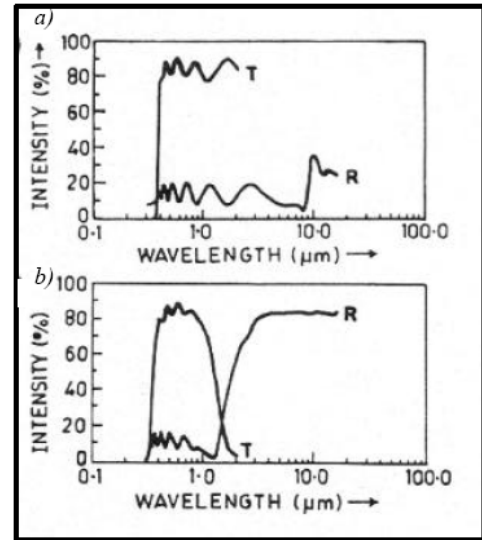


Figure 2.21 Transmittance and reflectance of (a) undoped ZnO and (b) Al-doped ZnO films [3].

Reflection like the transmission also is dependent on the doping of ZnO film. The transmission and reflection spectrums are shown in Figure 2.21 for aluminium doped and undoped ZnO where can be observed that the transmission drops from about 82% in the visible region to zero in the infrared part of the spectrum for the doped case. This drop in transmission is known as free carrier absorption. This type of absorption is dominated by the high free carrier concentration in the layers [3].

CHAPTER 3

Magnetic properties of dilute magnetic semiconductors oxides

3.1 Introduction

Magnetic and electromagnetic properties of materials and particularly, of thin films are used extensively. Applications include actuators, storage devices, memory devices, smart sensors and motors. Before we can begin our discussion of magnetic materials and about diluted magnetic semiconductors (DMS) we need to understand some of the basic concepts of magnetism, such as what causes magnetic fields, and what effects magnetic fields have on their surrounding.

3.2 Phenomenology

Magnetization

When a magnetic field, H , is applied to a material, the response of the material is called magnetic induction or flux density, B . The relationship between B and H is property of the material. The equation relating B and H is (in cgs units):

$$B = H + 4\pi M \quad 3.1$$

where M is the magnetization of the medium. The magnetization is defined to be the magnetic moment per unit volume,

$$M = m/V \quad [\text{emu/cm}^3], \quad 3.2$$

M is a property of the material, and depends on both the individual magnetic moments of the constituent ions, atoms or molecules, and on how these dipole moments interact with each other. The cgs unit of magnetization is the emu/cm³, and that of magnetic induction is the gauss.

In SI units the relationship between B , H and M is

$$B = \mu_0 (H + M) \quad 3.3$$

where μ_0 is the permeability of free space. The units of M are obviously the same as those of H (A/m) and those of μ_0 are weber/A.m, also known as henry/m. So the units of B are weber/m², or Tesla (T); 1 Tesla = 10⁴ Gauss.

Susceptibility and permeability

The properties of a material are defined not only by the magnetization, or the magnetic induction, but by the way in which these quantities vary with the applied magnetic field.

The ratio of M to H is called the susceptibility:

$$\chi = \frac{M}{H} \quad \left[\frac{\text{emu}}{\text{cm}^3 \text{Oe}} \right] \quad 3.4$$

therefore,

$$\frac{B}{H} = \mu_0(1 + \chi) \quad 3.5$$

The susceptibility indicates how responsive a material is to an applied magnetic field. The ratio of \mathbf{B} to \mathbf{H} in the equation 3.5 is called the permeability, i.e.:

$$\mu = \frac{B}{H} \quad \left[\frac{\text{gauss}}{\text{Oe}} \right] \quad 3.6$$

and μ indicates how permeable the material is to the magnetic field. A material which concentrates a large amount of flux density in its interior has a high permeability. Using the relationship $\mathbf{B} = \mathbf{H} + 4\pi\mathbf{M}$ gives us the relationship (in cgs units) between the permeability and susceptibility:

$$\mu = 1 + 4\pi\chi \quad 3.7$$

Note that in SI units, the susceptibility is dimensionless, and permeability is in units of henry/m. The corresponding relationship between permeability and susceptibility in SI units is:

$$\frac{\mu}{\mu_0} = 1 + \chi \quad 3.8$$

where μ_0 is the permeability in free space.

Graphs of \mathbf{M} or \mathbf{B} versus \mathbf{H} are called magnetization curves, and are characteristic of the type of material. Let's look at a few, for the most common types of magnetic materials.

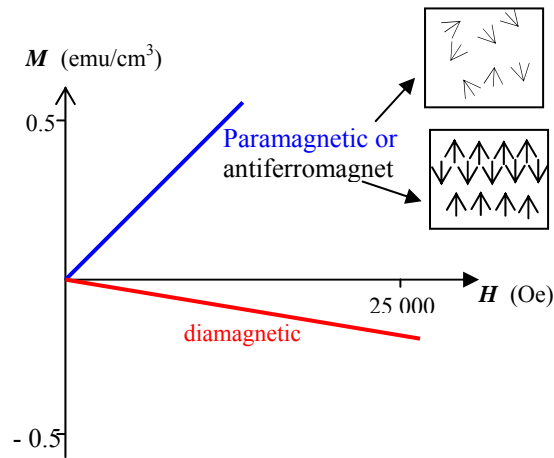


Figure 3.1 Magnetization curves for dia-, para- and antiferromagnets

The magnetization of diamagnetic, paramagnetic and antiferromagnetic materials is plotted schematically as a function of applied field in Figure 3.1. For all these materials the M - H curves are linear. Rather large applied fields are required to cause rather small changes in magnetization, and no magnetization is retained when the applied field is removed. For diamagnets, the slope of the M - H curve is negative, so the susceptibility is small and negative, and the permeability is slightly less than one. For para- and antiferromagnets the slope is positive and the susceptibility and permeability are correspondingly small and positive, and slightly greater than unity respectively.

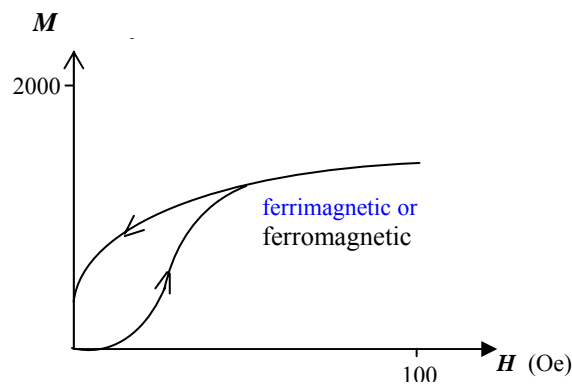


Figure 3.2 Magnetization curves for ferri- and ferromagnets

Figure 3.2 shows schematic magnetization curves for ferri- and ferromagnets. The first point to note is that the axis scales are completely different from those in Figure 3.1. In this case, a much larger magnetization is obtained on application of a much smaller external field. Second, the magnetization saturates – above a certain applied field, an increase in field causes only a very small increase in magnetization. Clearly both χ and μ are large and positive, and are functions of the applied field. Finally, decreasing the field to zero after saturation does not reduce the magnetization to zero. This phenomenon is called *hysteresis*, and is very important in technological applications. For example the fact that ferro- and ferrimagnetic materials retain their magnetization in the absence of a field allows them to be made into permanent magnets.

Hysteresis loop of thin films

We have just seen that reducing the field to zero does not reduce the magnetization of a ferromagnet to zero. In fact ferro- and ferrimagnets continue to show interesting behavior when the field is reduced to zero and then reversed in direction. The graph of \mathbf{M} versus \mathbf{H} which is traced out is called a *hysteresis loop* (Figure 3.3). Each atom of a magnetic material can be thought of as being a miniature magnet that aligns with, repels, or is not affected by the application of a magnetic field. In case of a film, the permeability is measure of how fast and the degree to which it can be magnetized. The maximum magnetization of a film is the saturation magnetization (\mathbf{M}_S). Properties such as low coercivity (\mathbf{H}_C) let a magnetic film be magnetized and demagnetized easily. High retentivity (\mathbf{M}_R) lets the film hold its

magnetization when the external field is removed. A hard magnetic material retains its magnetization and is hard to demagnetize (high H_C) while a soft magnetic material is easily demagnetized (low H_C). A soft magnetic material would be used for read-write applications and for audio recording where the tape must be erased to rerecord music [53]. Common soft materials are Ni-Fe alloys, Mn-Zn ferrites (magnetic insulators) and Ni-Zn ferrites. Hard magnetic materials such as Al-Ni-Co alloys and NdB alloys would be used in a computer hard drive [54]. A medium hard film such as FeO_2 would also be used for recording applications. Ferromagnetic material can be demagnetized by heating them above their Curie temperature T_c . The magnetic domains become disordered with no net magnetization. Typical T_c 's are 1042 K for Fe, 1388 K for Co, 627 K for Ni, and 585 K for $Nd_2Fe_{12}B$ [53]. A ferromagnetic material and thin film can be re-magnetized if it is heated above T_c by simply exposing it to a strong magnetic field.

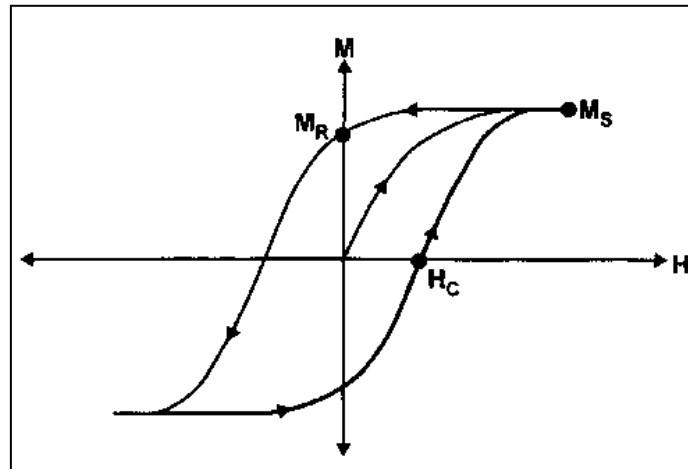


Figure 3.3 Hysteresis loop for the magnetization of a magnetic material

Because the films can be the thickness of a magnetic domain, their magnetic properties can be anisotropic [55]. Some materials are more easily magnetized in certain directions than others. The source of this anisotropy can be the crystal structure, bulk shape of the material and stress (deformation). A material is much easier to magnetize in the plane of the film than across the plane. This is known as shape anisotropy [56]. In some materials, it is 125,000 times easier to magnetize in the plane than transverse to the plane [53].

Magnetic thin films are deposited primarily by PVD, PECVD, and Magnetron sputtering process. When magnetrons are used, because a magnetic target shunts the magnetic field of the magnetron, the sputtering target must be thin or the magnetic field must be beefed up. However, magnetron sputtering system is especially useful for magnetic films on flexible substrates.

Zeeman effect

When a magnetic field is applied to a semiconductor, the energy of electrons and holes with their spin magnetic moments parallel to the field is lowered, and that of the antiparallel electrons and holes is raised. The difference in energy between the electron-hole pairs of opposite spin polarization is known as the Zeeman splitting [56]. A clear example of a normal Zeeman splitting of a transition between an s orbital and a p orbital is shown in Figure 3.4a. In the absence of an applied field, the s and p orbitals each have one energy level. The s energy level does not split when a field is applied, since the s electron has no orbital

angular momentum and therefore no orbital magnetic moment. The p level, on the other hand, splits into three, corresponding to m_l values of $-1, 0$ and 1 . As a result three lines are observed in the normal Zeeman spectrum. In fact only atoms with a total spin angular momentum equal a zero show the normal Zeeman effect.

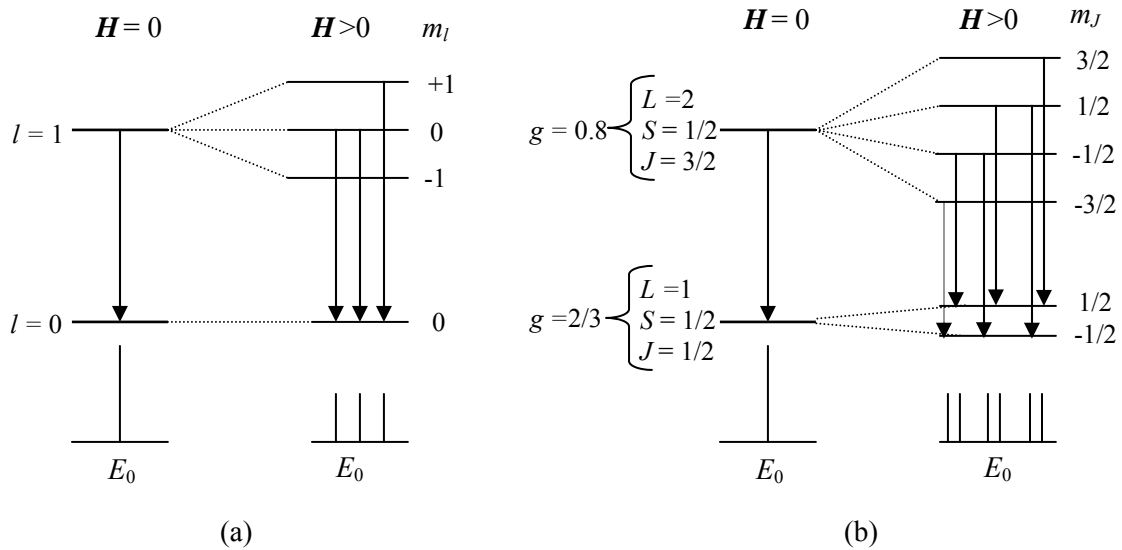


Figure 3.4 (a) Normal Zeeman effect for a transition between s and p orbitals (b) Transition in the anomalous Zeeman effect.

Much more common is the so-called *anomalous Zeeman effect*, which gives a more complex arrangement of lines in the spectrum, and is consequence of spin-orbit coupling (Figure 3.4b). The additional complexity arises because the splittings of the upper and lower levels of the transition are unequal. The ultimate reason for the unequal splittings is the anomalous g -factor of the electron ($g_e = 2.0023$) [9]. Because g_e is rather than 1, the total angular momentum, \mathbf{J} , and the total magnetic moment, $\boldsymbol{\mu}_m$, of the atom are not collinear. So the

magnitude of the total magnetic moment along the field axis (which determines the energy change in the presence of a magnetic field) is a function of spin momentum angular S , orbital angular momentum L and J , rather just of J . In fact, if we work through the mathematics [9], we obtain:

$$\mu_m = -g\mu_B m_J \quad 3.9$$

Here μ_B is called the Bohr magneton, and is the unit of orbital magnetic moment in an atom. Its value is 9.274×10^{-24} J/T and,

$$g = 1 + \frac{J(J+1) + S(S+1) - L(L+1)}{2J(J+1)} \quad 3.10$$

is called the Landé g -factor or the *spectroscopic splitting factor*. $m_J = J, J-1, \dots, -J$ is the quantum number, representing the projection of the total angular momentum, \mathbf{J} , onto the field axis. The corresponding expression for the magnitude of the total magnetic moment is $\mu_m = g\mu_B \sqrt{J(J+1)}$.

When $S = 0$, then $g = 1$ (because $J = L$) and so the magnetic moment is independent of L and the upper and lower levels are split by the same amount. In this case we observe the normal Zeeman effect, as we described before. However, when $S \neq 0$, the value of g depends on both L and S , and so the upper and lower levels in the spectroscopic transition are split by different

amounts. This is illustrated in Figure 3.4b. Note that the allowed transitions are further restricted by the angular momentum conservation selection rules $\Delta m_J = 0$ (corresponding to emission of linearly polarized light) or ± 1 (circularly polarized light).

Most of the initial work in Diluted Magnetic Semiconductor (DMS) was focused on II–VI semiconductors in which a fraction of the group II sub-lattice was randomly replaced by Mn atoms. The Mn^{2+} ions become magnetized in the presence of an applied magnetic field. Thus, in addition to the external field, the electrons and holes feel a large magnetization from Mn^{2+} ions. This results in a Zeeman splitting that can be hundreds of times larger than that in non-magnetic semiconductor quantum structures. This, in turn, results in a giant Faraday rotation, which means that II-VI DMSs have potential application as magneto-optic materials with large magneto-optic coefficients [56].

CHAPTER 4

Experimental Procedure

4.1 Introduction

The synthesis of quality thin films onto substrates requires careful optimization. In this chapter, the various processing steps as well the specific experimental details followed during the deposition by magnetron sputtering technique of the respective thin films, are described in detail. The optimization step was achieved through the influence of deposition parameters such as substrate to target distance, rf power on the structural, optical and electrical properties on ZnO films.

Another important aim of this study was the characterization of the semiconductors ZnO and Co, Fe-doped ZnO films. The techniques used to investigate the structural features of the films were X-ray diffraction (XRD), Raman spectra, atomic force microscopy (AFM) and scanning electron microscopy (SEM). The thickness was obtained through a profilometer. The optical features of the films were investigated by transmission through UV-vis absorption spectroscopy. The optical band gap was obtained from plot α^2 vs $h\nu$. The $M-H$ curves of the Co-doped and Co,Fe-doped ZnO ZnO films were measured using a Superconducting Quantum Interference Device (SQUID) at 300 K.

4.2 Preparation of the substrates

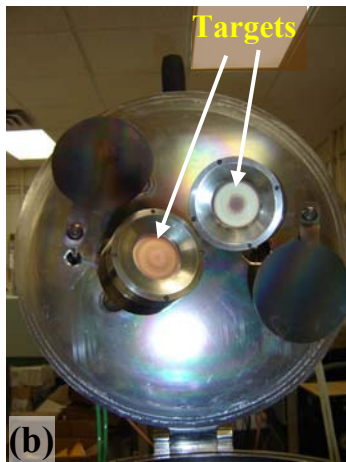
In this study, glass microscope slides and commercial grade fused quartz were used as substrate material, both 1 mm thicknesses. The glass substrates were cut into standard sizes of 10 x 10 mm, while the dimensions of quartz substrates were 12.7 mm of diameter as were acquired. All substrates were ultrasonically cleaned in acetone and dried into oven until it was loaded into the chamber deposition.

4.3 Description of magnetron sputtering system:

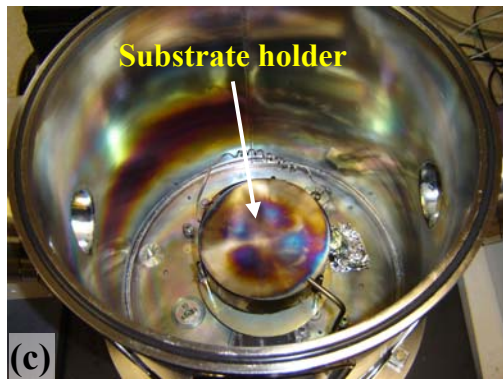
The magnetron sputtering system used in this study has a configuration on-axis with two magnetron sputter guns for two modes sputtering process: direct current (DC) and radio frequency (RF) magnetron. Figure 4.1a depicts a complete overview of the system. The process chamber is made of 304-grade stainless steel with cylindrical design 16” diameter x 16” high with full opening top plate for easy access to all internal parts – the guns for changing targets, substrate stage for loading and unloading samples. Figures 4.1b and 4.1c represents close up views of targets and substrate holder. The two magnetron guns of 2” diameter with shutters are mounted on the plate at 65 degree angle. The guns can be adjusted linearly to vary the distance between the substrate and the guns. The Chamber has two view ports at 70 degrees and at convenient height to monitor the substrate with ellipsometry. An additional 4 in view port has been provided in the front for process monitoring.



(a)



(b)



(c)

Figure 4.1 (a) Photograph of the magnetron sputtering system used in this study (b) top plate of chamber showing the targets (c) the process chamber.

The vacuum pumping system consists of a Varian 200 l/s turbo molecular pump, a 4 in manually operated stainless steel gate valve with a two stage direct drive rotary vane. The system has two gas inlets (one for oxygen, the other for argon) controlled by needle valves. A cold cathode combination gauge is provided for measuring vacuum ($760 - 10^{-8}$ Torr). A stainless steel substrate holder capable of mounting up to 4 in diameter wafer/sample is provided. It is capable of being heated up to 400 degree Celsius. Figure 4.2 is a schematic representation of the deposition system into the process chamber.

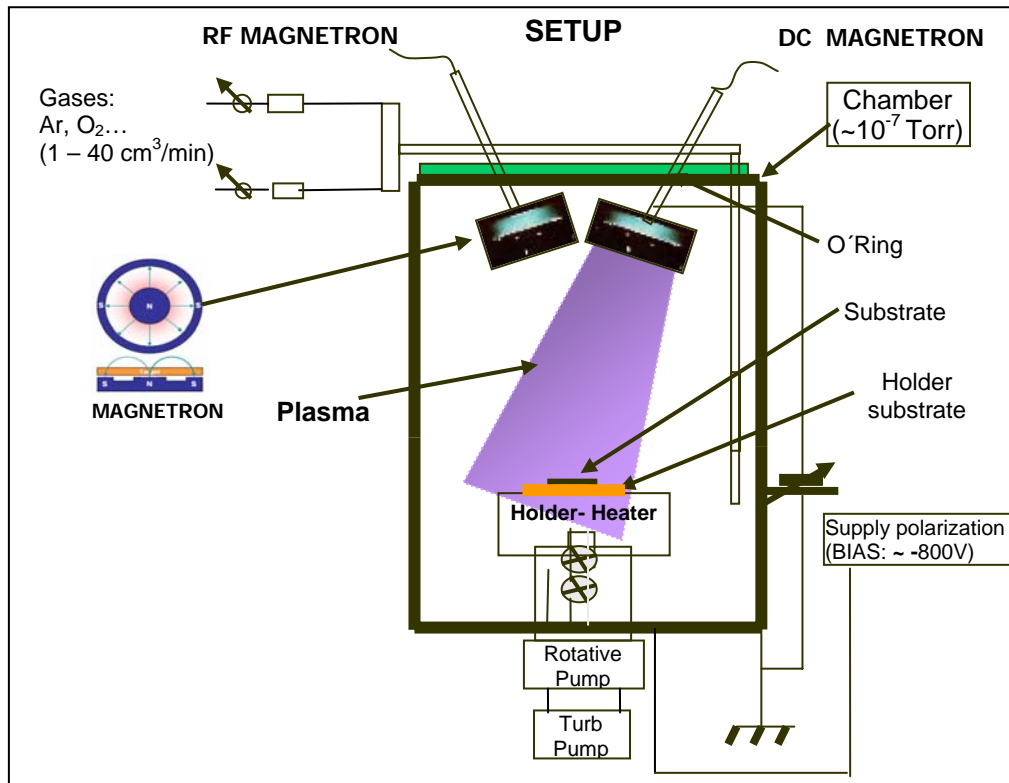


Figure 4.2 Schematic representation of the sputtering environment.

4.4 The sputtering targets

In this study, sintered ceramic discs of ZnO, Aluminum and ZnO mixed with Co, Fe with dimensions of 2 inch diameter x 0.125 inch thick were used as sputtering targets. The composition of each target is shown in the Table 4.1.

Table 4.1 Composition and purity of the sputtering targets used for films deposition.

Sputtering targets	Purity*
Aluminum (Al)	99.99
Zinc oxide (ZnO)	99.99
Zn _{0.90} Co _{0.10} O at. %	99.99
Zn _{0.85} [Co _{0.50} Fe _{0.50}] _{0.15} O at. %	99.99

* Purity provided by the manufacturer: Super conductor Materials, Inc.

4.5 Sputtering deposition procedure of ZnO films

Given the complexity of the deposition processes and in order to optimize the quality of the films in study, this first step consisted in carrying out a systematic study about of the evaluation the structural features and optical properties of ZnO films as function of substrate to target distance and rf power. The effect of Al-content in ZnO on the conductivity also was studied.

4.5.1 Substrate to target distance

In order to optimize the best location of the substrates on holder, the influence of the substrate to target distance on the structural and optical properties of ZnO films produced by

RF magnetron sputtering in argon atmosphere was studied. The ZnO films were grown during 90 min onto glass microscope slides located diametrically on the top plate substrate holder as shown in the Figure 4.3. The position zero indicated in this figure is considered as the point of reference and represents a point exactly in the vertical projection below center of the sputtering target. The base pressure in the chamber and the working pressure were $\sim 1.0 \times 10^{-4}$ Torr and 9.0×10^{-3} Torr, respectively. The rf power and the temperature were 100 W and $296 \pm 2^\circ\text{C}$ respectively. This temperature was measured with one thermocouple which was in contact with the top plate of the substrate holder. The evaluation to each ZnO film was carried out on cut pieces of 10 mm x 10 mm from glass microscope slides after deposition.

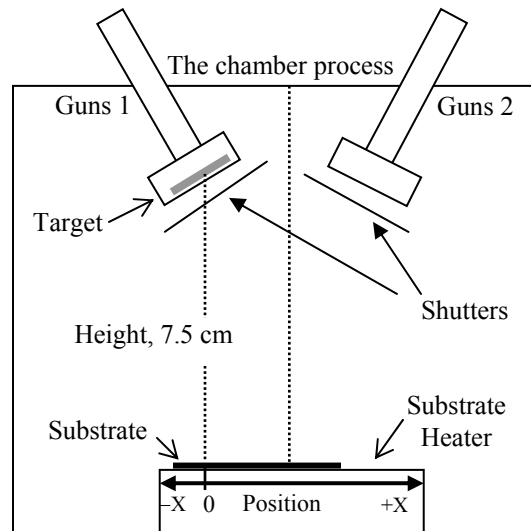


Figure 4.3 Schematic representation of the position of the glass microscope slide in relation to substrate to target distance.

4.5.2 Radio frequency power (P_{rf}) sputtering deposition

From the preceding study, the optimum position on substrate holder of the substrates with respect to the target distance was determined. A series of films were synthesized under argon atmosphere with rf power between 25 and 150 W, while the substrate temperature (T_s) and the working pressure (P_w) were kept constants and equal at: $T_s = 198 \pm 1^\circ\text{C}$, $P_w = 8.5 \times 10^{-3}$ Torr. All samples were deposited onto glass during 30 min.

4.5.3 Doping of ZnO film with Aluminum (Al) by co-sputtering deposition

In order to investigate the effect of Al-content on the electrical conductivity in ZnO films, the films were grown on glass during 90 min by co-sputtering (using rf magnetron and dc magnetron simultaneously) with 100 W rf power for ZnO ceramic target and dc power 68 W, -787 V and 89 mA for aluminum metallic target. The base pressure in the chamber and the working pressure were $\sim 1.0 \times 10^{-4}$ Torr and 9.0×10^{-3} Torr, respectively. The growth temperature was $296 \pm 2^\circ\text{C}$.

4.6 Sputtering deposition procedure of Co-doped ZnO and Co, Fe-doped ZnO films

$\text{Zn}_{0.90}\text{Co}_{0.10}\text{O}$ and $\text{Zn}_{0.85}(\text{Co}_{0.50}\text{Fe}_{0.50})_{0.15}\text{O}$ films were synthesized by rf magnetron sputtering onto fused quartz from $\text{Zn}(0.90)\text{Co}(0.10)\text{O}$ at.% and $\text{Zn}(0.85)[\text{Co}(0.50)\text{Fe}(0.50)](0.15)\text{O}$ at.% ceramic targets respectively. Argon was used as working gas. The sputtering chamber was evacuated with a turbomolecular pump to base pressure below 10×10^{-5} Torr. The substrate

temperatures were between 200 and 300°C and the chamber pressure was fixed at 8.5×10^{-3} Torr. The growth of films was carried out during 90 minutes with 125 W rf power. These conditions of sputtering were considered after the systematic study made in the first step of this work.

4.7 Characterization of the films:

4.7.1 Introduction

In this study, a variety of characterization techniques were used to evaluate the structural, optical, electrical and magnetic properties of the thin films. Of particular interest was the determination of the structure from X-ray diffraction, the film thicknesses, optical parameters, the conductivity of the various films and determination of the magnetic parameters. As important, were the investigation about of the morphological features by atomic force microscope (AFM), scanning electron microscope (SEM) and determination of grain size. The most relevant aspects of these analytical techniques are discussed briefly in the following sections.

4.7.2 Determination of film thickness

Use of a profilometer

The profilometer measures the vertical depth of a material across a specified horizontal length. In this study a KLA-Tencor Alpha Step IQ Surface Profiler for measurements of thicknesses of the films was used (see Fig 4.4). This system moves a small needle, called a

stylus, across the surface of a device and generates a profile based on the deflection of the needle. In this case, the film thickness was obtained by the step height between the deposited film and an area that was masked during the sputtering deposition. The profile is displayed on a printable graphical interface.

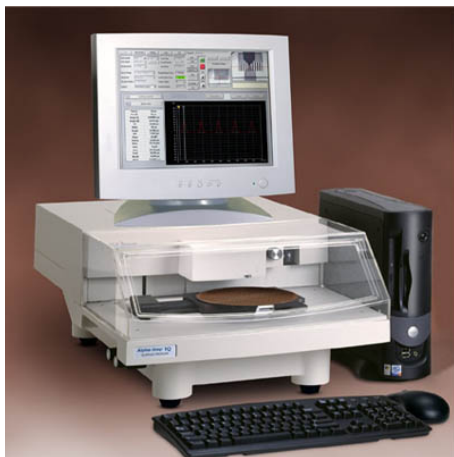


Figure 4.4 Profilometer used for measures the thicknesses of the films (NAMAS-Lab of the Mathematic Physics Department of UPR-Cayey).

4.7.3 Structural characterization

4.7.3.1 X-ray diffraction (XRD)

X-ray powder diffraction (XRD) is one of the most powerful techniques for qualitative and quantitative analysis of crystalline compounds. This experimental technique has long been used to determine the overall structure of bulk solids, including lattice constants, identification of unknown materials, orientation of single crystals, orientation of polycrystals, defects, stresses, etc. In this study a Kristalloflex-Siemens, DACO-MP, power diffraction system with Cu-K α x-ray tube ($\lambda = 1.54056 \text{ \AA}$) was used. The x-ray scans were performed between 2θ values of 15° and 75° with a typical step size of about 0.02° .

Basic fundamentals:

X-rays:

The relation between energy, frequency or wavelength in the case of photons is:

$$\varepsilon = h\nu = \frac{hc}{\lambda}, \quad 4.1$$

where $h = 6.62 \times 10^{-27}$ erg-s (6.62×10^{-34} J-s) is Planck's constant. Therefore, from equation 4.1, λ in laboratory units is,

$$\lambda(\text{\AA}) = \frac{12.4}{\varepsilon(\text{KeV})} \quad 4.2$$

Photons of 10 [KeV] are called X-rays. Since X-rays are produced whenever high-speed electrons collide with a metal target, any x-ray tube must contain (a) a source of electrons, (b) a high accelerating voltage, and (c) a metal target. All x-ray tubes contain two electrodes, an anode (the metal target) maintained, with few exceptions, at ground potential, and a cathode, maintained, at a high negative potential, normally of the order of 30 KV to 50 KV for diffraction work. A continuous spectrum is formed when the high-speed electrons are slowed down rapidly by multiple collisions with the anode material, this gives rise to white radiation, or so called *Bremsstrahlung* [57] (Figure 4.5). The continuous spectrum results from the rapid deceleration of the electrons hitting the target since, as mentioned above, any decelerated charged emits energy. Not every electron decelerates in the same way, however; some stop in one impact and release all their energy at once, while others deflect this way and that when they encounter atoms of the target, successively losing fractions of their total

kinetic energy until is all spent. Those electrons which are stopped in one impact produce photons of maxim energy, i.e. x-rays of minimum wavelength (wavelength characteristic, λ).

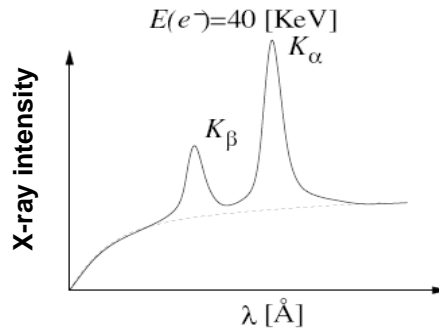


Figure 4.5 X-ray spectrum, with a bremsstrahlung background and electrons excitations.

Bragg's law

We consider a series of parallel lattice planes spaced equal distances d apart as show in Figure 4.6. The radiation is incident in the plane of the paper. The path difference for rays reflected from adjacent planes is $2d \sin\theta$, where θ is measured from the plane. Constructive interference of the radiation reflected from successive planes occurs whenever the path difference is an integral number n of wavelengths, λ . Thus the condition for constructive reflection of the incident radiation is:

$$n \lambda = 2 d \sin \theta \tag{4.3}$$

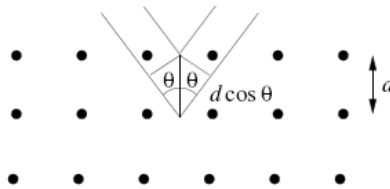


Figure 4.6 Bragg's diffraction conditions.

This is the Bragg law which is a consequence of the periodicity of the space lattice. This law does not refer to the arrangement or basis of atoms associated with each lattice point. The composition of the basis determines the relative intensity of the various orders n of diffraction from given set of parallel planes. Bragg reflection can occur only for wavelengths $\lambda \leq 2d$, since $(n\lambda/2d) \leq 1$.

An X-ray diffractogram is generated when the conditions for Bragg's law are met. The crystalline phases and orientation were identified by matching the XRD peaks with those given in several publications related with this study and in with those given in the data base of the program MATCH [58].

Crystallite size measurement

Phase identification using x-ray diffraction relies mainly on the positions of the peaks in a diffraction profile and to some extent on the relative intensities of these peaks. However, as practical aspect of diffraction from material, it is valuable to consider how diffraction peaks are altered by the presence of various types of defects such as small number of dislocations in crystals with dimensions of millimeters. Small crystal o grain size can be considered as another kind of defect and can alter diffraction peak widths. Very small crystals cause peak broadening. The well known Scherrer equation explains peak broadening in terms of incident beam divergence which makes it possible to satisfy the Bragg condition for non-adjacent diffraction planes. The crystallite size is easily calculated as a function of peak width

(specified as the full-width at half maximum peak intensity (FWHM)), peak position and wavelength.

Scherrer's formula. Suppose that the crystal has a thickness δ measured in a direction perpendicular to a particular set of Bragg planes (Figure 4.7). Let there be $(m + 1)$ planes in this set. Define the Bragg angle θ as a variable and let θ_B be the angle which exactly satisfies Bragg's law for the particular values of λ and d involved, or

$$\lambda = 2d \sin \theta_B \quad 4.4$$

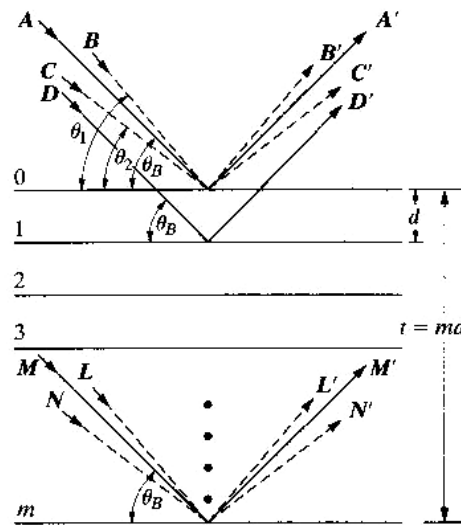


Figure 4.7 Effect of crystal size on diffraction [57]

In the Figure 4.7, rays A, D, ..., M make exactly this angle θ_B with the diffraction planes. Incident x-rays that make angles only slightly different from θ_B , produce incomplete destructive interference. Ray B, for example, makes a slightly larger angle θ_1 , such that ray

L' from the m th plane below the surface is $(m + 1)$ wavelengths out of phase with B' , the ray from the surface plane. The intensity of the beam diffracted at an angle $2\theta_1$ is therefore zero. It is also zero at an angle $2\theta_2$ where θ_2 is such that ray N' from the m th plane below the surface is $(m - 1)$ wavelengths out of phase with ray C' from the surface plane. This defines, therefore, the two limiting angles, $2\theta_1$ and $2\theta_2$, at which the diffracted intensity must drop zero. The curve of diffracted intensity vs. 2θ will thus have the form of Figure 4.8a in contrast to Figure 4.8b, which illustrates the hypothetical case of diffraction occurring only at the exact Bragg angle.

The width of the diffraction curve of Figure 4.8a increases as a thickness of the crystal decreases, because the angular range $(2\theta_1 - 2\theta_2)$ increases as m decreases. The width B is usually measured, in radians, at an intensity equal to half the maximum intensity (FWHM).

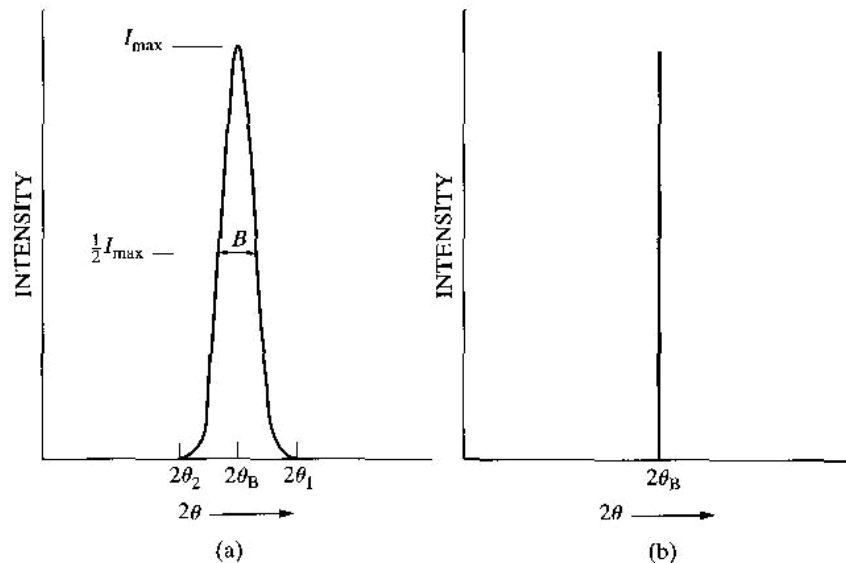


Figure 4.8 Effect of fine crystallite size on diffraction curves [57]

Therefore,

$$B = \frac{1}{2}(2\theta_1 - 2\theta_2) = \theta_1 - \theta_2 \quad 4.5$$

The path-difference equations for these two angles are similar to equation 4.4 but related to the entire thickness of the crystal rather than to the distance between adjacent planes:

$$2\delta \sin \theta_1 = (m+1)\lambda, \quad 4.6$$

$$2\delta \sin \theta_2 = (m-1)\lambda \quad 4.7$$

By subtraction,

$$\delta(\sin \theta_1 - \sin \theta_2) = \lambda \quad 4.8$$

$$2\delta \cos\left(\frac{\theta_1 + \theta_2}{2}\right) \sin\left(\frac{\theta_1 - \theta_2}{2}\right) = \lambda \quad 4.9$$

But θ_1 and θ_2 are both very nearly equal to θ_B , so that

$$\theta_1 + \theta_2 = 2 \theta_B \text{ (approx.)}$$

and

$$\sin\left(\frac{\theta_1 - \theta_2}{2}\right) = \left(\frac{\theta_1 - \theta_2}{2}\right) \text{ (approx.)}$$

Therefore,

$$2\delta \left(\frac{\theta_1 - \theta_2}{2}\right) \cos \theta_B = \lambda \quad 4.10$$

or,
$$\delta = \frac{\lambda}{B \cos \theta_B}, \quad 4.11$$

A more exact treatment of the problem gives:

$$\delta = \frac{0.9\lambda}{B \cos \theta_B} \quad 4.12$$

which is known as Scherrer's formula [57]. It is used to estimate the size of very small crystals from measured width of their diffraction curves.

4.7.3.2 Atomic force microscopy (AFM)

Atomic force microscopy (AFM) is a method of measuring surface topography on a scale from angstroms to 100 microns. The technique involves imaging a sample through the use of a probe, or tip, with a radius of 20 nm. The tip is held several nanometers above the surface using a feedback mechanism that measures surface–tip interactions on the scale of nanoNewtons. A detector measures the cantilever movement as the tip moves over the sample. From these tip movements and data from the detector, a computer is used to reconstruct a map of the surface morphology. The forces that are responsible for the deflection of the tip, is shown in Figure 4.9 as function of tip to sample distance. This force most commonly associated with atomic force microscopy is an inter-atomic force called the

van der Waals force. In this study, an AFM Veeco di CP-II for evaluate the surface morphology of the thin films was used.

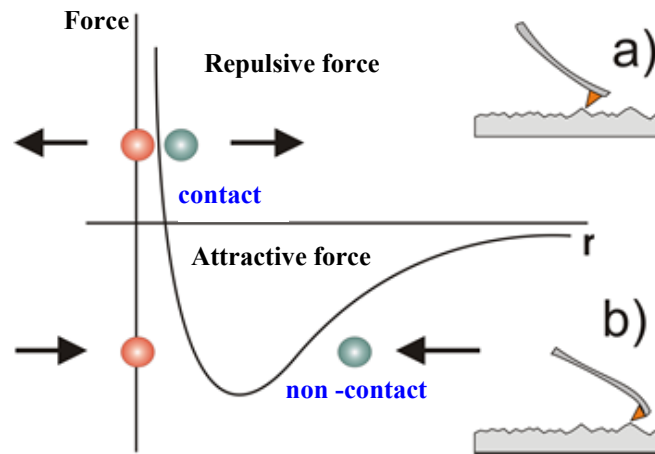


Figure 4.9 Interatomic force vs. distance curve. (a) repulsive force (b) attractive force.

These two regimes are (i) contact regime (soft physical contact) and (ii) the non-contact regime. In the contact regime, the tip is brought until there is a few angstroms between the sample and the tip. The force here is usually repulsive. In the non-contact regime the distance between the sample and the tip is held on the order of tens to hundreds of angstroms from the sample surface, and the inter-atomic force between the sample and tip is usually attractive (largely a result of long-range van der Waals interaction. In this study, the non-contact regime was used for morphologic analysis.

4.7.3.3 Scanning electron microscopy (SEM)

In this study, the morphological features of the various films were investigated with a JEOL JSM-6360 equipped with a EDAX detector. The SEM, is used in its common mode, the emission mode. In this mode, electrons fired from a filament (tungsten hairpin or LaB6) are accelerated with a voltage in the range of 1-30 kV down the center of an electron-optical column consisting of two or three magnetic lenses. The main aim of these lenses is to focus a fine electron beam onto the sample. Scanning coils placed before the final lens causes the electron spot to scan across the specimen surface in the form of a square raster. The current that passes through these coils are usually also made to pass through the deflection coils of the cathode ray tube or picked up as electronic signals and regenerated on a computer screen to generate the image.

Upon impinging on the specimen, there is an interaction between the atoms and electrons in the sample. This interaction causes various signals to be generated and the most commonly used signals are those from secondary and elastic back-scattered electrons. The secondary electrons are electrons of very low energy and thus contain information of only a few angstroms deep on the surface of the layer. These electrons are then detected by a detector consisting of a scintillator-photomultiplier combination, which in turn through the system electronics drive the cathode ray tube. These images are the ones commonly used in SEM to interpret the morphology of a sample.

4.7.3.4 Optical characterization of films

The optical absorption coefficient is defined as

$$I = I_0 \exp(-\alpha t) \quad 4.13$$

where I is the intensity of the transmitted light, I_0 is the incident light and t is the thickness of the film. The optical band gap (E_g) was calculated using the value of α in the following equation for direct band semiconductors:

$$\alpha(h\nu) \equiv \Lambda(h\nu - E_g)^{1/2} \quad 4.14$$

where h is Planck constant, and ν is the frequency of the incident photon, and Λ no depend of the frequency.

Transmittance was measured using a UV-vis DU 800 Spectrophotometer, Beckman Coulter.

4.7.3.5 Magnetic properties of films

Magnetic measurements were carried out using a Quantum Design superconducting quantum interference device (SQUID) MPMS Model 5S. The magnetic field was applied parallel to the film plane. Magnetometer SQUID is a detector of the flux of the high sensitivity based on

quantization of the flux of magnetic field that crosses a superconductive coil and on Josephson effect (Figure 4.10).

If a constant biasing current is maintained in the SQUID device, the measured voltage oscillates with the changes in phase at the two junctions, which depends upon the change in the magnetic flux. Counting the oscillations allows evaluating the flux change which has occurred [59].

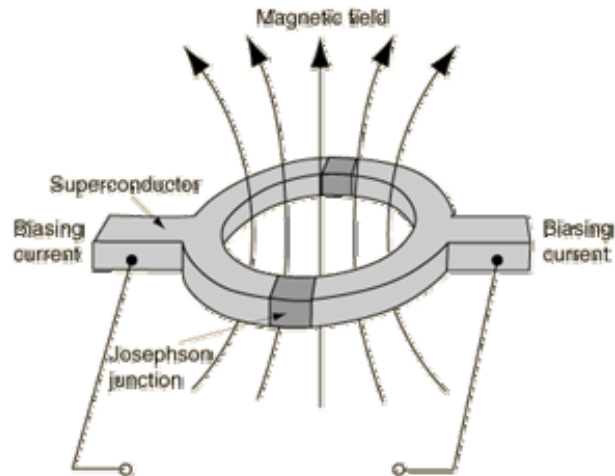


Figure 4.10 Superconducting quantum interference device (SQUID) as a simple magnetometer.

CHAPTER 5

Results and discussions

5.1 Introduction

One of the most important goals this study was considered also the optimization of the quality of the films evaluating first the influence of some external deposition parameters of magnetron sputtering technique such as substrate to target distance (substrate position on holder-heater) and rf power on structural, optical and electrical properties of ZnO films. Addition, this first step shows results the variation in resistivity as a function of temperature of Al-doped ZnO films growth by co-sputtering (rf and dc magnetron sputtering simultaneous) in pure argon atmosphere. Then, once evaluated this step, it was come to synthesize the Co, Fe-doped ZnO films for their respective characterization.

5.2 Sputtering deposition of ZnO films

5.2.1 ZnO thickness and deposition rate

In order to achieve high quality of the required films, it is important investigate the roles of the substrate to target distance (D_{st}) and radio frequency power (P_{rf}) on some physical properties on ZnO films synthesized by magnetron sputtering. D_{st} is referred at various points or substrate positions located along substrate-holder diameter as was described in the experimental procedure. In this study was observed that both parameters (D_{st} and P_{rf}) had a severe influence on thickness (t) and deposition rate (r) of ZnO films grown onto glass. The

thicknesses were determined by surface profilometry on partially coated of each substrate located along substrate-holder diameter while the deposition rate was obtained as ratio between the film thickness and the sputtering time. Immediately, we will discuss each one of these effects separately. Furthermore, the influence of these parameters on the optical and electrical properties also was study here.

The film thickness values for different substrate to target distances are shown in the Table 5.1. From this table we observe that the films thicknesses on the substrates located between -4 cm and 7 cm is approximately constants with mean value of 552.9 nm. But, from $x = 7$ cm is noted that the film thickness decreases notably from this mean value to 344.0 nm ($x = 10$ cm). This result, of course, it implies that the deposition rate will have a similar behavior such as it is possible to be observed in Figure 5.1. The position zero in this plot is considered as the point of reference and represents a point exactly in the vertical projection below center of the sputtering target.

From Figure 5.1 we observe that the deposition rate is considerably higher in points close to the vertical projection below center of the sputtering target (zero position) and it falls drastically as the substrates are located further away from this projection. In these points the films thickness and deposition rate is too low because the substrate is outside the plasma, while in points close to zero position, i.e. in front or close to sputtering target, the deposition rate is higher due a higher plasma density caused by the potential distribution in the

discharge generated by an rf magnetron discharge [41]. This potential distribution determines the energies of the ions and neutral species which contribute to the deposition process.

Table 5.1 Thicknesses mean of ZnO films for different substrate positions along holder-substrate diameter ($T_s = 296 \pm 2^\circ\text{C}$, $P_w = 9.0 \times 10^{-3}$ Torr, $P_{rf} = 100$ W)

Position, x (cm)	Thickness (nm)
-4	541.2
-3	549.7
-2	557.7
-1	566.5
1	564.3
2	560.6
3	546.2
4	552.4
5	545.4
6	552.9
7	545.5
8	371.0
9	362.1
10	344.0

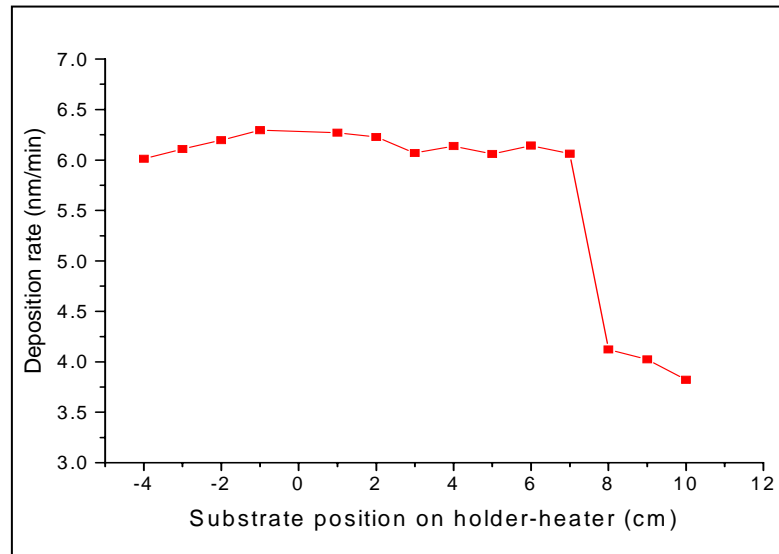


Figure 5.1 Variation of deposition rate vs substrate position on holder-heater

On the other hand, the values referred at film thickness of ZnO films on glass substrate for different rf power are shown in the Table 5.2. In this case, the substrates were located on substrate-holder in regions or points close to zero position, i.e., in places where the deposition rate approximately constant was observed. The synthesis was carried out during 30 minutes with rf power applied from 25 W to 150 W, $T_s = 198 \pm 1^\circ\text{C}$, $P_w = 8.5 \times 10^{-3}$ Torr, and in addition, in this case the vertical projection height was lower (5.5 cm).

Table 5.2 Thicknesses mean of ZnO films for rf power different ($T_s = 198 \pm 1^\circ\text{C}$, $P_w = 8.5 \times 10^{-3}$ Torr).

rf power (W)	Thickness (nm)
25	53.14
50	128.75
75	227.05
100	334.64
125	510.04
150	585.79

From this table we observe that as increases rf power the films thickness increases from 53.14 nm to 585.79 nm indicating that rf power is a influential parameter on film thickness in the synthesis of films by rf magnetron sputtering technique. We observed also that for 100 W rf power, the value of the film thickness obtained in this case (334.64 nm) is lower that the mean value of the film thickness obtained in the previous case (552.9 nm) (see Table 5.1). This difference (~218.3 nm) is due at change in the sputtering time (from 90 min to 30 min) and substrate temperature (from 296°C to 198°C) although that the height vertical projection was intentionally decreased from 7.5 cm to 5.5 cm.

The Figure 5.2 shows a plot for deposition rate vs. rf power. The deposition rate increases monotonically as rf power increases. This increase indicates that the numbers of atoms sputtered from the target is proportional to the rf power, as expected [39,41]. Therefore, under the deposition conditions mentioned above, the relationship between deposition rate (r) and rf power (P_{rf}) could be given by:

$$r = 4.35967 (P_{rf} - P_{rf,th}) \quad [\text{nm/min}] \quad \mathbf{5.1}$$

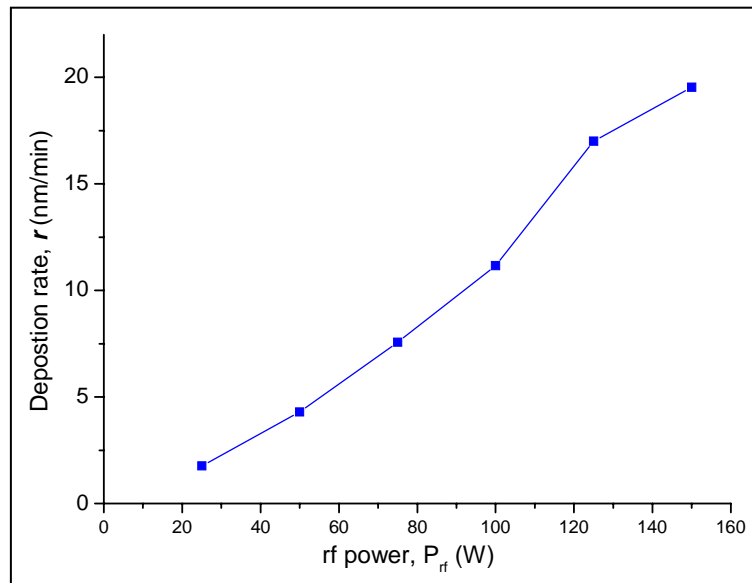


Figure 5.2 Variation of deposition rate with rf power

where $P_{rf,th}$ can be called how the *rf power threshold* due to the low discharge voltages. From plot showed in Figure 5.2, the $P_{rf,th}$ is estimated 19.7 W approximately.

Again, from comparison between the Figures 5.1 and 5.2 we observe that the deposition rate value corresponding at 100 W rf power obtained in this case (11.2 nm/min), is almost twice

greater than the deposition rate mean value obtained in the previous case (~ 6.2 nm/min). If we consider that the deposition rate is independent of the deposition time, this difference (~ 5.0 nm/min) possibly is due at the height vertical projection was lower (5.5 cm) and the pressure was lower changed slight from 9.0×10^{-3} Torr to 8.5×10^{-3} Torr. At lower pressures the mean free path of the sputtered species (Zn, for example) is increased and hence their energy too.

5.2.2 Structure of ZnO film

The structural features of the ZnO films were evaluated by X-ray diffraction. The morphology was analyzed by AFM. The crystalline quality of the films was correlated against important deposition parameters such as the substrate to target distance (substrate positions on holder) and rf power sputtering.

5.2.2.1 XRD patterns

The ZnO films growth under onto glass substrate were physically stable and had very good adhesion to the substrate. No chipping or delamination was observed, even when the films were cleaned with acetone and ethanol in each analysis. The XRD patterns shown in Figures 5.3 and 5.4 show the effects of substrate to target distance (or substrate position on holder-heater) and rf power on the crystallinity of ZnO films synthesized under conditions mentioned above. The inset in Figure 5.3 is also shown the XRD patterns obtained from ZnO

target for comparison. The peaks observed correspond at a typical wurtzite hexagonal structure ZnO with a preferred orientation the *c*-axis perpendicular to the substrate. However, greater polycrystallinity was observed for substrate to target distance close to target and for higher rf power which has a direct relation with film thickness. This result could be favorable for conductivity of the films due that drive at a degenerate or non-stoichiometric semiconductor which is agreement chemical analyses found from EDAX for ZnO films deposited at rf power 50 W (47.7% O, 52.83%Zn) and rf 100W (29.31% O, 70.69% Zn). It which means that, the possible optimum substrate position on holder is between -1 cm and +5 cm and the rf power possible optimum could be between 80 W and 125 W.

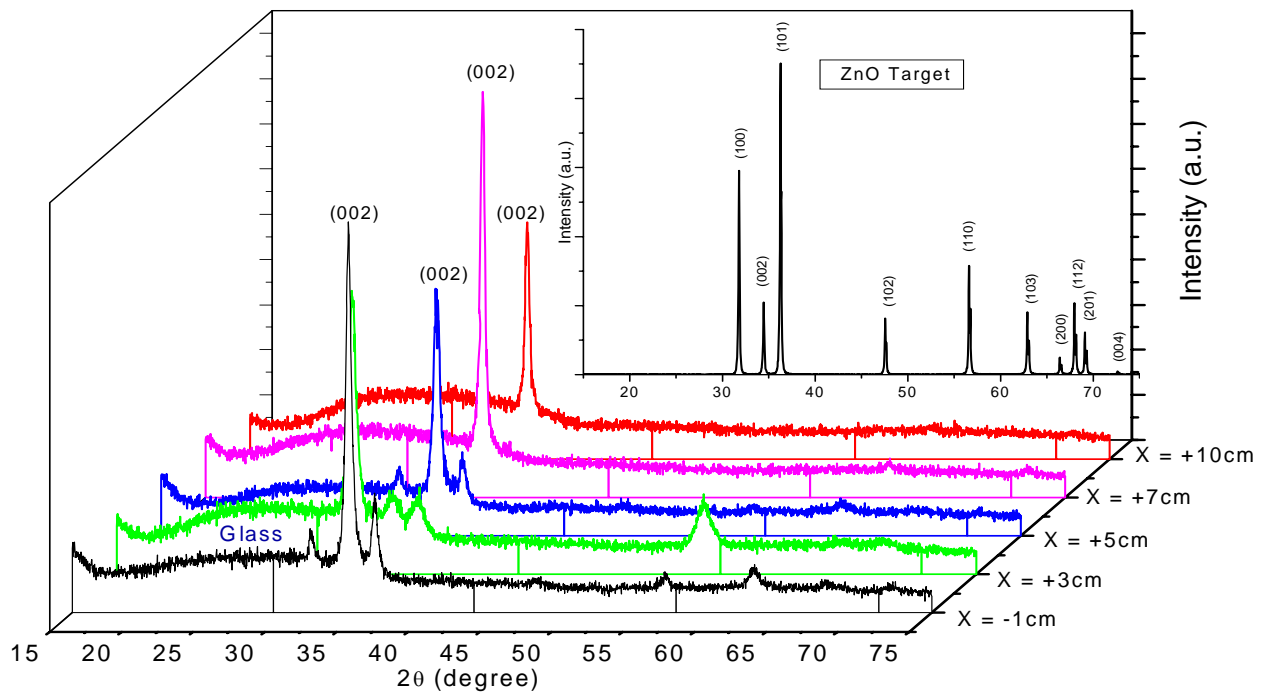


Figure 5.3 Effect of substrate to target distance on the crystallinity of ZnO films synthesized on glass. (X = substrate position on holder)

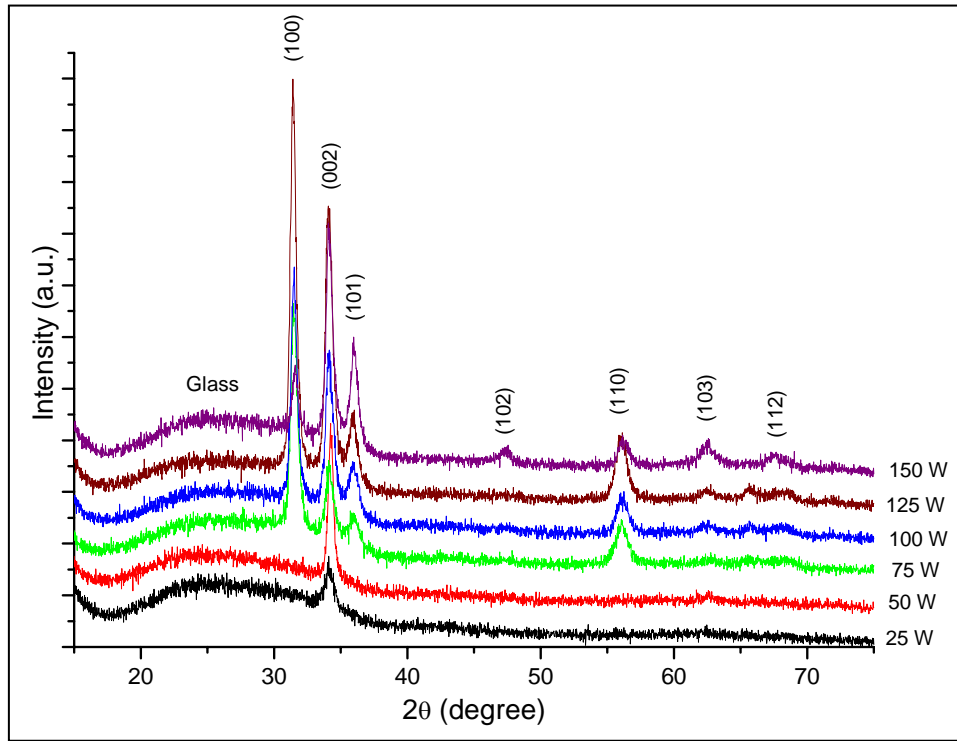


Figure 5.4 XRD patterns of the ZnO films at different rf power

Tables 5.3 and 5.4 shows the (002) peak position, interplanar distance d (002), c -axis value and film stress calculated for each film. The interplanar distance d and c -axis lattice parameters were calculated using the following equations [57]:

$$d = \frac{\lambda}{2 \sin \theta} \quad 5.2$$

with $\lambda = 0.154056$ nm.

And,

$$d_{hkl} = \frac{a}{\sqrt{h^2 + k^2 + \left(\frac{a}{c}\right)^2 l^2}} \quad 5.3$$

being, $h = k = 0$ and $l = 2$. Therefore,

$$c = 2 d_{002} \quad 5.4$$

The stress films can be calculated based on the biaxial strain model [60], using interlayer spacing of the films. The stress in the plane of ZnO film with a hexagonal crystal structure can be expressed as [61,62]:

$$\sigma_{film} = \frac{2c_{13}^2 - c_{33}(c_{11} + c_{12})}{2c_{13}} \frac{c_{film} - c_{bulk}}{c_{film}} \quad 5.5$$

The values of the elastic constant from single crystalline ZnO are used, $c_{11} = 208.8$ GPa, $c_{33} = 213.8$ GPa, $c_{12} = 119.7$ GPa and $c_{13} = 104.2$ GPa. Substituting these values in the above equation gives:

$$\sigma_{film} = -232.75 \left(\frac{c_{film} - c_{bulk}}{c_{bulk}} \right) \text{ [GPa]} \quad 5.6$$

where $c_{bulk} = 5.2067 \text{ \AA}$, which was obtained from data base of the program MATCH [58].

Table 5.3 Peak position and calculated lattice parameters at different substrate position on holder (X).

X (cm)	2 θ for (002) reflection (°)	Interplanar spacing d ,(Å)	Lattice constant c ,(Å)	Stress (GPa)
-1	34.28	2.61371	5.227424	-0.926
+3	34.26	2.61519	5.230384	-1.059
+5	34.22	2.61816	5.236315	-1.324
+7	34.32	2.61075	5.221515	-0.662
+10	34.34	2.60928	5.218565	-0.530

Table 5.4 Peak position and calculated lattice parameters at different rf power.

P _{rf} (W)	2 θ for (002) reflection (°)	Interplanar spacing d ,(Å)	Lattice constant c ,(Å)	Stress(GPa)
25	34.10	2.62710	5.25419	-2.123
50	34.22	2.61816	5.23632	-1.324
75	34.10	2.62710	5.25419	-2.123
100	34.14	2.62411	5.24822	-1.856
125	34.08	2.62859	5.257184	-2.257
150	34.08	2.62859	5.257184	-2.257

The shift of the diffraction (002) peak position from its normal value is mainly associated with residual stress in the film [63]. In this work, the compressive stresses found in all films were due to increment of the c -axis value in comparison at the c -axis of the bulk. The Figures 5.5a and 5.5b show a relation between the stress and the average grain size. The average grain size was obtained from Scherrer's formula (Equation 4.12):

$$\delta = \frac{0.9\lambda}{B \cos \theta_B}$$

Here we observe that smaller grain size was found for $x = +3$ cm and rf power between 75 W and 125 W but in both cases with greater compressive stress.

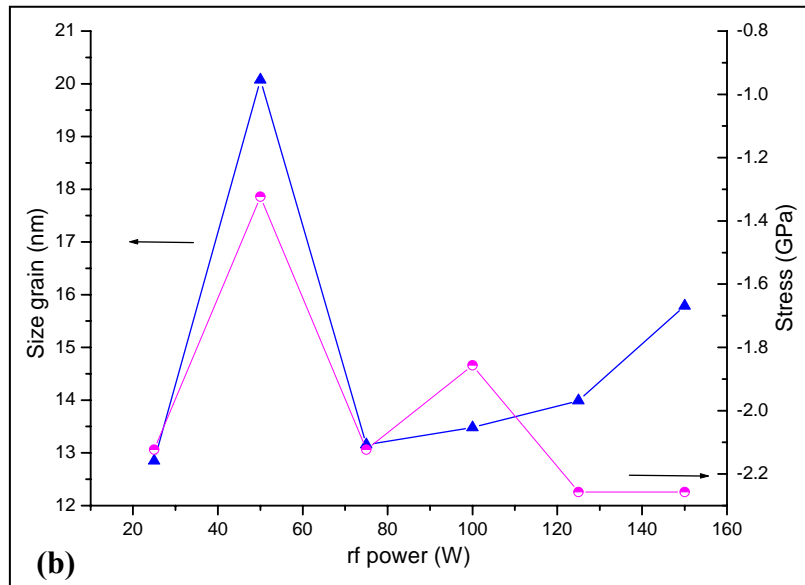
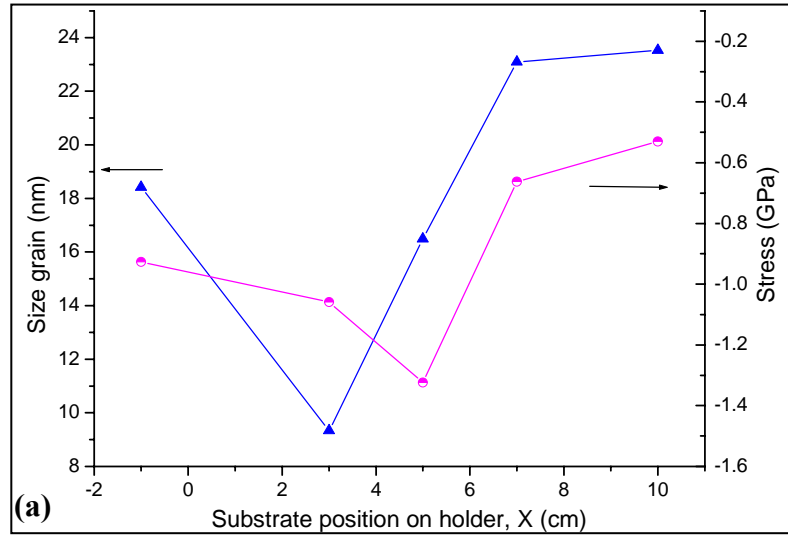


Figure 5.5 Size grain and film stress for different (a) substrate position and (b) rf power.

AFM images showed higher rms roughness for 150W rf power which is agreement with their greater compressive stress found.

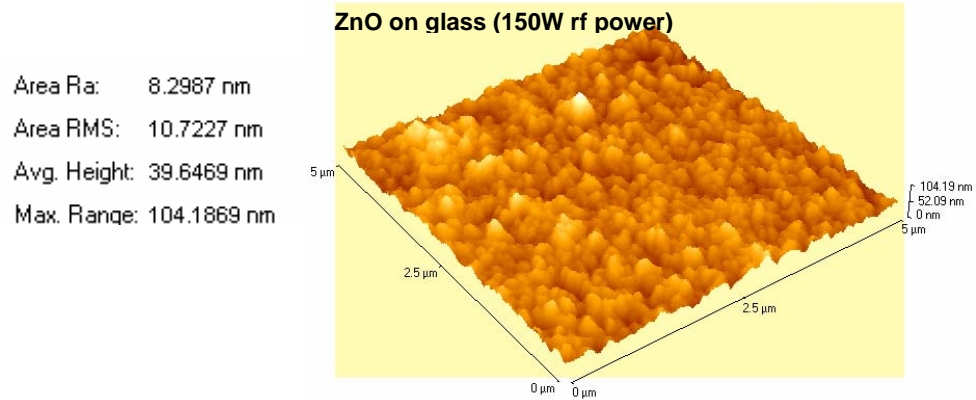


Figure 5.6 Surface morphology of ZnO films on glass at 150 W rf power. (5μm x 5μm).

5.2.3 Optical properties of ZnO films

For most applications, high transmission in the visible range is also important. Figures 5.7a and 5.7b show the transmittance of the all films deposited under different substrate position and rf power. The films at different substrate position display transparency in excess of 80% throughout the visible range while that, the films at different rf power showed above 70%. The cut-off wavelength λ_c where the transmission approaches a zero and the absorption is increased by transitions of electrons from valence band to the conduction band [64], changed towards lower wavelengths for greater substrate to target distance and low rf power. In addition, both with increasing thickness, the transmittance of the films is decreased due to the thickness effect, which leads to a decrease in light scattering losses. However, as mentioned above, an increase in the film growth rate led to non-stoichiometric films with low transmittance but, greater conductivity could be expected. The oscillatory behavior of these

spectrums is due to the interference between the incoming and reflected light. The increase in surface roughness could be responsible for this behavior also.

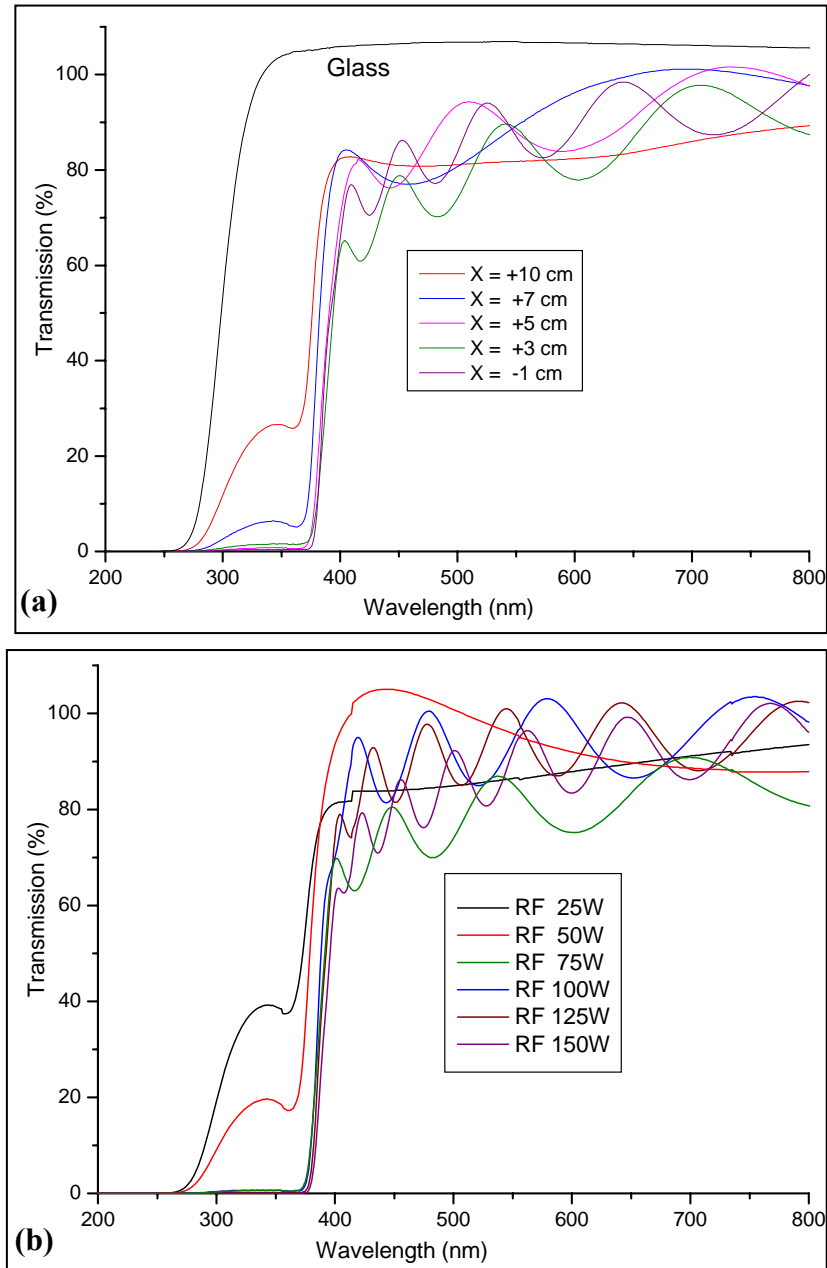


Figure 5.7 Optical transmissions of ZnO films synthesized onto glass with various (a) substrate position and (b) rf power.

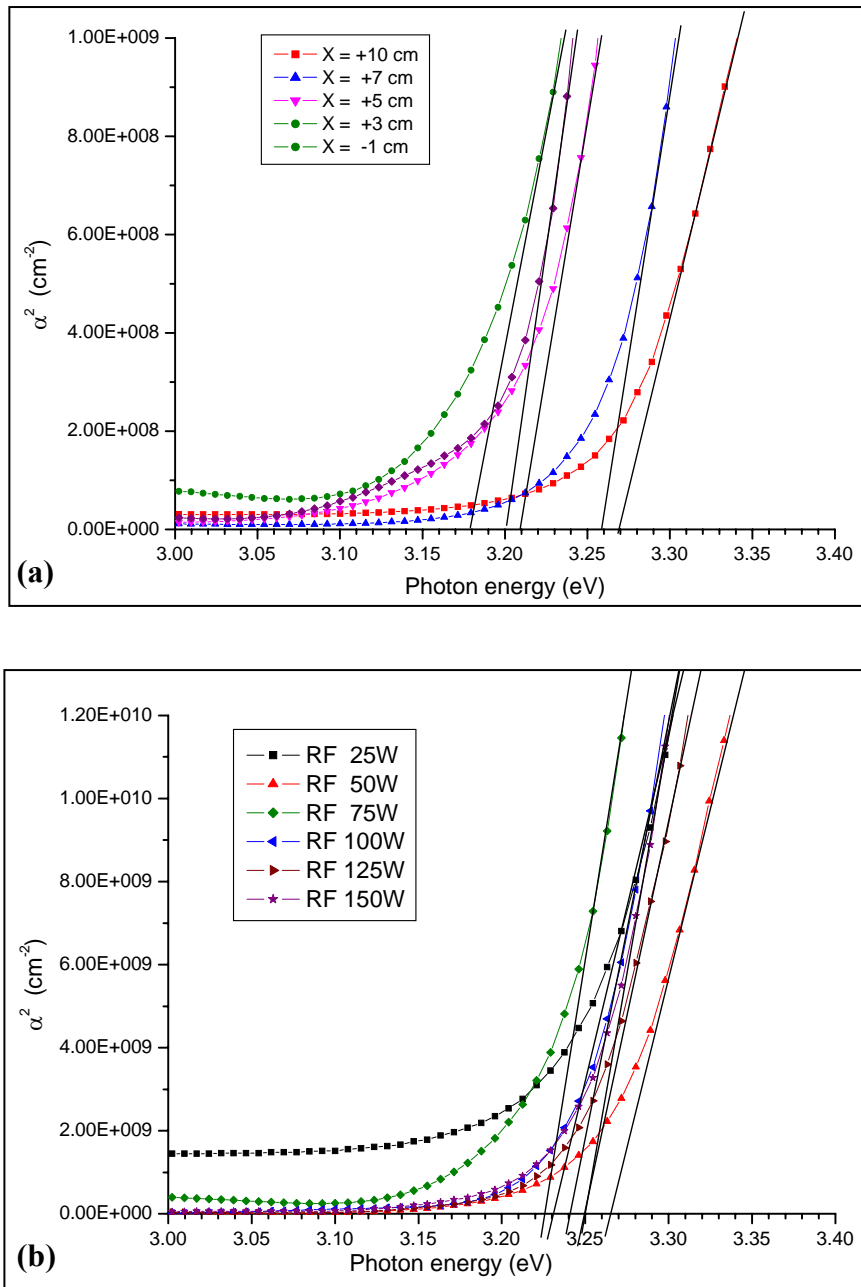


Figure 5.8 Optical band gap of ZnO films at different (a) substrate to target distance and (b) rf power

In this work it was tried to find a relation between the optical band gap with film stress from plot for optical band gap and film stress as function of the substrate position and rf power.

The variation of optical band gap (E_g) for films can thus be obtained by plotting α^2 vs. $h\nu$ (Figures 5.8a and 5.8b). α is the absorption coefficient and $h\nu$ is the photon energy, both obtained from UV transmittance data. E_g is then determined by extrapolation method. This method was explained in detail in the experimental procedure.

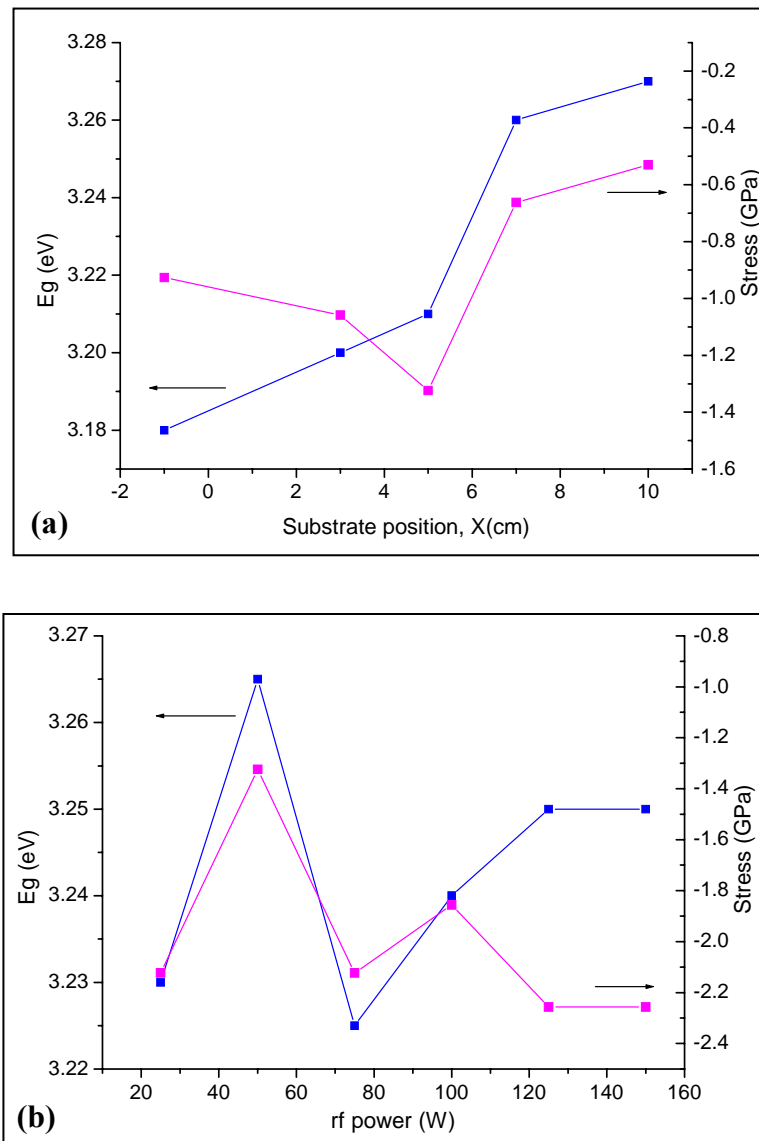


Figure 5.9 Optical band gap and film stress of ZnO films with different (a) substrate to target distance and (b) rf power

From Figure 5.9a we observe that the band gap widens with increasing substrate to target distance D_{ts} following the equation approximate: $E_g \equiv 0.00892 X + 3.18$ [eV]. The greater value found for E_g is 3.27 eV which is more close at band gap value of the ZnO bulk (3.3 eV) and correspond at smaller compressive stress. This means that of the band gap could be affected by film stress and the substrate to target distance. On the other hand, from Figure 5.9b we observe that the widened in band gap follow a similar behavior with films stress below 100W rf power, from which the behaviors are opposed.

5.3 Sputtering deposition of Al-doped ZnO film

In this section we describe the effect of aluminum on the electrical properties and optical properties of ZnO film. This study is important due us will allow evaluate the possibility of obtain better electrical, optical and magnetic properties of ZnO films doped with metal transitions. The films were deposited at $\sim 300^\circ\text{C}$ ($296 \pm 2^\circ\text{C}$). The working pressure in Ar gas was 9.0×10^{-3} Torr and the rf power was 100W. The substrate position was +5cm and the high vertical projection 7.5 cm.

Structural characterization

Figure 5.10 shows the typical XRD pattern of ZnO and Al-doped ZnO films. The (002) diffraction peaks for ZnO film and Al-doped ZnO film was observed at $2\theta = 34.20^\circ$ and $2\theta = 34.28^\circ$ respectively (see inset Figure 5.10). This shift means that the c -axis lattice parameter was decreased with Al doping. This result is reasonable because possibly Al atoms are

substituted into the Zn site in the crystal, considering that the ionic radii of Al^{3+} (53pm) is greater than ionic radii of Zn^{2+} (72 pm). The Al atomic percentage found from EDAX was 4.85%.

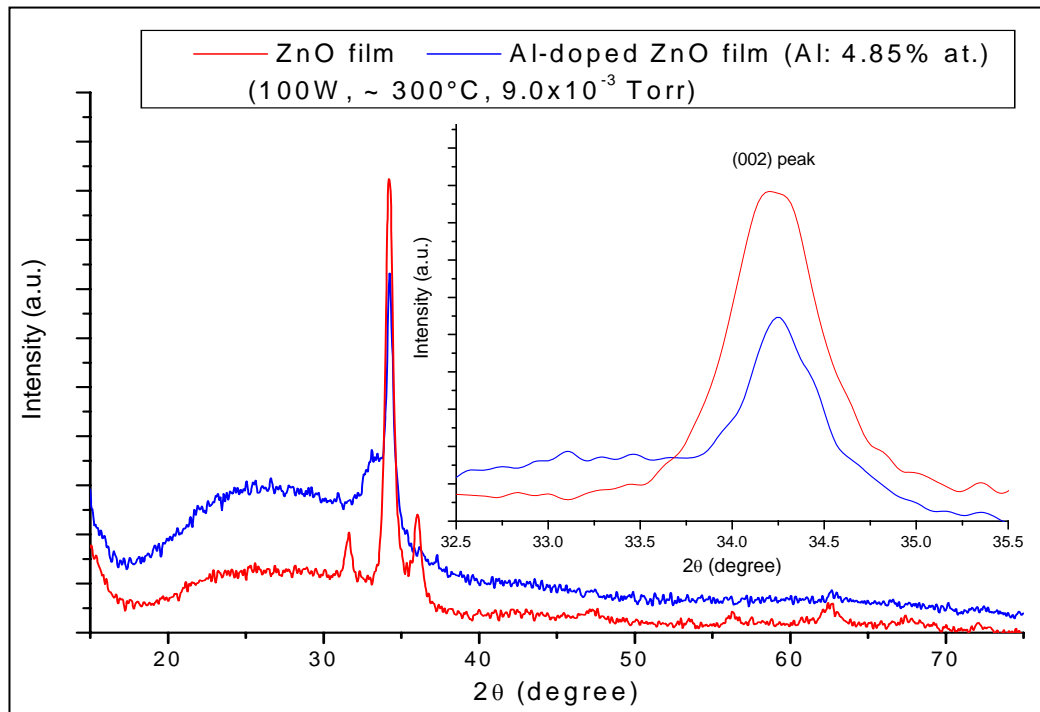


Figure 5.10 XRD pattern of ZnO and Al-doped ZnO films deposited onto glass substrate. The inset shows the shift of (002) diffraction peak

Figure 5.11 shows SEM surface micrograph of the Al-doped ZnO film with 4.8% at. obtained from EDAX. The average grain size is $\sim 0.1 \mu\text{m}$ ($\sim 100 \text{ nm}$). The grains become densely packed near regularly. The average grain size δ deduced from x-ray diffraction using

the Scherrer's formula (Eq. 4.12) is estimated at ~ 17.01 nm. Therefore, as shown in SEM surface micrograph the grain size is ~ 6 times larger than that estimated from XRD data. This means that the semiconductor Al-ZnO film is polycrystalline.

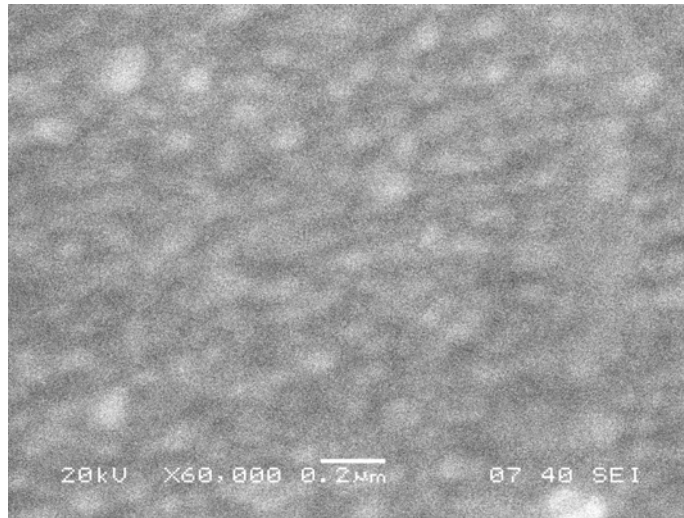


Figure 5.11 SEM surface micrograph of Al-doped ZnO film (Al 4.85%at.) synthesized onto glass at 100 W rf power, $P_w = 9.0 \times 10^{-3}$ Torr).

Optical band gap and conductivity

The effect of Al doping on optical and conductivity of ZnO film has been studied. From transmission spectra, not showed here, exhibited a transmission of higher than 80% in the visible region with a sharp fundamental absorption edge. Because Al-doped ZnO film is a direct transition-type semiconductors too, the optical band gap (E_g) can be obtained by plotting α^2 vs. $h\nu$ (α is the absorption coefficient and $h\nu$ is the photon energy). The photon

energy at the point where $\alpha^2 = 0$ is E_g . The E_g value was determined by the extrapolation method. The Figure 5.12 shows the results of the E_g values for both, ZnO and Al-doped ZnO, 3.25 eV and 3.55 eV respectively. This broadening effect due at Al effect can be understood based on the Burstein-Moss (B-M) effect [9,65], i.e. the optical band gap of ZnO increased in energy with increasing impurity concentrations.

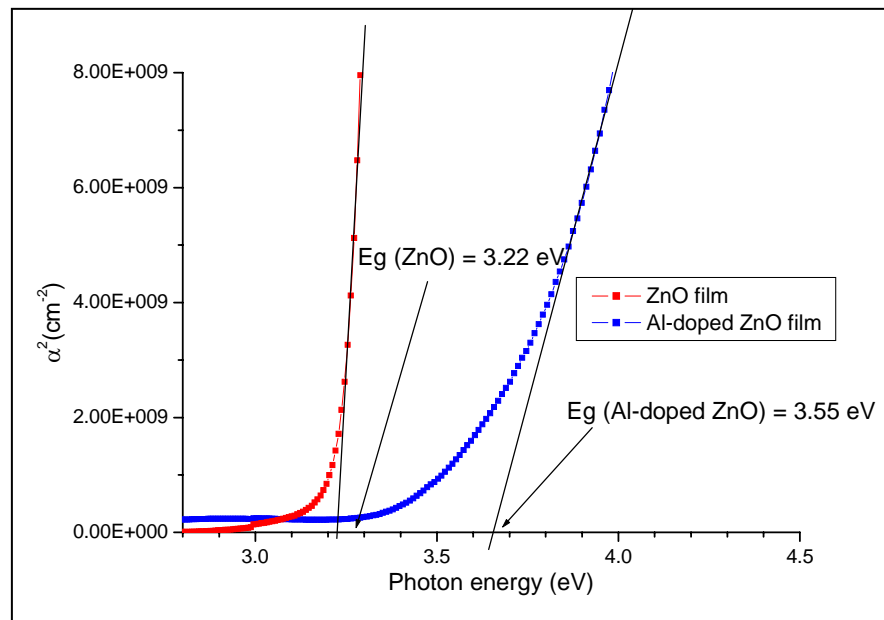


Figure 5.12 Optical band gap of ZnO and Al-doped ZnO film calculated from plot α^2 vs. $h\nu$.

This effect is illustrated in Figure 5.13 where we can observe the possible presence of electrons occupying states in the conduction band. The Fermi level in the conduction band of the degenerate semiconductor leads to the energy band widening effect.

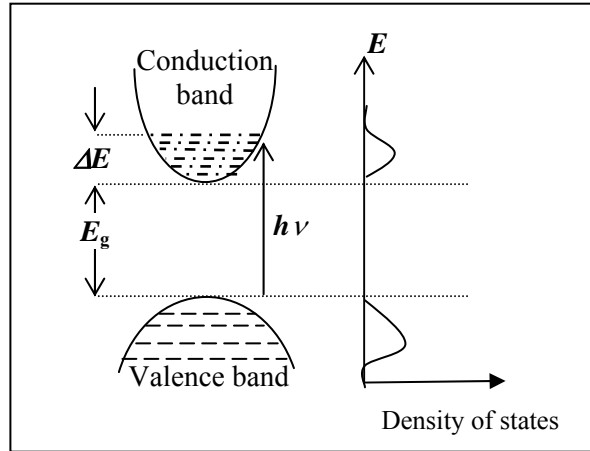


Figure 5.13 Diagram model showing the band and density of states by impurity effect (semiconductor *n*-type).

The number of conduction electrons required to fill the band to a level ΔE , shown in the Figure 5.13 is:

$$N = \int_0^{\Delta E} g(E) dE = \left(\frac{V}{2\pi^2} \right) \left(\frac{2m^*}{\hbar^2} \right)^{3/2} \int_0^{\Delta E} E^{1/2} dE \quad 5.7$$

where $g(E)$ is the density of states, $m^* = 0.24m_e$ is the electron reduced effective mass [4].

Hence,

$$\Delta E = \left(\frac{\hbar^2}{2m^*} \right) (3n\pi^2)^{2/3} \approx 0.25eV \quad 5.8$$

Where n is the carrier concentration.

On the other hand, the plot resistivity vs temperature (see Figure 5.14) showed shift to smaller temperatures for resistivity Al-doped ZnO due probably at presence of carrier concentration n_e indicating to be better conductive that undoped ZnO at temperature below 200 K.

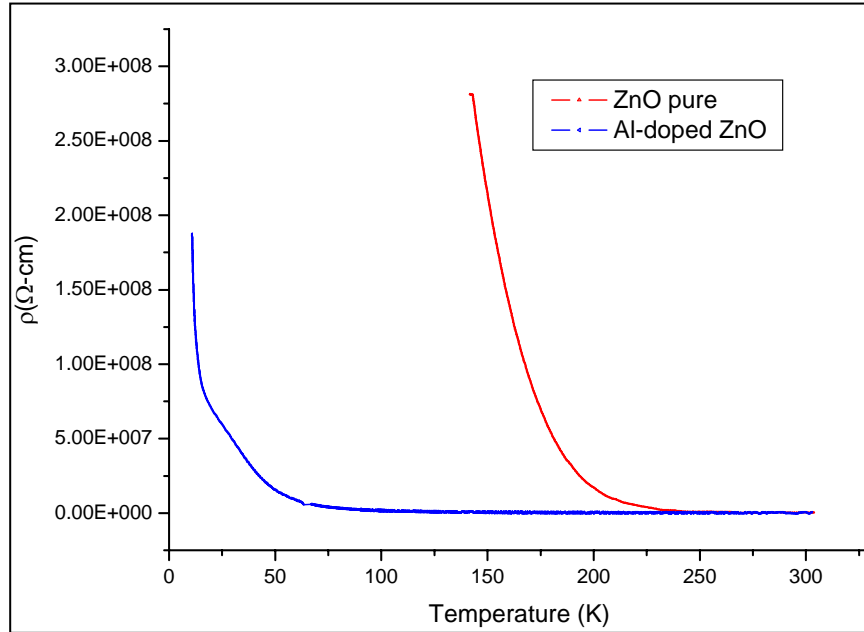


Figure 5.14 Plot resistivity vs temperature of ZnO and Al (4.85%at.)-doped ZnO films.

5.4 Substrate effect on structure of ZnO film

In order to study the substrate effect on the structure of the ZnO films, synthesis of films onto quartz substrate and glass substrate under the same sputtering conditions. From XRD pattern shown in the Figure 5.15 we can see that the quartz substrate improve the growth of the films with perpendicular c -axis to the substrate surface. This means that this substrate is more

compatible with the films of ZnO and could be expected less tensions in the films ($P_{rf} = 100\text{W}$, $T_s = 300^\circ\text{C}$ and $P_w = 9.0 \times 10^{-3}$ Torr).

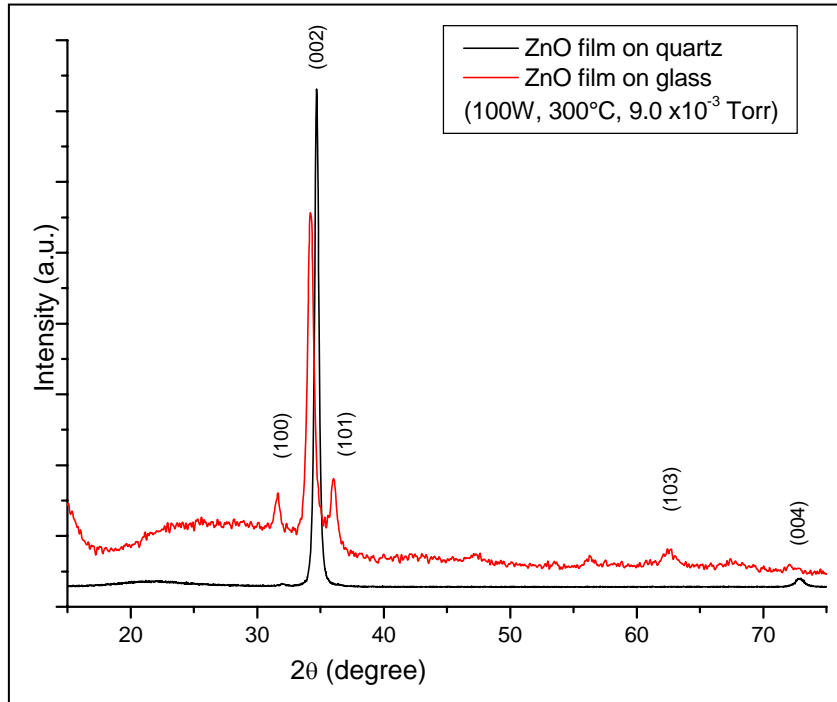


Figure 5.15 XRD patterns of ZnO films grown onto quartz and glass substrate.

5.5 Optimum deposition conditions of ZnO-based films

Based on the systematic study carried out and of the results that followed from this study, optimum deposition conditions could be determined for rf magnetron sputtering of ZnO-based films from ceramic targets. As can be observed that is preferable obtain degenerate or non-stoichiometric semiconductors in the order improve their conductivity, but also is recommendable to control the films stresses which could affect their optical and electrical properties. The results in this step shown that the films stress could be less when the rf power

is not very high, the substrate to target distance not very close and deposited with substrate temperature between 200°C-300°C. From this way could we obtain a rate deposition around 7 nm/min with a strong (002) orientation and average grain sizes around 30-40 nm. We could observe in addition that 4.68 % of aluminum content improves the conductivity in the films of ZnO without modifying its structure. The most important parameters and proposed values are summarized in Table 5.5.

Table 5.5 Optimum sputtering conditions for the deposition of ZnO-based films, as determined experimentally in this study.

Parameter	Optimum values/range
Substrate position	Between -1 cm and +5 cm
Height of vertical projection to target	7.5 cm
Substrate temperature	Between 200 and 300°C
RF power	Between 80 and 125 W
Argon working pressure	8.0×10^{-3} and 9.0×10^{-3} Torr
Al content (optional)	to 4 % at.
Substrate recommendable	Quartz

5.6 Sputtering deposition of Co-doped ZnO and Co,Fe-doped ZnO films

The ZnO films doped with Co and Fe were synthesized onto quartz from ceramics targets ($\text{Zn}_{0.90}\text{Co}_{0.10}\text{O}$ at% and $\text{Zn}_{0.85}[\text{Co}_{0.50}\text{Fe}_{0.50}]_{0.15}\text{O}$ at%) using rf magnetron sputtering in argon

gas atmosphere under the optimum conditions found in the first step of this work about of the ZnO films study. The substrate temperature (T_s), rf power (P_{rf}) and work pressure (P_w) were: $296 \pm 2^\circ\text{C}$, 125 W and 8.5×10^{-3} Torr respectively. The height of vertical projection was 7.5 cm.

5.6.1 Structure

5.6.1.1 XRD patterns

Figure 5.16a shows a typical XRD pattern for $\text{Zn}_{0.90}\text{Co}_{0.10}\text{O}$ film deposited onto quartz substrate. The inset in Figure corresponds to XRD pattern obtained from ZnO film under same sputtering parameters. Only single ZnO wurtzite phase with (002) preferential orientation is revealed. No metallic cobalt or cobalt oxide phases are observed, suggesting that the Co atoms are substituted in the ZnO lattice. From the XRD pattern of $\text{Zn}_{0.85}[\text{Co}_{0.50}\text{Fe}_{0.50}]_{0.15}\text{O}$ film shown in the Figure 5.16b, only four diffractions peaks of the hexagonal wurtzite structure were observed without any impurity peaks from CoFe metal particles. The sharp and intense (002) peaks observed for both $\text{Zn}_{0.90}\text{Co}_{0.10}\text{O}$ and $\text{Zn}_{0.85}[\text{Co}_{0.50}\text{Fe}_{0.50}]_{0.15}\text{O}$ films indicate that the films are highly crystalline which is confirmed by the low value of full width at half maximum (FWHM). However, in both cases the position of the (002) peak was shifted towards lower 2θ values in comparison with the same peak for bare-ZnO, implicating an increase in the interplanar spacing, d . The Figure 5.17 emphasizes these changes for d calculated from XRD patterns.

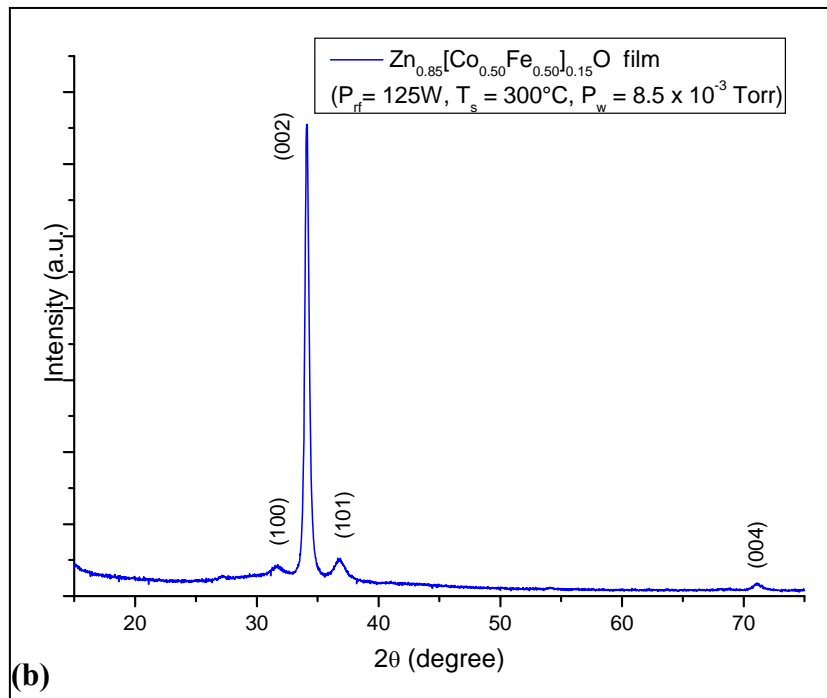
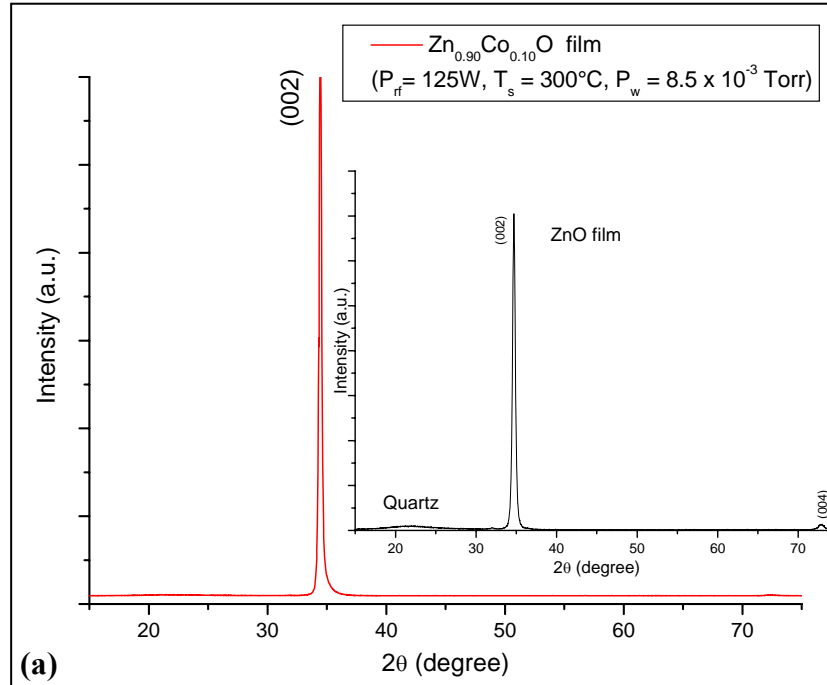


Figure 5.16 X-ray diffraction pattern of (a) $\text{Zn}_{0.90}\text{Co}_{0.10}\text{O}$ and (b) $\text{Zn}_{0.85}[\text{Co}_{0.50}\text{Fe}_{0.50}]_{0.15}\text{O}$ films. Inset: X-ray diffraction of ZnO film.

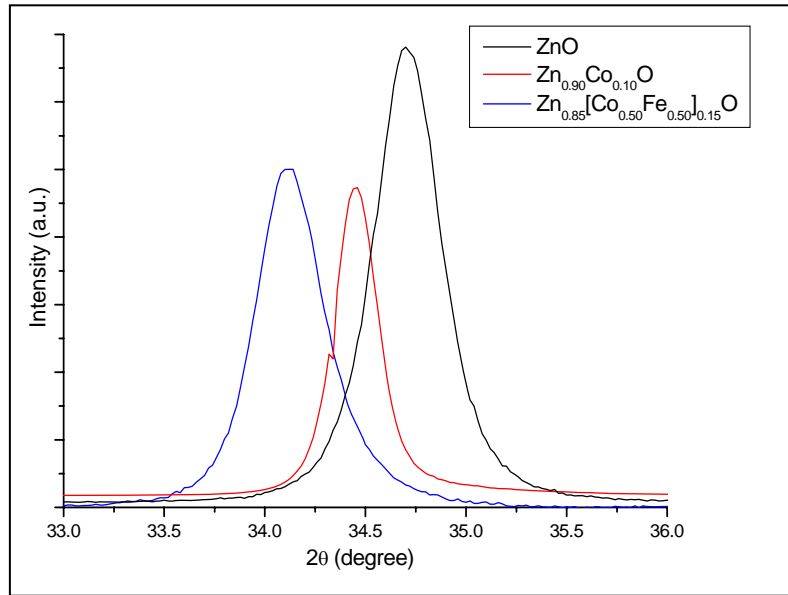


Figure 5.17 (002) peak of ZnO, Zn_{0.90}Co_{0.10}O and Zn_{0.85}[Co_{0.50}Fe_{0.50}]_{0.15}O films

Table 5.6 shows the peak position, interplanar spacing d , c -axis value and stress σ , calculated for the films. The stress values in the films were calculated considering the biaxial strain model using the equation 5.5:

$$\sigma_{film} = -232.75 \left(\frac{c_{film} - c_{bulk}}{c_{bulk}} \right)$$

with $c_{bulk} = 5.2067 \text{ \AA}$. Here we observed that the increase in the dopant concentrations, 'x', increased the c -axis value compared to undoped ZnO thin films.

Table 5.6 Calculated lattice parameters and stress for ZnO, Co-doped ZnO and Co,Fe-doped ZnO films

Film	2 θ for (002) reflection ($^{\circ}$)	Interplanar spacing d ,(\AA)	Lattice constant c ,(\AA)	Stress(GPa)
ZnO	34.70	2.58303	5.16606	1.813
Zn _{0.90} Co _{0.10} O	34.46	2.60047	5.20094	0.253
Zn _{0.85} [Co _{0.50} Fe _{0.50}] _{0.15} O	34.14	2.62411	5.24821	-1.860

The dopant content dependence of the $d(002)$ value (associated to the c -axis lattice constant value) is shown in Figure 5.18. The $d(002)$ values increased monotonically with increasing the dopant fraction in the films, 'x'. The increase in d values with a rising 'x' value can be attributed to the actual incorporation of dopant ion into the host ZnO structure [66,67].

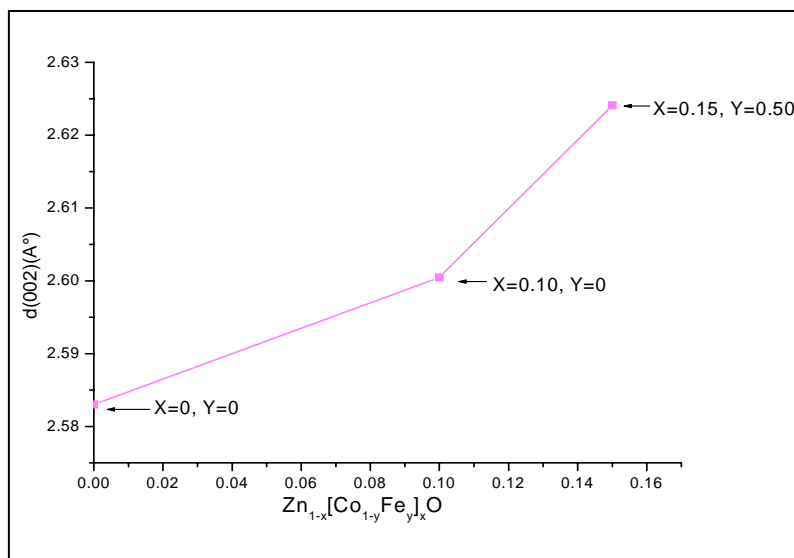


Figure 5.18 Variation of $d(002)$ value with the dopant fraction in the films, 'x'.

On the other hand, we observed that the stress in the films changed from tensile to compressive along the interface by increasing doping. Generally, all of the films deposited by sputtering are in state of stress due to the ionic bombarding during film deformation. However, lower stress was observed for $\text{Zn}_{0.90}\text{Co}_{0.10}\text{O}$ film, i.e. a σ value near zero. Then, for this film the c -axis value found (5.20094 Å) is slightly smaller than c -axis value for bulk ZnO (5.2067 Å). In addition, Co ions could exist in either Co^{2+} or Co^{3+} states in ZnO [68]. Therefore, this implicate that only Co^{2+} states are present in ZnO because their radio (72 pm) is higher than Co^{3+} diameter, but slightly lower than Zn^{2+} (74 pm) which cause a lower shrink of the lattice without changing the ZnO wurtzite structure. This result is agreement with XRD pattern corresponding to the Co-doped ZnO film (Figure 5.16a). On the other hand, the incorporation of Fe atoms into the lattice caused stress compressive due at increment of the c -axis. This increment for c -axis is due possibly by the presence of Fe^{3+} in interstitials considering that their ionic radio (55pm) is smaller than Co^{2+} and Zn^{2+} ionic radius originating a distortion of the lattice.

The relation between stress and average crystallite size it shows in the Figure 5.19. The average crystallite size was obtained from Scherrer's formula [57]. Also, the results shown in Figure 5.19 suggest that a minimum internal stress, and hence a more stable condition, was obtained in $\text{Zn}_{0.90}\text{Co}_{0.10}\text{O}$ film.

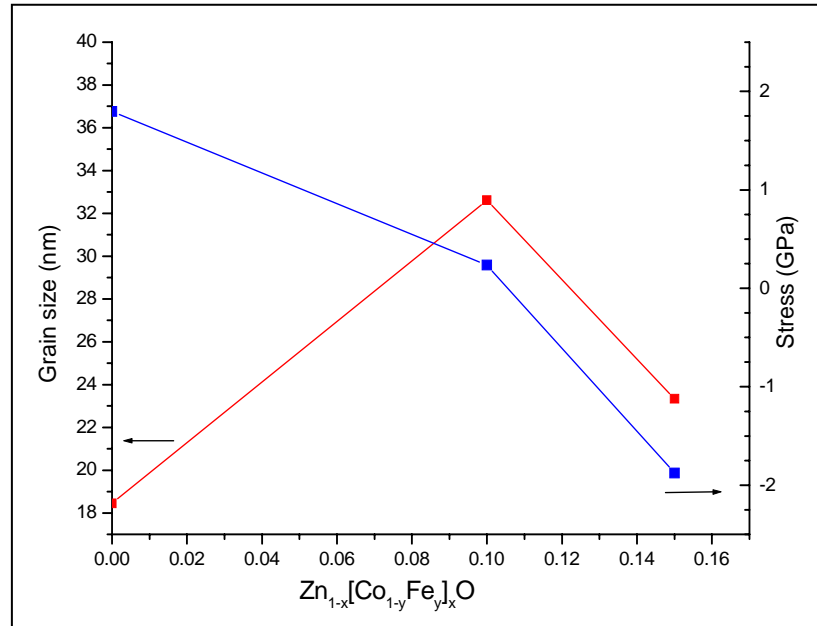


Figure 5.19 Average grain size and stress of the ZnO and Co,Fe-doped ZnO films.

5.6.1.2 Raman spectra of ZnO and Co,Fe-doped ZnO films

If photons of visible light (usually from high intensity laser beam) are scattered with the emission or absorption of phonons, the energy (or frequency) shifts are still very small, but they can be measured, generally by interferometric techniques. Therefore one can isolate the one-phonon contribution to the light scattering, and extract the values of $\omega_s(\mathbf{k})$ for the phonons participating in the process [59]. Because, however, the photon wave vectors (of order 10^5 cm^{-1}) are small compared with the Brillouin zone dimensions (of order 10^8 cm^{-1}),

information is provided only about phonons in the immediate neighborhood of $\mathbf{k} = 0$. The process is referred to as *Brillouin scattering*, when the phonon emitted or absorbed is acoustic, and *Raman scattering*, when the phonon is optical [9,59].

Raman scattering measurements were carried out using ISA T64000 from Jovin-Yvon, France. A 514.5 nm line of an Inova argon ion laser was used as an excitation source. Zinc oxide (ZnO) is a polar crystal with wurtzite $C_{6v}^4 (P6_3mc)$ symmetry and group theory predicts the existence of the following optical modes at the Γ point of the Brillouin Zone: $\Gamma_{\text{opt}} = A_1 + 2B_1 + E_1 + 2E_2$ [69,70]. The $A_1 + E_1$ modes are both infrared active and Raman active and therefore these can have longitudinal and transverse frequencies (LO and TO). Figure 5.20 shows the room temperature Raman spectra of ZnO, $\text{Zn}_{0.90}\text{Co}_{0.10}\text{O}$ and $\text{Zn}_{0.85}[\text{Co}_{0.50}\text{Fe}_{0.50}]_{0.15}\text{O}$ films. Undoped ZnO film spectrum (the bottom curve, Figures 5.20a and 5.20b) shows 2 E_2 modes at 101 and 437 cm^{-1} . While these 2 E_2 modes for $\text{Zn}_{0.90}\text{Co}_{0.10}\text{O}$ and $\text{Zn}_{0.85}[\text{Co}_{0.50}\text{Fe}_{0.50}]_{0.15}\text{O}$ films had a slight shift towards greater frequencies with broadening peak. However, this shift is still not clear enough due to the poor resolution of Raman measurement. The apparent peak shift as well as the broadening with increasing x value in $\text{Zn}_{1-x}[\text{Co}_{1-y}\text{Fe}_y]_x\text{O}$ show in Figure 5.20b means changes in the lattice, which would indicate that the Co and Fe ions could be incorporated in ZnO. The substitution of Zn by Co and Fe lowered the reduced mass, reason by which the modes frequency shifted to the higher value. This result is agreement with XRD patterns. An additional mode appears at 273.6 cm^{-1} for $\text{Zn}_{0.85}[\text{Co}_{0.50}\text{Fe}_{0.50}]_{0.15}\text{O}$ films that is no well understood.

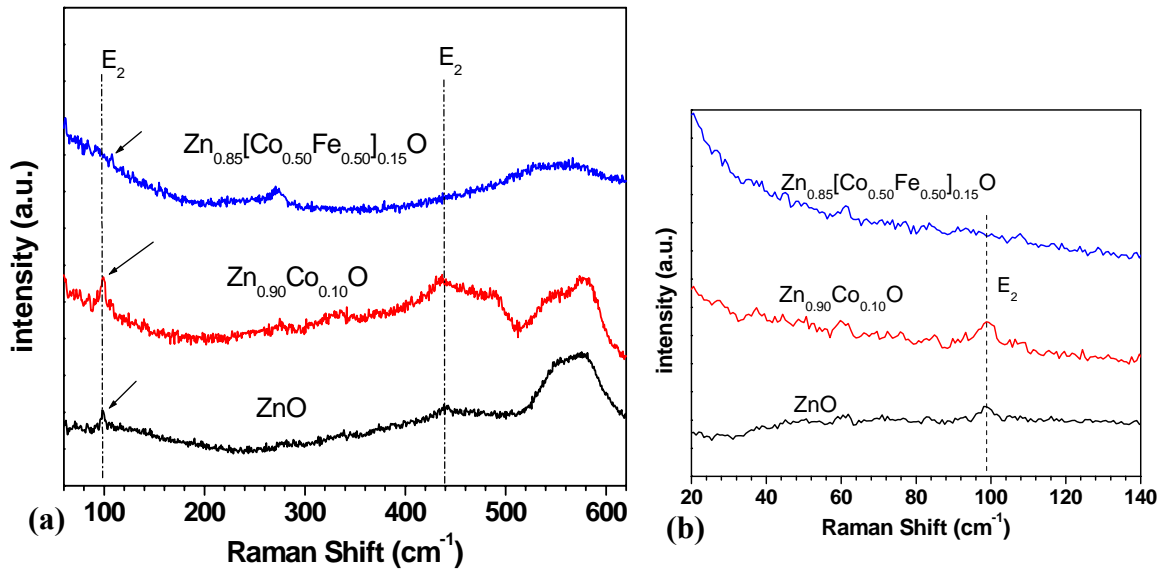
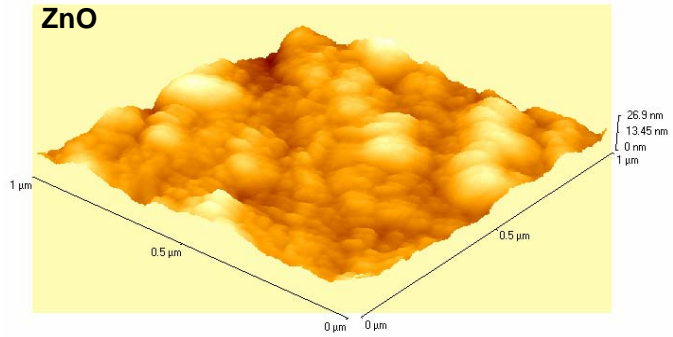


Figure 5.20 (a) Room temperature Raman spectra of ZnO, Zn_{0.90}Co_{0.10}O and Zn_{0.85}[Co_{0.50}Fe_{0.50}]_{0.15}O films, (b) Variation of strongest E₂ mode frequency with Co and Fe content in ZnO film.

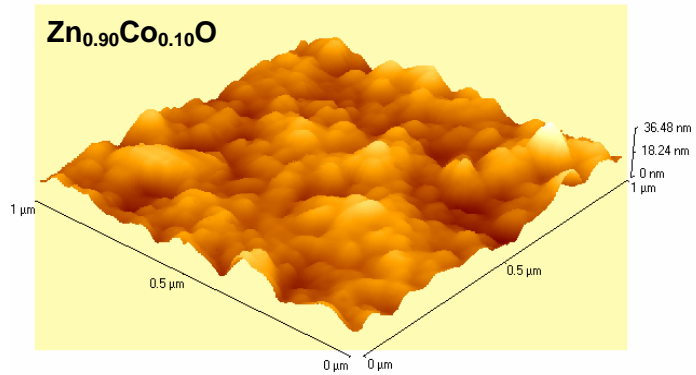
5.6.1.3 Surface morphology

From AFM images we found that the presence of Co and Fe atoms in the ZnO lattice increases the rms roughness in the films (Figure 5.21). The higher rms roughness was found for Zn_{0.85}[Co_{0.50}Fe_{0.50}]_{0.15}O film which have compressive stress and lower rms roughness for ZnO film which have tensile stress.

Area Ra: 2.8153 nm
Area RMS: 3.6373 nm
Avg. Height: 13.6015 nm
Max. Range: 26.9032 nm



Area Ra: 3.6888 nm
Area RMS: 4.7157 nm
Avg. Height: 13.3492 nm
Max. Range: 36.4755 nm



Area Ra: 4.7693 nm
Area RMS: 5.8825 nm
Avg. Height: 15.2087 nm
Max. Range: 37.9869 nm

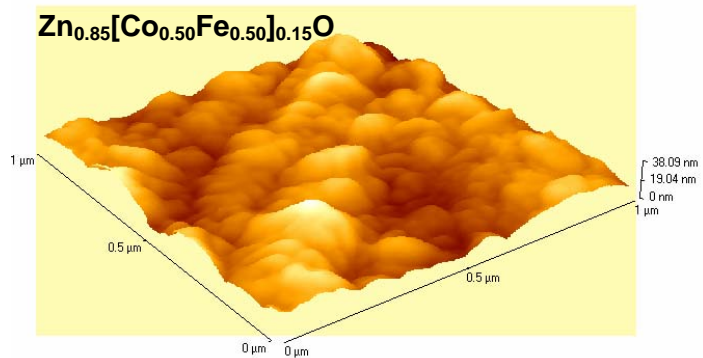


Figure 5.21 Surface morphology of (a) ZnO, (b) Zn_{0.90}Co_{0.10}O and (c) Zn_{0.85}[Co_{0.50}Fe_{0.50}]_{0.15}O films. (1 μm x 1 μm).

Figure 5.22 shows a typical SEM image of the $\text{Zn}_{0.85}[\text{Co}_{0.50}\text{Fe}_{0.50}]_{0.15}\text{O}$ film deposited on quartz. The surface is very smooth and the crystallites are very fine. No big particles can be found from SEM image. The grain size is $\sim 0.25 \mu\text{m}$ ($\sim 250 \text{ nm}$). The grains become densely packed near regularly. The average grain size δ deduced from x-ray diffraction using the Scherrer's formula (Eq. 5.13) is estimated at $\sim 23 \text{ nm}$. Therefore, as shown in SEM surface micrograph the grain size is ~ 10 times larger than that estimated from XRD data. This means that this film is polycrystalline.

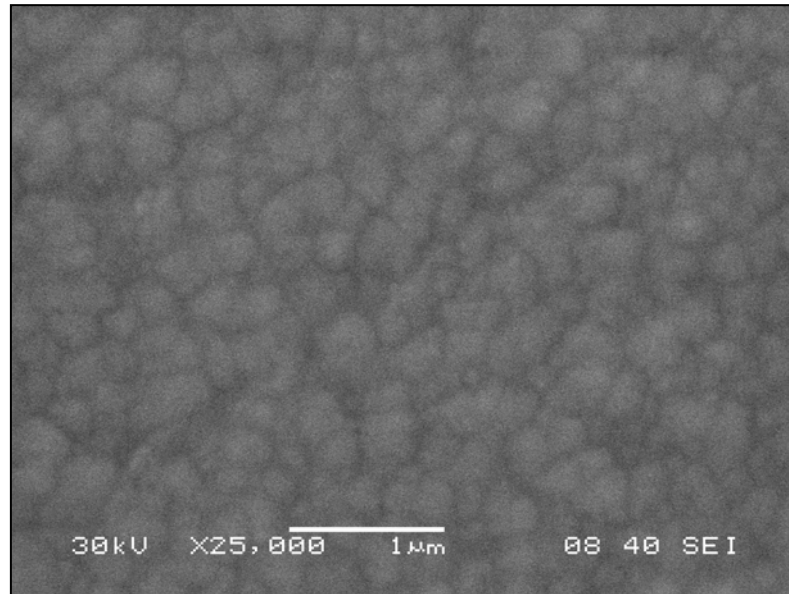


Figure 5.22 SEM image of the $\text{Zn}_{0.85}[\text{Co}_{0.50}\text{Fe}_{0.50}]_{0.15}\text{O}$ film deposited on quartz at 300°C at argon pressure 8.5×10^{-3} Torr and 125 W rf power.

5.6.2 Optical properties of Co,Fe-doped ZnO films

The effect of Co,Fe doping on the optical absorption of ZnO can be observed in the Figure 5.23. As shown in this figure, the $Zn_{0.90}Co_{0.10}O$ and $Zn_{0.85}[Co_{0.50}Fe_{0.50}]_{0.15}O$ films exhibited significant bands tails the near-band-edge region (or cut-off wavelength λ_c). These bands tails seem to be related to dopant fraction in the films, 'x', point defects, Zn vacancies, interstitial Co^{3+} , phonon-assisted transitions or stress as we will see later from relation between band gap and stress. Undoped ZnO film showed a good transmittance above 80% in the visible range from 400 – 800 nm. $Zn_{0.90}Co_{0.10}O$ film showed transmittance above 70%, but with three absorption peaks in 568 nm (2.18 eV), 610 nm (2.03 eV) and 653 nm (1.89 eV) which are indicated by arrows **a**, **b** y **c** in the Figure 5.23. These absorption peaks are attributed to $d-d$ transitions of tetrahedrally coordinated Co^{2+} . They are assigned as ${}^4A_2(F) \rightarrow {}^2E(G)$, ${}^4A_2(F) \rightarrow {}^4T_1(P)$ and ${}^4A_2(F) \rightarrow {}^2A_1(G)$ transitions in high spin state $C^{2+}(d^7)$, respectively [68,71]. These results are similar at the found by S. G. Yang *et. al* [72]. Therefore, from XRD and UV-Vis results suggest that the Co ions substituted for the Zn as $2+$ ions without changing the wurtzite structure.

On the other hand, the $Zn_{0.85}[Co_{0.50}Fe_{0.50}]_{0.15}O$ film showed less transmittance than the previous ones from 400 – 700 nm, then above this value it has greater transmittance. Absorption peaks were observed too for this film in 560 nm (2.21 eV), 605 nm (2.05 eV) and 650 nm (1.91 eV) indicated by arrows **d**, **e** y **f** in the Figure 5.23. These absorption peaks are very near to found above y also are attributed to $d-d$ transitions Co^{2+} and Fe^{2+} .

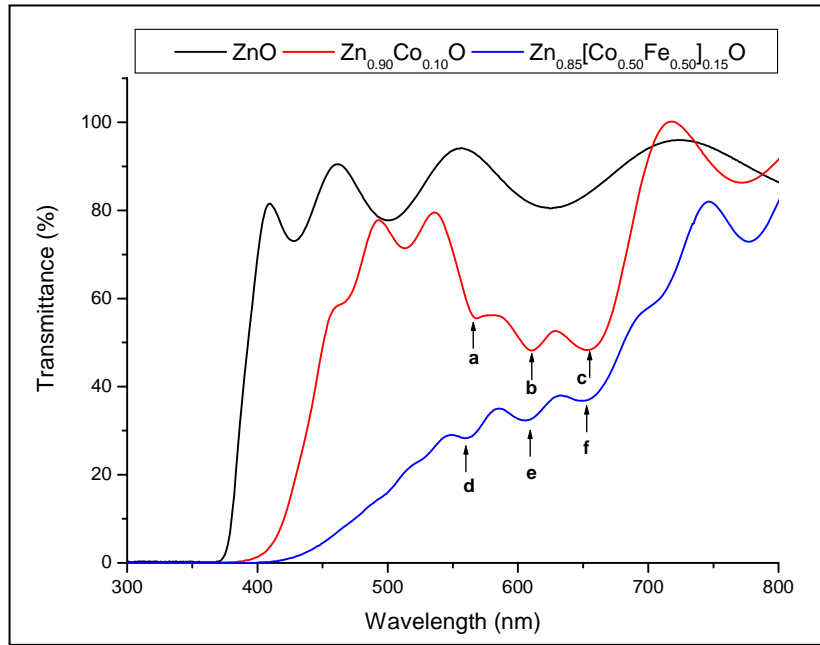


Figure 5.23 Optical transmittance spectra for ZnO, Zn_{0.90}Co_{0.10}O and Zn_{0.85}[Co_{0.50}Fe_{0.50}]_{0.15}O films.

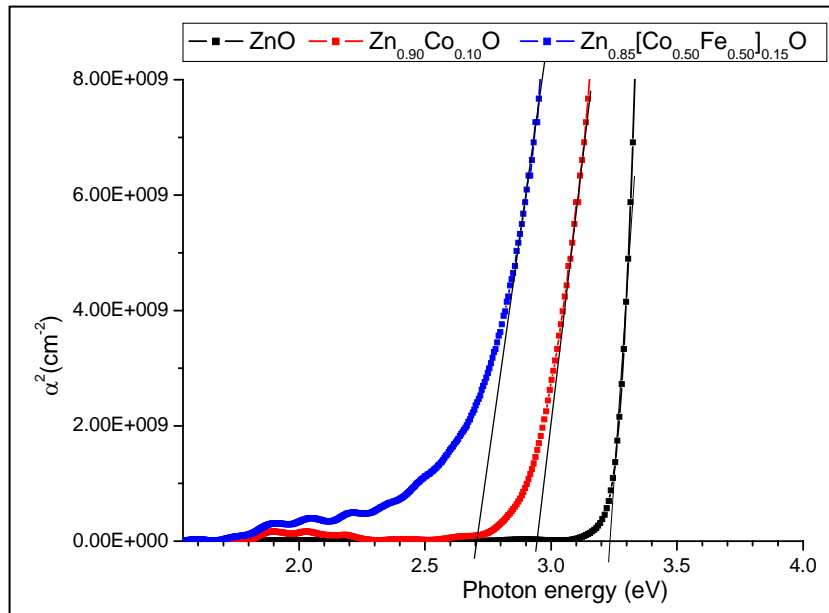


Figure 5.24 Optical band gap of ZnO, Zn_{0.90}Co_{0.10}O and Zn_{0.85}[Co_{0.50}Fe_{0.50}]_{0.15}O films calculated from plot α^2 vs. $h\nu$.

The optical band gap of $Zn_{0.90}Co_{0.10}O$ and $Zn_{0.85}[Co_{0.50}Fe_{0.50}]_{0.15}O$ films were calculated using plot band α^2 vs. $h\nu$ (Figure 5.24) as indicated in experimental procedure. The value of α was calculated using the transmission data. The estimated band gap values from extrapolation of the linear portion of α^2 to zero were: 3.23 eV, 2.95 eV and 2.7 eV for ZnO, $Zn_{0.90}Co_{0.10}O$ and $Zn_{0.85}[Co_{0.50}Fe_{0.50}]_{0.15}O$ films respectively. A decrease in the band gap energy with the dopant fraction 'x' is shown in this case, which was also reported by K.J Kim *et al* and K. Samanta *et al* [73,74]. The red shift is interpreted as mainly due to the $sp - d$ exchange interactions between the band electrons and the localized d electrons of the Co^{2+} ions substituting Zn ions. The $s-d$ and $p-d$ exchange interactions give rise to a negative and positive correction to the conduction- and the valence-band edges, respectively. In addition, the shift to lower energy due increasing the dopant fraction in the films, 'x' seem to be related to presence of localized donor levels (E_e) in the band gap which are characteristics in extrinsic semiconductors o non-stiochiometric. The absorption coefficient $\alpha(\nu)$ in the low energy rang follows the well knows exponential law, i.e. the Urbach law tail which it is expressed by [75]:

$$\alpha(\nu) = \alpha_{\eta} \exp(\hbar \nu / E_e) \quad \mathbf{5.9}$$

where E_e is interpreted as the width of the localized states in the band gap. E_e is estimated from the inverse slope of the linear plot between $\ln(\alpha)$ vs. hc/λ . Table 5.7 shows the values of the optical band gap (E_g), width of the localized state (E_e) and thickness of ZnO and Co,Fe-doped ZnO films.

Table 5.7 Optical band gap (E_g) and localized state (E_e) measurements of ZnO and Co,Fe-doped ZnO films at room temperature

Film	E_g (eV)	E_e (eV)	Thickness (nm)
ZnO	3.23	0.088	334.64
Zn _{0.90} Co _{0.10} O	2.95	0.19	566.3
Zn _{0.85} [Co _{0.50} Fe _{0.50}] _{0.15} O	2.70	0.542	566.5

As shown in the table 5.7, there is significant change in the E_e with presence of Co and Co,Fe doping in the ZnO. This greater values of E_e obtained in this present study indicates comparatively higher number of localized donor levels in the band gap. Oppositely, the value of E_e obtained for undoped ZnO is reported to be in the range of 0.07 – 0.10 eV [76], hence, the smaller values of E_e obtained in this present study indicates less number of localized donor levels in the band gap.

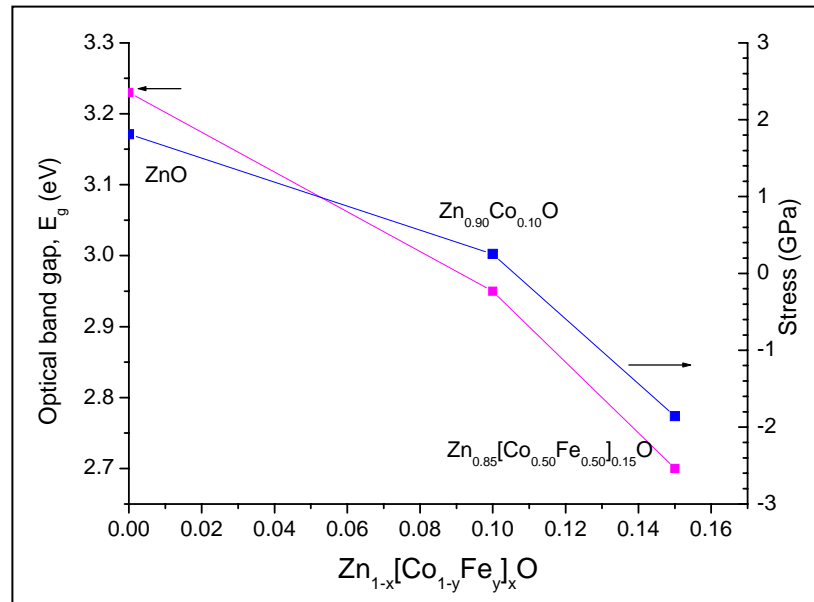


Figure 5.25 Variation of optical band gap with the dopant fraction ‘x’ in ZnO structure and stress type.

On the other hand, we can observe in the Figure 5.25 that the band gap have direct relation with film stress. The optical band gap decrease as film compressive stress as increases. This result seem related with the Co^{3+} and Fe^{3+} ions that are possibly located in interstitial sites causing distortions in the lattice, affecting the transport of the carriers.

In addition, on the Figure 5.26 we noticed that at 5 K, the band gap was widened up to ~ 3.41 eV. This result was estimated from Faraday effect at 5 K on the same film prepared in this work under the same sputtering conditions ⁽¹⁾.

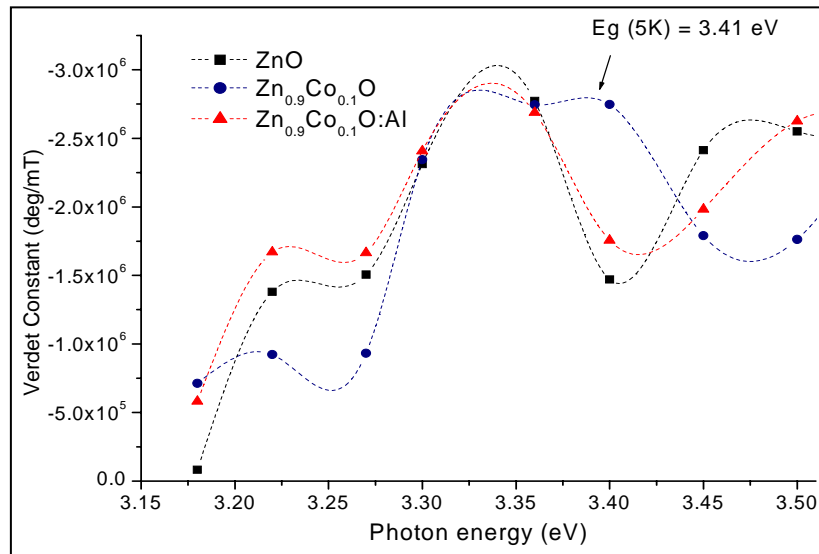


Figure 5.26 Verdet constant of ZnO , $\text{Zn}_{0.9}\text{Co}_{0.1}\text{O}$ and $\text{Zn}_{0.9}\text{Co}_{0.1}\text{O}:\text{Al}$ (6.68%at.) films ⁽¹⁾.

¹ R. Martínez, Thesis: Estudio de magnetoresistencia y rotación de Faraday en $\text{Zn}_{1-x}(\text{Co})_x\text{O}$. Lab. Magneto-optica-Dpt. Of Physic – University of Puerto Rico-Mayaguez campus.

5.6.3 Resistivity vs temperature of $\text{Zn}_{0.85}[\text{Co}_{0.50}\text{Fe}_{0.50}]_{0.15}\text{O}$ film

In this work, the variation of the resistivity with the temperature above room temperature only was measured on $\text{Zn}_{0.85}[\text{Co}_{0.50}\text{Fe}_{0.50}]_{0.15}\text{O}$ film due to the fact that the $\text{Zn}_{0.90}\text{Co}_{0.10}\text{O}$ film was very resistive and not-stable when the electric field was applied. However, we will see later that, their conductivity increased when this film was doped with Al (6.68% at.). From Figure 5.27 we can observe that the resistivity of the $\text{Zn}_{0.85}[\text{Co}_{0.50}\text{Fe}_{0.50}]_{0.15}\text{O}$ decreases as temperature increases, therefore, this film has a typical degenerate-semiconductor behavior when it is applied an electric field above room temperature. This behavior could be favorable for applications in most electronics devices. The measurements were carried out by the van der Pauw method.

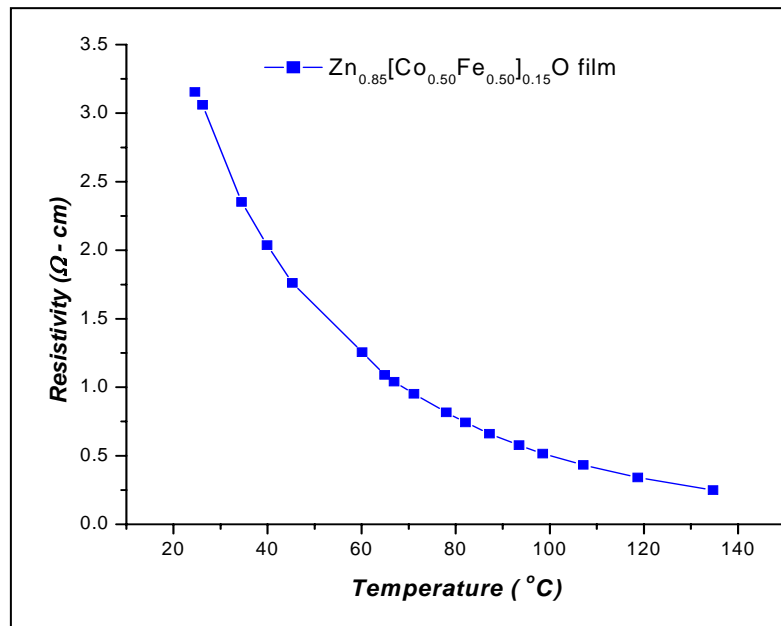


Figure 5.27 Variation of resistivity with the temperature of $\text{Zn}_{0.85}[\text{Co}_{0.50}\text{Fe}_{0.50}]_{0.15}\text{O}$ film.

In the Figure 5.28 we observe the aluminum content (6.68%at.) effect on conductivity in $Zn_{0.90}Co_{0.10}O$ film. The resistivity displays a typical semiconducting behavior. At room temperature the resistivity has a value of $25.1 \Omega\text{-cm}$. In addition, from plot resistivity vs temperature (below room temperature) showed shift to smaller temperatures for resistivity due probably at presence of carrier concentration n_e indicating to be better conductive that undoped ZnO and Al-doped ZnO film at temperature below 50 K. The inset in the Figure shows a plot resistivity vs temperature for undoped ZnO, Al-doped ZnO and $Zn_{0.85}[Co_{0.50}Fe_{0.50}]_{0.15}O$ for comparison.

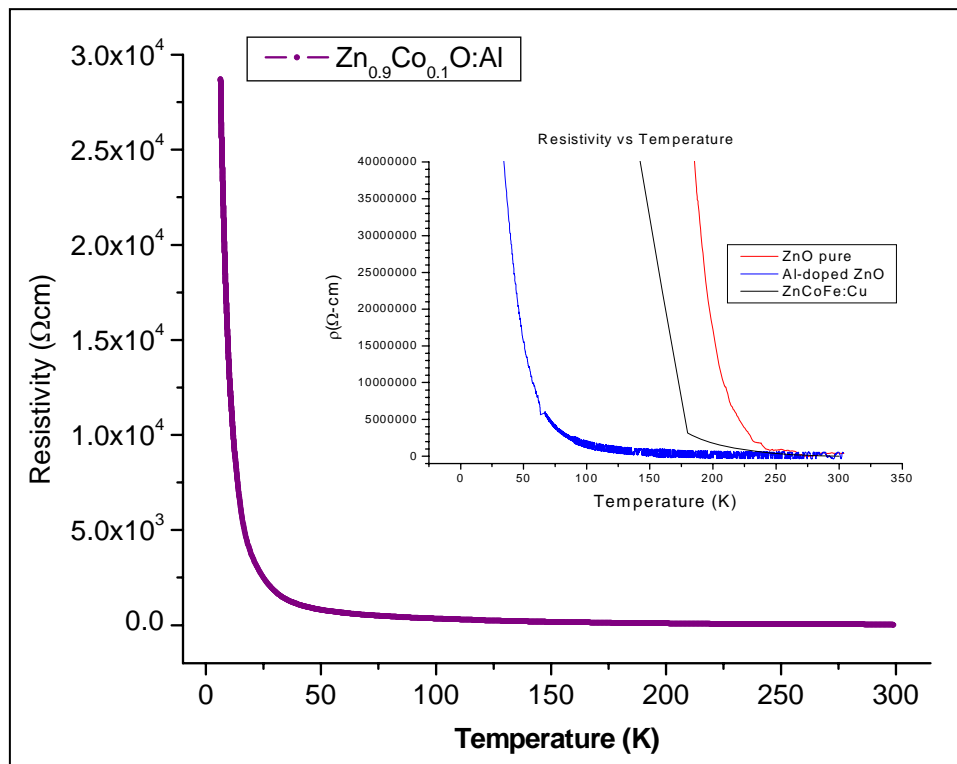


Figure 5.28 Variation of resistivity with the temperature (below room temperature) of Co-doped ZnO films.

5.6.4 Magnetic properties of Co,Fe-doped ZnO films

Diluted magnetic semiconductors (DMS) are considered as very important materials for spintronics [77]. Spintronics (spin + electronics) is the field of electron techniques, which focuses its attention on creating functional devices based on control of ferromagnetic ordering by electric field. In DMS structure the exchange interaction between *d*-electrons, localized on magnetic ions, and *sp*-conduction electrons takes place [78]. In result the material gets unusual magnetic, optical and magneto-optical properties. By interest to ZnO as a promising material DMS, especially of the Zn(TM)O type (where TM is a transition metal) and due that there are few articles that pay less attention on magnetic properties of ZnO doped by various transition metals, will we shows here some results found about of the magnetoresistance of Al (6.68%)-doped Zn_{0.90}Co_{0.10}O film and about M-H behavior of Zn_{0.90}Co_{0.10}O and Zn_{0.85}[Co_{0.50}Fe_{0.50}]_{0.15}O films. Al (6.68%)-doped Zn_{0.90}Co_{0.10}O film was synthesized onto glass by co-sputtering from ceramic target of Zn_{0.90}Co_{0.10}O at 100W rf power and metallic target of Al applying dc magnetron at ~ -770 V and 86 mA during 90 min. The substrate was not heated intentionally, but the temperature was registered up ~ 40°C. The argon gas pressure was 9.0 x10⁻³ Torr.

Magnetoresistance Of Al (6.68%)-doped Zn_{0.90}Co_{0.10}O film

Magnetoresistance, MR of Al (6.68%)-doped Zn_{0.90}Co_{0.10}O film was measured at various temperatures. Magnetoresistance measurement has been used to study *s-d* exchange interaction between *sp*-conduction electrons and spins of *d*-electrons localized on Co²⁺ and Fe²⁺ ions. These measurements were carried out by R. Martínez into development of their

thesis: “*Estudio de magnetoresistencia y rotación de Faraday en $Zn_{1-x}(Co)_xO$* ” in the laboratory of Magneto-optical, Department of Physic of the University of Puerto Rico-Mayaguez campus. Figure 5.29 illustrate these interesting measures at various temperatures.

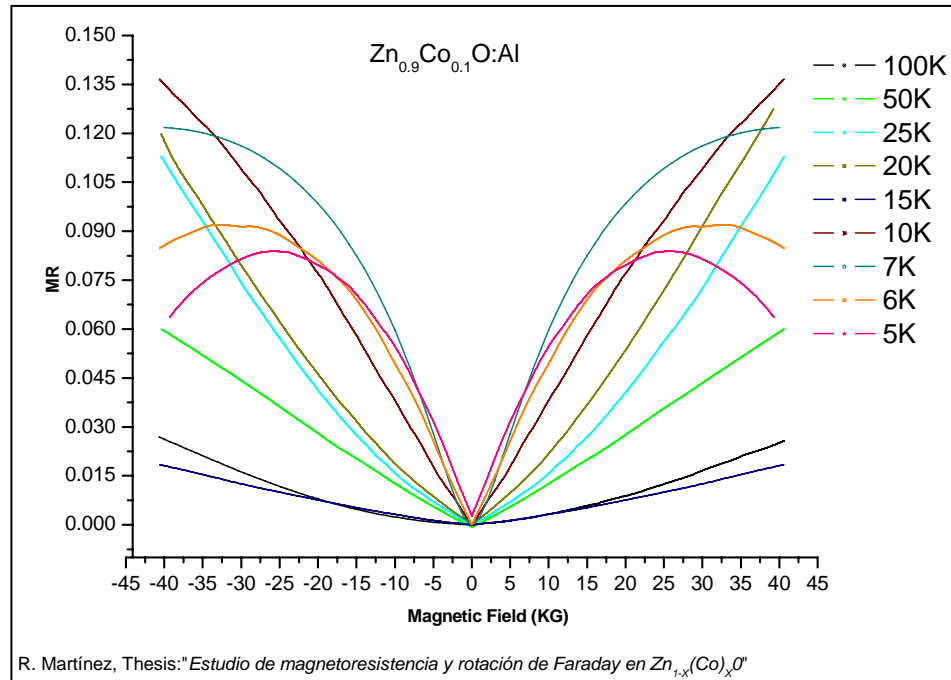


Figure 5.29 Magnetoresistance (MR) at various temperatures for $Zn_{0.90}Co_{0.10}O:Al$ film. MR is defined as: $[\rho(H) - \rho(0)] / \rho(0)$.

More discussions on these results are indicated in the thesis by the author of these measurements. Only I will make a brief comment about these results. Usually the magnetoresistance $MR \equiv [\rho(H) - \rho(0)] / \rho(0)$, for ZnO film is weakly negative [79]. However, the Al (6.68%)-doped $Zn_{0.90}Co_{0.10}O$ film shows a relatively large positive magnetoresistance at the high magnetic field in the temperature range from 7 to 50K, which reached 11.9% at 7K for the magnetoresistance peak, as shown in the Figure 5.29. At 100K, the MR is lowest. We

know that the large positive magnetoresistance is related to exchange-induced giant spin splitting of the electrons states and the formation of magnetic polarons (MPs) [80], therefore, we can assume that this MPs are formed by localized electrons polarizing the magnetic impurities inside the effective s-d exchange interaction region.

Room temperature $M-H$ behavior of $\text{Zn}_{0.90}\text{Co}_{0.10}\text{O}$ and $\text{Zn}_{0.85}[\text{Co}_{0.50}\text{Fe}_{0.50}]_{0.15}\text{O}$ films:

ZnO, a wide gap II-VI semiconductor, attracts attention as a material with possible application in optoelectronic devices such solar cells, ultraviolet emitting diodes, and transparent high-power electronic devices [81]. Theoretical predictions of room temperature ferromagnetism (FM) in diluted magnetic semiconductors (DMS) recently focused attention on magnetic-ion-substituted ZnO with wurtzite structure similar to GaAs [82]. The main idea is that the ferromagnetic ordering is caused by the exchange interaction between magnetic impurities mediated by free electrons or holes [6]. Regarding the magnetic properties of the Co,Fe-doped ZnO films, contrasting behaviors were obtained by different research groups. Also, the results are not very reproducible. This controversy between research teams may result from the growth method used and/or from the growth conditions (argon/oxygen pressure, deposition temperature, etc). For example, Ueda *et al.* doped Co in ZnO using PLD technique, and found that a few films showed systematic ferromagnetic behavior, but the rest of the films showed spin-glass behavior [66]. Jin *et al* [83] found no indication FM for ZnO:Co films (with some Al) grown by utilizing laser molecular beam epitaxy (MBE).

Optical studies, similar this work, confirm Co is divalent, high spin, and substituting for Zn. Kim *et al.* [84] have used PLD to grow $Zn_{1-x}Co_xO$ and found evidence for FM when the films are grown under low O_2 partial pressures. However, they pointed to the presence of Co clusters in their thin films as reason for room temperature FM. On the other hand, FM was also observed for the Co,Fe-doped ZnO films. Y. Mok Cho *et al* [67] reported that with a rapid thermal annealing vacuum, gave rise to room temperature ferromagnetism on $Zn_{1-x}(Co_{0.5}Fe_{0.5})_xO$ growth by reactive magnetron co-sputtering method using Zn and CoFe metal targets.

Based on the above commented discrepancies on the magnetic properties of transition metals substituted ZnO, specifically Co and Fe, we carried out a preliminary study $M-H$ behavior of $Zn_{0.90}Co_{0.10}O$ and $Zn_{0.85}[Co_{0.50}Fe_{0.50}]_{0.15}O$ films grown onto quartz by magnetron sputtering. The $M-H$ curves of these films were measured using a Superconducting Quantum Interference Device (SQUID) at 300 K. The magnetic field was applied parallel to the film plane. The quartz substrate has diamagnetic response at this temperature, reason why the corresponding data was subtracted from total data. Although these films exhibited good crystallinity with a fraction of Zn atoms substituted by Co and Fe, no indication of FM in both films was observed between -2000 and 2000 Oe, as shown in Figure 5.30.

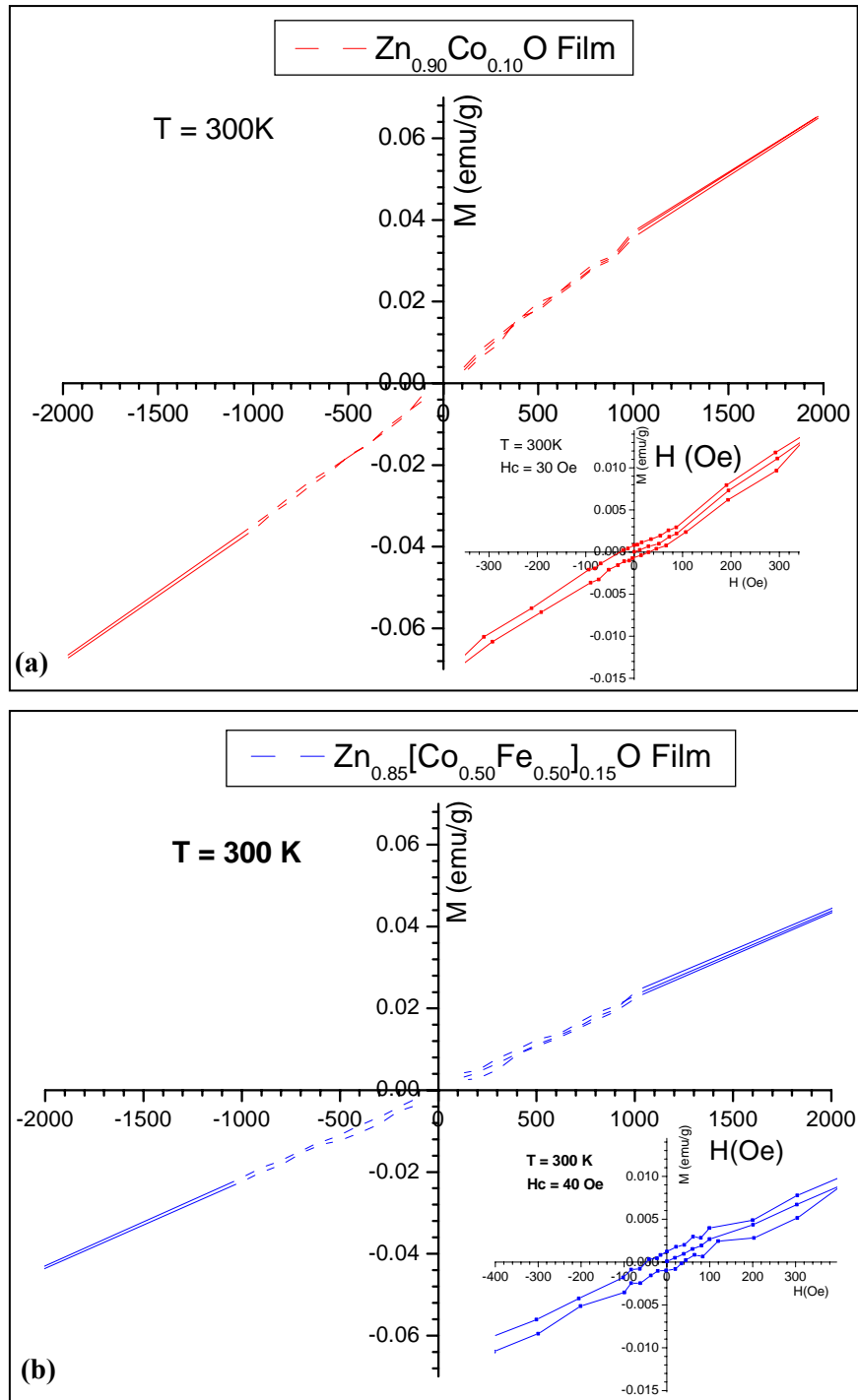


Figure 5.30 Magnetization as function of applied field at $T = 300\text{K}$ (a) $\text{Zn}_{0.90}\text{Co}_{0.10}\text{O}$ and (b) $\text{Zn}_{0.85}[\text{Co}_{0.50}\text{Fe}_{0.50}]_{0.15}\text{O}$ films. The inset in each figure shows the coercivity H_c of 40 and 30 Oe respectively.

It is well known that the magnetic properties of II-VI DMS are dominated by the antiferromagnetic superexchange interactions between the localized spins, which result in paramagnetic, spinglass or antiferromagnetic behavior depending on the concentration of the magnetic ions and temperature [6]. In addition, possibly there is a strong antiferromagnetic interaction between the Co ions; if they do not interact with each other, they would show the Curie behavior. Although both the ferromagnetic and paramagnetic/antiferromagnetic Co ions has the same 2+ valence and the tetrahedral crystal field, subtle differences such as neighboring defects and local lattice distortion may lead to the different magnetic behaviors [84]. It is known that in ferri- and antiferromagnetic compounds 3d transition metals cation-cation as well as cation-anion-cation interactions are possible [85]. In both cases the determinant parameter is the distance between magnetic ions. In this sense, from interpreted by R. Sadikhov *et al.*[85] we can assume that a exchange interaction along axis c of one type, for example, interaction cation-cation ($\text{Fe}^{2+} - \text{Fe}^{2+}$, $\text{Fe}^{3+} - \text{Fe}^{3+}$ or $\text{Co}^{2+} - \text{Co}^{2+}$) or cation-anion-cation ($\text{Fe}^{2+} - \text{O}^{2-} - \text{Fe}^{2+}$ or $\text{Co}^{2+} - \text{O}^{2-} - \text{Co}^{2+}$) took place in our samples. Then as a result of contraction distance between Fe^{2+} (or Fe^{3+}) ions along c axis, the increase of Curie temperature (i.e. exchange interaction) must be observed. Therefore, these interactions along c axis in our Co,Fe-doped ZnO films could be of antiferromagnetic character. Despite of this probable antiferromagnetic behavior it was possible to observe little coercive field (H_c) of 30 Oe and 40 Oe for $\text{Zn}_{0.90}\text{Co}_{0.10}\text{O}$ and $\text{Zn}_{0.85}[\text{Co}_{0.50}\text{Fe}_{0.50}]_{0.15}\text{O}$ films, respectively. We consider that this difference in magnetic behaviors among these films is due probably to the differences in electric properties. The $\text{Zn}_{0.85}[\text{Co}_{0.50}\text{Fe}_{0.50}]_{0.15}\text{O}$ film showed major conductive behavior that $\text{Zn}_{0.90}\text{Co}_{0.10}\text{O}$ film. This last film has a resistivity of four orders of magnitude

greater than $\text{Zn}_{0.85}[\text{Co}_{0.50}\text{Fe}_{0.50}]_{0.15}\text{O}$ film. Hence, it is important to consider an increase of carriers in these DMS in order to obtain a possible ferromagnetic behavior. K. Ueda *et al.* [66] found that the $\text{Zn}_{0.85}\text{Co}_{0.15}\text{O}$ film indicated that only few films showed ferromagnetism features, while others showed spin glass-like behaviors. The reproducibility of the method was poor (less than 10%). Other studies showed that in the case of wide gap II-VI compounds, neither of these transition metals (TM) introduces free carriers. However, for sufficiently high TM concentrations a Mott-Hubbard transition is expected, leading to a transport through the gap d -states. A co-doping with either shallow acceptors or donors could make such transport, and the associated exchange interaction, more efficient. Since the TMs act as deep donors and acceptors, the co-doping of such compounds with shallow impurities, as Al for example, constitutes a natural way to control the ferromagnetic couplings [86]. Indeed, according to Sato and Katayama-Yoshida [87], for Fe, Co, or Ni doped ZnO, the ferromagnetic state is stabilized by the doping of shallow donors.

On the other hand, we believe that a thermal post-treatment under vacuum conditions could induce ferromagnetic features in $\text{Zn}_{0.85}\text{Co}_{0.15}\text{O}$ and $\text{Zn}_{0.85}[\text{Co}_{0.50}\text{Fe}_{0.50}]_{0.15}\text{O}$ films. This annealing would increase the electron concentration and, hence, enhance the corresponding ferromagnetic properties. This result was observed by Mok Cho *et al* [67] on $\text{Zn}_{1-x}(\text{Co}_{0.5}\text{Fe}_{0.5})_x\text{O}$ films. They showed that a rapid thermal annealing under vacuum leads to the marked increase of the Curie temperature as well as the spontaneous magnetization and the carrier concentration, giving rise to room temperature ferromagnetism in the Co,Fe-doped ZnO films. Finally, these results found in this work suggest to continue the study about the

magnetic behavior of these films, as for example, to determine the temperature of curie (T_c) through the temperature effect on magnetization.

CHAPTER 6

Conclusions and suggestions

In order to achieved high quality of the ZnO-based films and particularly on Co,Fe-doped ZnO films, the role of the substrate to target distance and radio frequency power on deposition rate, structure, optical and electrical properties on ZnO films synthesized onto glass by the magnetron sputtering technique was investigated. The most important results that followed from the respective studies are briefly highlighted:

- The deposition rate (r) is almost constant when the substrates were localized on regions close to target, while its value increased almost lineally with the rf power with:

$$r = 4.35967 (P_{rf} - P_{rf,th}) . \text{ Being, } P_{rf,th} \text{ the rf power threshold.}$$

- Highly oriented polycrystalline ZnO thin films were observed on substrates localized close to target and for greater rf power. This result could be favorable for the conductivity of the films due that drive at a degenerate or non-stoichiometric semiconductor n-type, being for example O:29.31% and Zn:70.69% at. for 100 W rf power. However, for rf power between 75 and 125 W compressive stress was observed, which could be reduced increasing the vertical projection height below target. From 5.5 we observed that on all ZnO films the average grain size has a direct correlation with film stress, i.e. the changes in grain size are similar at the changes in the films stress.

- The optical band gap values found for ZnO films were between 3.18 and 3.28 eV, which can be considering within the ZnO bulk (3.3 eV), nevertheless, was found in addition that the optical band gap is affected by films stress.
- ZnO and Al (4.85%at.)-doped ZnO films onto glass showed high optical transmittance of over 80% in the visible range. This means that these ZnO films can be considering as transparent conductive films for practical applications such as window materials in display, solar cells, and various optoelectronic devices. Their conductive behavior was improved by replacing Zn^{2+} species by Al^{3+} . Therefore, Al-doped ZnO films called AZO, is a degenerate semiconductor with a blueshift around 0.25 eV (difference of the energy band gap between Al-doped ZnO and ZnO film). This broadening effect is due to the Al effect which can be understood on the basis of Burstein-Moss (B-M) model.
- $Zn_{0.90}Co_{0.10}O$ and $Zn_{0.85}[Co_{0.50}Fe_{0.50}]_{0.15}O$ films prepared by rf magnetron sputtering from ceramic targets in argon atmosphere, showed wurtzite crystal structure with an increasing of the $d(002)$ due to increasing of the dopant fraction in the films, 'x', attributed to the actual incorporation of dopant ion into the host ZnO structure.
- The optical transmission spectra showed the decrease in band gap with increasing of the dopant fraction in the films, 'x'.

- Although these films exhibited good crystallinity with a fraction of Zn atoms substituted by Co and Fe, from $M-H$ measurements no indication of FM in both films was observed between -2000 and 2000 Oe. We assume that an exchange interaction along axis c , cation-cation ($\text{Fe}^{2+} - \text{Fe}^{2+}$, $\text{Fe}^{3+} - \text{Fe}^{3+}$ or $\text{Co}^{2+} - \text{Co}^{2+}$) or cation-anion-cation ($\text{Fe}^{2+} - \text{O}^{2-} - \text{Fe}^{2+}$ or $\text{Co}^{2+} - \text{O}^{2-} - \text{Co}^{2+}$) took place in our samples and as a result of contraction distance between Fe^{2+} (or Fe^{3+}) ions along c axis, and therefore, an increase of Curie temperature could be given indicating that $\text{Zn}_{0.90}\text{Co}_{0.10}\text{O}$ and $\text{Zn}_{0.85}[\text{Co}_{0.50}\text{Fe}_{0.50}]_{0.15}\text{O}$ films could be of antiferromagnetic character. However, despite of this probable antiferromagnetic behavior it was possible to observe a little coercive field (H_c) of 30 Oe and 40 Oe for $\text{Zn}_{0.90}\text{Co}_{0.10}\text{O}$ and $\text{Zn}_{0.85}[\text{Co}_{0.50}\text{Fe}_{0.50}]_{0.15}\text{O}$ films, respectively.
- From these results found in this work suggest to continue the study about the magnetic behavior of these films, as for example, to determine the temperature of Curie (T_c) through the temperature effect on magnetization.

REFERENCES

- [1] S.H Jeong, J.W. Lee, S.B. Lee, J.H. Boo, *Thin solid films* **435**(2003) 78-82.
- [2] K. Vanheusden, W.L. Warren, C. H. Seager, D. R. Tallant, J.A. Voight and B.E. Gnade, *J. Appl. Phys* **79**, 7983 (1996).
- [3] C.J. Sheppard, Thesis: Structural and Optical Characterization of α Si:H and ZnO; Faculty of science at the Rand Afrikaans University, (2002).
- [4] D.P. Norton, Y. W. Heo, M.P. Ivill, K. Ip, S. J. Pearton, M. F. Chisholm and T. Steiner, *Materialstoday* (June 2004) 34-40.
- [5] H.Y. Kim, J.H. Kim, Y.J. Kim, K.H. Chae, C.N. Whang, J.H. Song and S. Im, *Optical materials* **17** (2001) 141-144.
- [6] T. Dietl, H. Ohno and F. Matsukara, *Phys Rev. B*, Vol. 63 (2001) 195205-1/21.
- [7] Z.C. Jin, I. Hamberg and C.G. Granqvist, *J. Appl Phys.* **64**(10), (1988) 5117-5131.
- [8] R. B. Heller, J. McGannon, and A. H. Weber, *J. Appl. Phys.* **21**, 1283 (1950).
- [9] G. Burns, *Solid State physics*, Academic Press, Inc., Orlando, Florida 1998, 65-67.
- [10] R.G. Gordon, *MRS Bulletin/August* (2000) 52-57.
- [11] Ü. Özgür, Ya. I. Alivov, C. Liu, A. Teke, M. A. Reshchikov, V. Avrutin, S. Doğan, S.-J. Cho and H. Morkoç, *J. Appl. Phys* **98**, 041301-1 (2005).
- [12] A.F. Ioffe, *Physics of semiconductors*, Academic Press Inc., New York 1960, 148-151.
- [13] S.H Jeong, S. Kho, D. Jung, S.B. Lee, J.H. Boo, *Surface and coatings technology*, **174-175**(2003) 187-192.
- [14] R. R. Reeber, *J. Appl. Phys.* **41**, 5063 (1970).
- [15] L. Gerward and J. S. Olsen, *J. Synchrotron Radiat.* **2**, 233 (1995).
- [16] S. J. Pearton, W. H. Heo, M. Ivill, D. P. Norton and T. Steiner, *Semicond. Sci. Technol.* **19** (2004) R59–R74.
- [17] G.B. Palmer, K.R. Poeppelmeier, *Solid State Sciences* **4** (2002) 317–322.
- [18] H. Karzel *et al.*, *Phys. Rev. B* **53**, 11425 (1996).

- [19] M. Catti, Y. Noel, and R. Dovesi, *J. Phys. Chem. Solids* **64**, 2183 (2003)
- [20] I.V. Kityk, A. Migalska-Zalas, J. Ebothe, A. Elchichou, M. Addou, A. Bougrine and K.A. Chouane, *Cryst. Res. Technol.* **37** (2002) 4, 340-352.
- [21] M.L. Cohen, J.R. Chelikowsky, *Electronic structure and optical properties of semiconductors*, Springer-Verlag Berlin Heideberg 1988, 7-50.
- [22] B. K. Tanner, *Introduction to the physics of electrons in solids*, Cambridge University Press 1995, 79-90.
- [23] S. Tiwari, *Compound Semiconductor Device Physics*, Academic Press, Inc., New York, 1992, 13-46.
- [24] Ch. Kittel, *Introduction to Solid State Physics*, John Wiley, New York, 1996.
- [25] U. Rössler, *Phys. Rev.* **184**, 733 (1969).
- [26] Ch. Q. Sun, *Progress in Materials Science* 48 (2003) 521–685.
- [27] K. Sawada, Y. Shirotori, K. Ozawa and K. Edamoto, Photon factory activity report 2002 #20 Part B (2003).
- [28] I. Ivanov and J. Pollmann, *Phys. Rev. B* 24. 7273 (1981).
- [29] W. Göpel, J. Pollmann, I. Ivanov and B. Reihl, *Phys. Rev. B* 26 (1982)3144-3150.
- [30] R. Dhar, P. D. Pedrow, K. C. Liddell, Q. Ming, T. M. Moeller, *IEEE Transactions on plasma science*, vol. 33, No. 1, February 2005.
- [31] R. D. Vispute *et al.*, *Appl. Phys. Lett.* **73**, 348 (1998).
- [32] S.K. Hong, Y. Chen, H.J. Ko, H. Wensch, T. Hanada and T. Yao, *Journal of electronic materials*, Vol. 30, No. 6, 2001.
- [33] T.E. Murphy, D.Y. Chen and J.D. Phillips, *Journal of electronic materials*, Vol. 34, No. 6, 2005.
- [34] M. Okuya, K. Shiozaki, N. Horikawa, T. Kosugi, G.R. Asoka Kumara, J. Madarasz, S. Kaneka, G. Pokol, *Solid State Ionics* 172 (2004) 527–531.

- [35] P. Pushparaht, A. Kariem Aroft and S. Radhakrishnat, *J. Phys. D: Appl. Phys.* 27 (1994) 1518-1521. Printed in the UK.
- [36] H. H. Afify, S. H. EL-Hefnawi, A. Y. Eliwa, M. M. Abdel-Naby and N. M. Ahmed, *Egypt. J. Solids*, Vol. (28), No. (2), (2005).
- [37] G.Y. Yeom and J. A. Thornton, *J. Appl. Phys.* 65(10), (1989) 3816-3832.
- [38] S. Bose, S. Ray and K. Barua, *J. Phys D: Appl. Phys*, 29 (1996) 1873-1877. Printed in the UK.
- [39] K. Ho Kim, K. Cheol Park and D. Young Ma, *J. Appl. Phys.* 81(12), (1997) 7764-7772.
- [40] R. Cebulla, R. Wendt and K. Ellmer, *J. Appl. Phys.* 83(2), (1998) 1087-1095.
- [41] K. Ellmer, *J. Phys D: Appl. Phys*, 33 (2000) R17-R32. Printed in the UK.
- [42] R. Das and S. Ray, *J. Phys D: Appl. Phys*, 36 (2003) 152-155.
- [43] A. Belkind, A Freilich, J Lopez, Z Zhao, W Zhu and K Becker, *New Journal of Physics* 7 (2005) 90.
- [44] T. C. Grove, *Advanced energy industries*, Inc. SL-Whites-270.01 1M 08/00 (2000) Printed in U.S.A.
- [45] Meng, L.J., Azavedo, A. and dos Santos, M.P., *Vacuum* 46, 233 (1995)
- [46] D. J. Kang, J.S. Kim, S.W. Jeong, Y. Roh, S.H. Jeong, J.H. Boo, *Thin solid films* 475(2005) 160-165.
- [47] R.M. de la Cruz, R. Pareja and R. Gonzáles, *Phys. Rev.* B45, 685-6586 (1192).
- [48] T.K. Subramanyam, B. Srinivasulu Naidu and S. Uthanna, *Cryst. Res. Technol.* **35** 2000 10 1193-1202.
- [49] M. K. Jayaraj, A. Antony and M. Ramachandran, *Bull. Mater. Sci.*, Vol. 25, No. 3, June 2002, pp. 227–230.
- [50] K.V. Shalimova, *Física de los semiconductores*, Ed. MIR, Moscú 1975, pp.264-288.
- [51] A.P. Roth, J.B. Webb, D.F. Williams, *Phys. Rev* **B 25** (1982) 7836.

- [52] W.W. Wenas, A. Yamada, K. Takahashi, M. Yoshino and M. Konagai, *J. Appl. Phys.* 70 (1991) 7119.
- [53] P. M. Martin, *Vacuum and coating*, Nov. 2005, 30-33.
- [54] A. Hernando, J.M. Rojo, *Física de los materiales magnéticos*, Edit Sintesis, Printed in Spain, 2001.
- [55] *Handbook of Chemistry and Physics*, 80th Edition, David R. Lide, Editor in Chief, CRC Press (1999-2000) 12-118.
- [56] N. Spaldin, *Magnetic materials, fundamentals and device applications*, Cambridge University press, 2003].
- [57] B.D. Cullity and S.R. Stock, *Elements of X-ray diffraction*, third edition, Prentice Hall, New Jersey (2001) 4-9.
- [58] K. Brandenburg and H. Putz, *Match! Phase identification from powder diffraction*, crystal Impact (2003-2006) Postfach 12 51, D-53002 Bonn Germany.
- [59] Ashcroft, N. W. and Mermin, N. D., *Solid State Physics*, Saunders, 1976.
- [60] H. Ohta, K. Kawamura, M. Orita, M. Hirano, N. Saokura, H. Ozono, *Appl. Phys. Lett.* 77 (2000) 475.
- [61] J. Mass, P. Bhattacharya, R.S. Katiyar, *Materials Science and Engineering*, B103 (2003) 9-15.
- [62] Y. G. Wang, S. P. Lau, H. W. Lee, S. F. Yu, B. K. Tay, X. H. Zhang, K. Y. Tse and H. Hng, *J. Appl. Phys.* 94(3), (2003) 1597-1604.
- [63] V. Gupta and A. Mansingh, *J. Appl. Phys.* 80(2), 15 July 1996.
- [64] P. M. Amirtharaj and D. G. Seiler, *Optical properties of semiconductors, Handbook of optics-devices, measurements and properties*, Vol.II, Second Edition Sponsored by the Optical Society of America.
- [65] E. Burstein, *Phys. Rev* 93(1954) 632.
- [66] K. Ueda, H. Hitoshi and T. Kawai, *Appl. Phys. Lett.* 79 (2001) 988.

- [67] Y. Mok Cho, W. Kil Choo, H. Kim, D. Kim and Y. Ihm, *Appl. Phys. Lett.* 80 (2002) 3358.
- [68] Y.Z. Yoo, T. Fukumura, Z. Jin, K. Hasegawa, M. Kawasaki, P. Ahmet, T. Chikyow and H. Koinuma, *J. Appl. Phys.*, Vol. 90 (2001) 4246-4250.
- [69] R. Loudon, *Adv. Phys.* 13, 423 (1964).
- [70] M.S. Tomar, R. Melgarejo, P.S. Dobal and R.S. Katiyar, *J. Mater.Res.*, Vol. 16, No. 4, Apr (2001) 903-906.
- [71] P. Koidi, *Phys.Rev.B* 15, 2493 (1977).
- [72] S.G. Yang, A.B. Pakhomov, S.T Hung and C.Y. Wong, *IEEE Transactions on magnetics*, Vol. 38, No. 5, Sep. (2002) 2877-2879.
- [73] K. Joo Kim and Y. Ran Park, *Appl. Phys. Lett.* 81, 1420-1422 (2002).
- [74] K. Samanta, P. Bhattachary and R.S. Katiyar, *Appl. Phys. Lett.* 87, 101903 (2005).
- [75] F. Urbach, *Phys. Rev* 92(1953)1324.
- [76] S.B. Majumder, M. Jain, P.S. Dobal and R.S. Katiyar, *Mat. Scienc and Eng*, B103 (2003) 16-25.
- [77] J.K. Furdyna, *J. Appl. Phys.*, 64 (4), 15 August 1988, R29-R58.
- [78] V. A. Karpina, V.I. Lazorenko, C.V. Lashkarev, V.D. Dobrowski, L. I. Kopylova, V.A. Baturin, S.A. Pustovoytov, A. Karpenko, S. A. Eremin, P.M. Lytvyn, V.P. Ovsyannikov and E. A. Mazurenko, *Cryst. Res Technol.* 39, No. 11,980-992 (2004).
- [79] J.H.Kim, *J.Appl.Phys.*92,6066(2002).
- [80] M. Sawicki, *Phys.Rev.Lett.* 56, 508 (1986).
- [81] S. Kolesnik, B. Dabrowski and J. Mais, *J. Appl. Phys.*, Vol. 95 (2004) 2582-2586.
- [82] T. Dietl, H. Ohno and F. Matsukara, J. Cibert and D. Ferrand, *Science* 287, 1019 (2000).
- [83] Z. Jin *et al*, *Appl. Phys. Lett.* 78, 3824 (2001).
- [84] M. Kobayashi, Y. Ishida, J. Hwang, T. Mizokawa, A. Fujimori, K. Mamiya, J. Okamoto, Y. Takeda, T. Okane, Y. Saitoh, Y. Muramatsu, A. Tanaka, H. Saeki, H. Tabata and T. Kawai, <http://arxiv.org/> arXiv:cond-mat/0505387 v1 , 17 May 2006.

- [85] R. Sadikhov, A. Namazov and J. Guseinov, *Tr. J. of Physiscs* **22** (1998), 199-202.
- [86] H. Katayama-Yoshida, R. Kato and T. Yamamoto, *J. Cryst. Growth*, **231**, 428 (2001).
- [87] K. Sato and H. Katayama-Yoshida, *Jpn. J. Appl. Phys.* **40**, L334 (2001).